Spring 2018

Modeling of shrinkage porosity defect formation during alloy solidification

Vahid Khalajzadeh
University of Iowa

MODELING OF SHRINKAGE POROSITY DEFECT FORMATION DURING ALLOY SOLIDIFICATION

by

Vahid Khalajzadeh

A thesis submitted in partial fulfillment
of the requirements for the Doctor of
Philosophy degree in Mechanical Engineering
in the Graduate College of
The University of Iowa

May 2018

Thesis Supervisor: Professor Christoph Beckermann

Graduate College
The University of Iowa
Iowa City, Iowa

CERTIFICATE OF APPROVAL

_____

Ph.D. THESIS

_____

This is to certify that the Ph.D. thesis of

Vahid Khalajzadeh

has been approved by the Examining Committee for the thesis requirement for the Doctor of Philosophy degree in Mechanical Engineering at the May 2018 graduation.

Thesis Committee:

Christoph Beckermann, Thesis Supervisor

David G. Rethwisch

H.S. Udaykumar

Albert Ratner

Hongtao Ding

To my family

ACKNOWLEDGEMENTS

First, I would like to thank my academic adviser, Prof. Christoph Beckermann, for his support and deep insights about my research topic that helped me a lot at various stages of my PhD project. Also, my sincere thanks go to my thesis committee: Dr. Rethwisch, Dr. Udaykumar, Dr. Ratner, and Dr. Ding for their precious comments and suggestions about my dissertation. I would like to thank my fellow friends at Solidification Lab for all the discussions and the fun we have had during the past years.

Last but not the least, I would like to thank my wonderful family: my beloved wife Mina, my devoted parents, my brothers, my sister, my lovely nieces and nephews for supporting me spiritually throughout my study at the University of Iowa and my life in general. I love you all!

ABSTRACT

Among all casting defects, shrinkage porosities could significantly reduce the strength of metal parts. As several critical components in aerospace and automotive industries are manufactured through casting processes, ensuring these parts are free of defects and are structurally sound is an important issue. This study investigates the formation of shrinkage-related defects in alloy solidification. To have a better understanding about the defect formation mechanisms, three sets of experimental studies are performed. In the first experiment, a real-time video radiography technique is used for the observation of pore nucleation and growth in a wedge-shaped A356 aluminum casting. An image-processing technique is developed to quantify the amount of through-thickness porosity observed in the real-time radiographic video. Experimental results reveal that the formation of shrinkage porosity in castings has two stages: 1-surface sink formation and 2- internal porosity evolution. The transition from surface sink to internal porosity is defined by a critical coherency limit of $g_{s,sur}$. In the second and third experimental sets, two Manganese-Steel (Mn-Steel) castings with different geometries are selected. Several thermocouples are placed at different locations in the sand molds and castings to capture the cooling of different parts during solidification. At the end of solidification, castings are sectioned to observe the porosity distributions on the cut surfaces. To develop alloys' thermo-physical properties, MAGMAsoft (a casting simulation software package) is used for the thermal simulations. To assure that the thermal simulations are accurate, the properties are adjusted to get a good agreement between simulated and measured temperatures by thermocouples.

Based on the knowledge obtained from the experimental observations, a computational model is developed for the prediction of shrinkage porosity in castings. The model, called "advanced feeding model", includes 3D multi-phase continuity, momentum and pore growth equations which inputs the material properties and transient temperature fields, and outputs the feeding velocity, liquid pressure and porosity

distributions in castings. To solve the model equations, a computational code with a finite-volume approach is developed for the flow calculations. To validate the model, predicted results are compared with the experimental data. The comparison results show that the advanced feeding model can accurately predict the occurrence of shrinkage porosity defects in metal castings. Finally, the model is optimized by performing several parametric studies on the model variables.

PUBLIC ABSTRACT

Most materials shrink once they solidify. Depending on the cooling history of a cast component, the shrink volume may appear as exterior or internal defects in the casting. As metal industries are constantly looking for ways to improve the quality of their products, predicting shrinkage defects is an important issue. In the current study, a computational model is developed that predicts the location and the size of shrinkage defects in castings. The model is validated and optimized by comparing the predicted results with the experimental data.

TABLE OF CONTENTS

LIST OF TABLES

LIST OF FIGURES

LIST OF NOMENCLATURE

Symbols		Description	Unit
$\boldsymbol{g}$	:	Gravity Vector	m/s^2
g_ℓ	:	Liquid Volume Fraction	-
g_s	:	Solid Volume Fraction	-
g_p	:	Pore Volume Fraction	-
$\bar{g}_p$	:	Averaged Pore Volume Fraction	-
$\bar{g}_{P,Th}$	:	Through-thickness Averaged Pore Volume Fraction	-
$g_{s,sur}$	:	Surface Coherency Solid Fraction	-
$g_{s,coh}$	:	Coherency Limit Solid Fraction	-
G	:	Thermal Gradient	$^oC/m$
K	:	Mushy Zone Permeability	m^2
K_0	:	Permeability Coefficient	m^2
μ_ℓ	:	Dynamic Liquid Viscosity	Pa.s
Ny	:	Niyama Criterion	$(^oC\text{-}s)^{1/2}/m$
Ny^*	:	Dimensionless Niyama Criterion	-
P_{atm}	:	Atmospheric Pressure	bar
P_ℓ	:	Dynamic Liquid Pressure	bar
$P_{\ell,T}$	:	Total Liquid Pressure	bar
P_h	:	Hydrostatic Pressure	bar

Symbols		Description	Unit
P_σ	:	Capillary Pressure	bar
P_p	:	Pore Pressure	bar
P_{mold}	:	Mold Pressure	bar
Π	:	Nucleation Parameter	bar
ρ_ℓ	:	Liquid Density	kg/m^3
ρ_s	:	Solid Density	kg/m^3
ρ_p	:	Pore Density	kg/m^3
$\bar{\rho}$	:	Mixture Density	kg/m^3
t	:	Time	s
$\boldsymbol{u}$	:	Superficial Velocity Vector	m/s
T_{liq}	:	Liquidus Temperature	^oC
T_{sol}	:	Solidus Temperature	^oC
$\dot{T}$	:	Cooling Rate	$^oC/s$
$\boldsymbol{v}$	:	Liquid Velocity Vector	m/s
v, v_0, v_{100}	:	Pixel Values	-
V	:	Volume	m^3
V_{Cast}	:	Casting Volume	m^3
V_{Shrink}	:	Shrink Volume	m^3
V_P	:	Pore Volume	m^3

CHAPTER 1. INTRODUCTION

1.1 Motivation

Foundries and metal casting suppliers are constantly trying to produce higher quality components with lower cost and shorter development time. Some of the most common casting defects, such as: shrinkage porosities, oxide inclusions, and alloy segregation, form during mold filling or solidification [1, 2, 3]. Among all these defects, shrinkage porosities could significantly reduce fatigue life, tensile and creep capabilities of metal parts [4, 5, 6]. Software developers have been collaborating with industrial companies to develop and implement models that capture the physics behind the porosity defect formation, while considering the computational limits of modern castings. These models could be helpful in optimization of process parameters, mold, gating and riser designs, while reducing the requisite number of trial-and-error studies. During the past years, researchers have been working to develop a comprehensive porosity models that account the fundamental science of porosity formation.

1.2 Literature Review

Porosity defects are mostly classified as shrinkage and gas porosities in metallurgy and metal casting industry. Shrinkage-related defects are caused by the density change during solidification. They form when the accompanying shrinkage can no longer be fed by feeding flow. It sometimes forms late in solidification, when the solid dendritic network is rigid, and has a low permeability. As a result, the porosity takes on the tortuous shape of the remaining spaces between the dendrites. But if a shrinkage porosity happens early in solidification, it will have time to grow and appear as an open hole in castings. The gas porosity, on the other hand, occurs when the melt contains relatively large amounts of dissolved gas. In this instance, pores can form much earlier in solidification, and therefore they have freedom to adopt a more spherical shape.

Depending on the size and the location of porosity defects, they are classified as micro-porosity, macro-porosity or surface sinks. The differences between porosity defects are illustrated in Figure 1.1, which contains photographs of different porosity defects such as: exterior surface depression or surface sink [Figure 1.1(a)], macro-shrinkage porosity [Figure 1.1(b)], micro-shrinkage porosity [Figure 1.1(c)], and gas porosity [Figure 1.1(d)].

The complexity of cast components has steadily increased as the metals industry strives for mass reduction, higher content and improved quality. Researchers have been working to develop a comprehensive porosity models that predict the formation of porosity defects during solidification. By obtaining an accurate porosity model, engineers can achieve optimal design solutions easier and faster. Casting porosity has been the subject of numerous solidification research studies since the 1960's. Piwonka and Flemings [7] and Kubo and Pehlke [8] identified porosity formation mechanisms and developed a mathematical model to describe porosity evolution during solidification. Over the next four decades, advances in the understanding and modeling of porosity were made by many solidification researchers [9, 10, 11, 12, 13, 14]. These advances are: refining the description of the liquid pressure drop associated with flow in the mushy zone; new or improved thermodynamic approximations; modeling the diffusive transport of liquid phase gas-solute toward growing gas pores; including the influence of the dispersion pore-nuclei potency upon final pore size distributions; and in-situ pore measurement during solidification. Much of this work has been summarized in review papers [15, 16].

For decades, foundry process engineers have qualitatively predicted the presence and severity of casting shrinkage porosity using the empirically derived Niyama criterion [17], $Ny = G/\sqrt{\dot{T}}$; where G is the thermal gradient, and $\dot{T}$ is the cooling rate. While useful, this criterion has shortcomings. First, since the Niyama criterion does not utilize material properties or solidification path information, the critical Ny value that is used to

detect the onset of shrinkage porosity is dependent on the alloy and process and must be empirically determined. Secondly, the Niyama criterion cannot be used to quantitatively determine the amount of porosity that will form. Carlson and Beckermann [18] proposed a novel procedure for prediction of shrinkage porosity by developing a dimensionless form of the Niyama criterion (Ny^*) that incorporates mushy zone physics and alloy properties. This research showed that Ny^* calculations performed during computer casting simulations can be used to directly predict shrinkage pore volume fractions throughout the casting; with knowledge of the alloy's solid fraction-temperature curve and total solidification shrinkage. Note that this criterion cannot be used to predict gas porosity. An experimental validation of the Ny^* model has recently been reported by Guo et al. for Ni-based superalloy castings [19].

Carlson et al. [20] developed a volume-averaged model that predicts both gas-related and shrinkage-related porosity by accounting for the simultaneous effects of pressure drop and hydrogen diffusion on pore growth. In this model, the gas species conservation equation was coupled with equations for flow continuity and the pressure field in solidifying metal. Yao et al. [21] applied this model in a pore formation investigation of the A356 aluminum alloy and showed that the model developed by Carlson et al. [20] provided an acceptable accuracy for gas porosity predictions in aluminum alloys. The volume-averaged model of Ref. [20] requires the coupled solution of transient conservation equations over the entire casting domain. While such generality may be needed for predicting porosity for complex casting geometries and solidification conditions, the model is computationally intensive and therefore difficult to apply for typical commercial casting simulations. Indeed, this model does not provide straightforward evaluation of the porosity volume fraction at any point in a casting as a function of the local cooling conditions, gas content and alloy properties, in contrast to the Ny^* model of Ref. [18] for pure shrinkage.

In 2002, Pequet et al. [22] developed a three-dimensional (3-D) model that

predicts the formation of shrinkage porosity in castings. They used a dynamic refinement algorithm to detect the feeding zones boundaries in the computational domain. In their model, they had to adjust the calculated void fractions to make sure that the overall mass was conserved during calculations. At about the same time, Carlson et al. [23] developed a 3D multi-phase model to predict the feeding velocity, the liquid pressure, and the porosity distributions during solidification. Although their method was more accurate compare to the previous models, they did not distinguish between the surface sink and internal porosity formation. Later, Reis et al. [24, 25] applied a model to predict the formation of surface sink and internal porosity defects in different alloy castings. They observed that in alloys with long freezing ranges, shrinkage defects tend to form on the exterior surface of the castings; while, in the short freezing range alloys, defects appear in form of internal porosities. Despite the success of different models in prediction of shrinkage defects, still a comprehensive porosity model, that accounts for the entire solidification shrinkage in the system and predicts both surface sink and internal porosity in casting, is lacking.

Advances in porosity models require precise experimental data for calibration. As most of the classical methods of porosity measurement are *ex-situ* approaches, they cannot provide extensive information about the porosity behavior during solidification. Awano and Morimoto [26] performed an *in-situ* experimental study on porosity defect formation in different Al-Si alloy castings. In their method, they gently put a floating thin wire on the melt surface to measure the movement of castings' surfaces during solidification. Their results showed that in absence of any gas content in melt, the shrinkage pipe and surface sink are formed at the early stages of solidification; when, the casting surfaces are not rigid [26]. Recently, real-time X-ray radiography has become an increasingly popular approach in solidification studies. In a series of experimental works several researchers have shown that real-time X-ray is a powerful tool for direct observation of porosity formation during solidification of aluminum alloys [27, 28, 29].

But most of the mentioned studies were focused on pore formation and growth at micro-scales; so, they did not provide comprehensive information about the porosity behavior at the scale of casting.

1.3 Objective of the Present Study

In the present study, to understand the physics behind the shrinkage defect formation in castings, three sets of experimental studies have been performed where different alloys such as: Manganese-Steel (Mn-Steel) and A356 aluminum alloys are considered for the casting materials. From the experimental observations, a computational model is developed for the formation of shrinkage defects in castings. The model uses three-dimensional (3D) and multi-phase equations to predict the feeding velocity, the liquid pressure and the porosity distributions during casting solidification. The next chapters describe the model development and parametric studies to investigate the effects of model parameters on the prediction results. Finally, the model is validated and optimized by comparing the predictions with the experimental results.

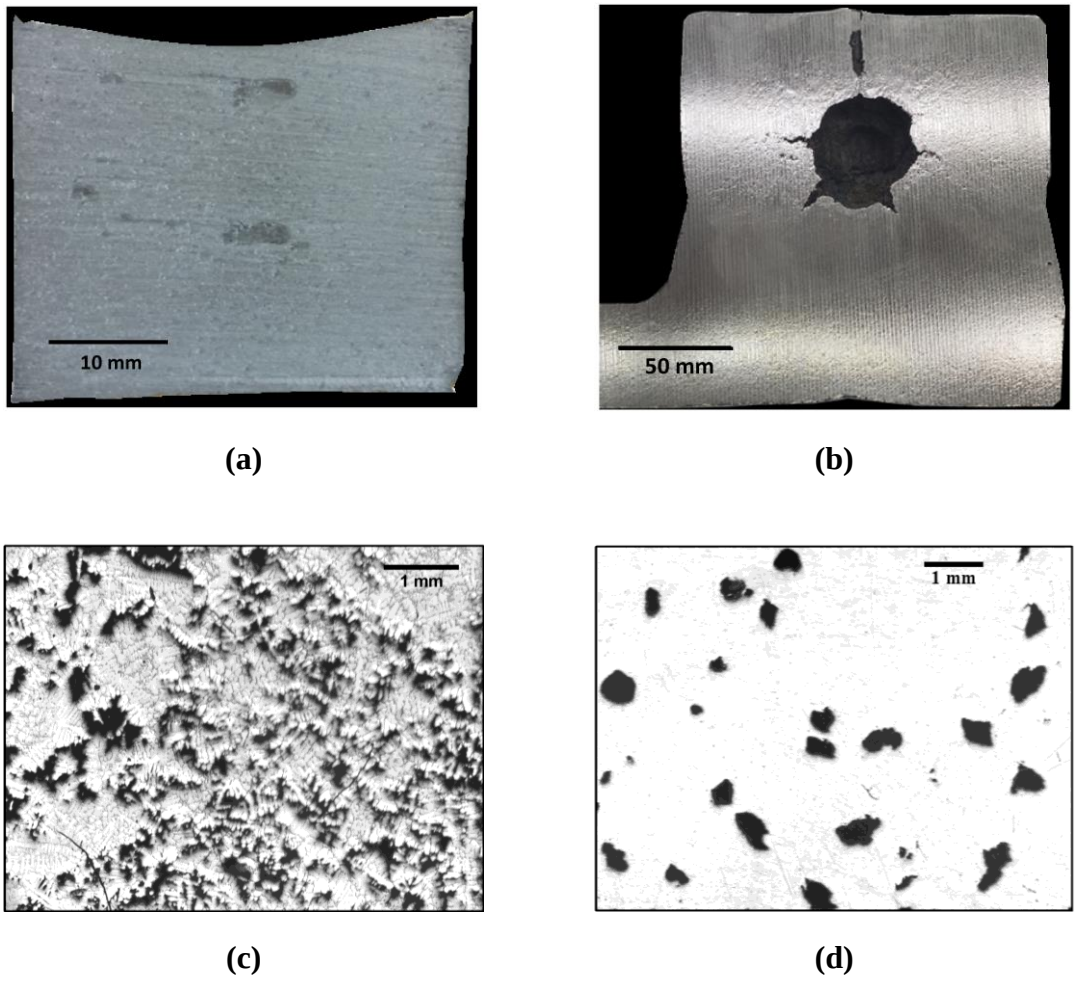

(a) **(b)**

(c) **(d)**

Figure 1.1. Typical porosity defects: (a) surface sink in aluminum alloy casting; (b); macro-shrinkage porosity on in Manganese Steel (Mn-Steel) casting; (c) micro-shrinkage porosity on the metallographic sections of aluminum alloy (d) gas porosity on the metallographic sections of aluminum alloy casting

CHAPTER 2. EXPERIMENTAL STUDIES

2.1 Introduction

The current experimental studies aim to provide a better understanding about the mechanisms of shrinkage porosity formation in castings. In the first experiment, a real-time video radiography technique was used for the observation of shrinkage porosity evolution during solidification of an aluminum wedge casting. In the second and third experiments, a Manganese-Steel (Mn-steel) alloy was selected for the casting material. In all the investigations, several thermocouples were placed at different locations in the mold cavities and walls to capture the cooling of castings during solidification. Finally, by analyzing the measured temperature data and using MAGMASOFT software package, the alloys' thermo-physical properties were developed as a function of temperature. The experimental setups, casting geometries and measurement results are described in the following sections.

2.2 Experiment 1: A356 Aluminum Alloy Wedge Casting

2.2.1 Experimental Setup

Internal shrinkage porosity in aluminum alloys tends to form in the thermal-mass center of castings, the last region to solidify. Hence, to investigate the evolution of shrinkage porosity defects in A356 aluminum alloys, a wedge-shaped geometry was considered for the experimental investigation. The casting geometry was composed of three main parts: a riser, a thin runner section and a wedge part. The schematic in Figure 2.1 shows how the different parts in the mold cavity are connected to each other. In the experiment, A356 aluminum alloy with the composition in Table 2.1 was poured at a temperature of $953\mathrm{K}(680^{\circ}\mathrm{C})$ and a filling time of 5 seconds. Quickly after filling, the thin runner section freezes off and the wedge part becomes isolated from the riser. Thus, all remaining solidification shrinkage in the wedge was converted to either surface sink or

internal shrinkage porosity. To minimize the riser size and to facilitate feeding to the casting, a riser sleeve was used as the sprue. Furthermore, to reduce unwanted artifacts in radiographic video, two Superwool® 607® HT [30] ceramic boards, with a thickness of 12.5 mm were used as the front and back mold walls [Figure 2.1(a)]. The mold cavity was located at the cope section and it was filled through the riser. Other details about the casting geometry and mold dimensions can be found in Figure 2.1.

The experimental investigation included two identical casting trials. One of them used a K-type thermocouple at the thermal center of wedge to measure the cooling during solidification. The other one used a real-time X-ray radiography technique to observe the nucleation and the evolution of shrinkage porosity during casting solidification. The experimental work was carried out at General Motors Company (GM) R&D lab where a 450 kV X-ray beam was used for real-time radiography. Figure 2.2 shows the experimental setup and the sample radiograph image recorded by imaging facility. As this study is about shrinkage porosity, not gas porosity, the hydrogen gas content was carefully removed from the melt.

2.2.2 Image Processing of Radiographs

To process the recorded radiographic video, first it is converted to a sequence of 8-bit grayscale images. In an 8-bit image, the pixel value is an integer number between 0 and 255 that represents the darkness and brightness of a pixel. Typically, values of 0 and 255 correspond to black and white colors on an 8-bit image, respectively. Other values between these two values will create different shades of gray. If a region on a radiographic image is too dark it shows that the averaged through-thickness density of an object in that area is relatively high; which, does not allow the X-ray beam to pass through the object and reach to the detector. Obviously, for lower local average through-thickness densities, the corresponding X-ray image would be brighter than the high value one. Figure 2.3(a) represents a typical 8-bit grayscale image obtained from the

radiographic video. In this image, due to a high-density ratio of A356 aluminum alloy to the mold materials, the casting region appears darker than the mold part. Moreover, due to a lower local density of porosity compare to A356 aluminum alloy, the shrinkage porosity region (at the center of the wedge casting) appears brighter than the sound area in the image. The related pixel values to dark and bright regions in the radiographic image can be determined using image's histogram curve. For example, in Figure 2.3(b), the image's histogram has two peaks at around values of 105 and 250. These peaks correspond to the most frequent pixel values on the foreground and background of the image, respectively. By interpreting the peaks as 0% and 100% average through-thickness porosity areas, one can obtain the porosity distribution contour from an X-ray image. By this assumption, any pixel values between two peaks will correspond to different porosity percentages in casting. If the porosity varies linearly between 0% and 100% porosity pixel values, Equation for the calculation of through-thickness averaged pore-fraction ($g_{p,Th}$) is defined as:

$$g_{p,Th} = \left(\frac{v - v_0}{v_{100} - v_0} \right) \qquad (2.1)$$

where, v is the pixel value, v_0 and v_{100} are the values of 0% and 100% porosity areas, respectively. Figure 2.3(c), shows the variation of v_0 and v_{100} on the real-time radiograph during solidification of the wedge casting. Due to the variation of alloy density during solidification, v_0 changes significantly by time, while, v_{100} variation is insignificant.

By take a closer look at the radiographic images, it is observed that at the vicinity of the casting's surfaces, the pixel values smoothly change to v_{100}. Thus, the edges are not clearly distinguishable on the radiograph images. So, at each time step after applying Eq. (2.1) to an X-ray image, the difference of current frame and the initial frame is used for tracking the surface movement in the casting. Moreover, to separate the internal porosity from the surface sink, a binary mask was used in the calculations. Finally, by

defining the pore-fraction distribution on the radiograph image, the total shrinkage is defined by taking an average over pore-fractions throughout the entire casting domain.

Based on the real-time observations, the evolution of shrinkage porosity in a wedge casting has two main stages: 1-surface sink formation and 2-internal porosity evolution. In the first stage, the entire shrinkage in the system goes to surface sink until the surfaces become coherent. Once the surface stops, the internal porosity nucleates at the internal part of the casting and develops until the end of solidification [Figure 2.4(a)-(d)]. Applying the developed image-processing technique to the radiograph images, the real-time porosity distribution was captured during solidification [Figure 2.4(e)-(h)]. The total shrinkage of the casting at each time is calculated by taking an average throughout the porosity domain. The final average pore volume fraction percentage in the wedge part is around 5.42%.

As, it can be observed in Figure 2.5(a), the surface sink happens on both inclined and back surfaces of the wedge part. The measurement results in Figure 2.5(b) reveal that in the first stage, when the runner freezes off at around t = 8s, the averaged surface sink volume fraction increases to 2.70% until about t = 80s. Then the surfaces stop moving and the internal porosity forms adjacent to the inclined surface and grows until the casting is fully solidified. The total shrinkage, which is the sum of surface sink and internal porosity percentages, becomes about 5.42% at t = 240s.

2.2.3 Metallographic Study

For the metallographic investigation, the wedge casting was sectioned from the location of maximum internal porosity observed on the radiographic image [Figure 2.6(a)]. The cut section was divided into four samples and each of them was ground and polished using standard metallographic techniques. An optical microscope, equipped with a high-definition digital camera, was used to photograph the shrinkage pores on the metallographic samples. Then, all photos were stitched together to create a composite

microscope image of the cut surface [Figure 2.6(b)]. It can be observed that a higher concentration of porosity exists at the central part of wedge. Moreover, a slightly asymmetric porosity distribution on the polished sample was observed. The reason might be due to different interfacial heat transfer coefficients on the front and back mold walls or it might be due to liquid metal leakage between the mold and the ceramic boards which occurred during filling.

To quantify the amount of porosity on the composite microscope image, first it was converted to an 8-bit greyscale image. By applying a proper image processing technique, the background shadows were removed from the image and then it was converted to a binary image. In a binary image, porosity areas are shown in black with the pixel value of 0, and the sound areas are shown in white with the pixel value of 1. Then by using a proper threshold value the 8-bit composite image was converted to a binary image. In a binary image, the area fraction of pores corresponds to the pore-fraction. Figure 2.6(c) shows a small box at the center of cut section where the measured area fraction or porosity percentage from the binary image [Figure 2.6 (d)] is around 29.7%. To compare the results from metallographic study with the real-time radiography ones, it is necessary to have the variation of through-thickness porosity along the cut section. So, as it can be observed in the Figure 2.7(a), several boxes of the same size are defined along the cut section to measure the through-thickness porosity percentages along the cut section. Comparison results in Figure 2.7(b) show that the image processing technique has an acceptable accuracy in measuring the through-thickness porosity distribution in the wedge casting.

2.2.4 Thermal Simulation

To determine the solid-fraction curve and other temperature dependent thermo-physical properties, the A356 aluminum alloy with the composition in Table 1 was used in the JMatPro® software package [31]. By using the initial property dataset from

JMatPro® and applying the exact experimental conditions, the casting was initially simulated in the MAGMASOFT software package. Unfortunately, the initial simulation results were not in a good agreement with the measured data. One of the important reasons was that the solidus and liquidus temperatures calculated by JMatPro® were different from the experimental values. Therefore, by using the described procedure in references [32] and [33], the solidus and liquidus temperature were defined from the analysis of measured cooling curves. The measured solidus and liquidus temperatures were defined as $921\ \mathrm{K}(548^{\circ}\mathrm{C})$ and $892\ \mathrm{K}(619^{\circ}\mathrm{C})$, respectively. Then, the initial JMatPro® property dataset was adjusted to the measured solidus and liquidus temperatures using a detailed procedure described in references [33]. Examples of adjusted temperature dependent solid-fraction and density curves are shown in Figure 2.8. On the solid-fraction curve [Figure 2.8(a)], the first and larger slope discontinuity is observed at around $850\ \mathrm{K}(577^{\circ}\mathrm{C})$, which corresponds to the initial formation of eutectic (Si) phase; whereas the lower and smaller slope discontinuity at around $830\ \mathrm{K}(557^{\circ}\mathrm{C})$ is associated with the formation of tertiary solid phase (Mg_2Si). Like the solid-fraction curve, the same slope discontinuities happen on the density-temperature curve [Figure 2.8(b)].

The interfacial heat transfer coefficient (IHTC) between the casting and sand mold was modeled with a temperature-dependent curve. An iterative trial-and-error procedure was applied to define the interfacial heat transfer coefficient (IHTC) curve between the sand mold and casting. The resulting IHTC curve as a function of temperature is a constant value of $700\ \mathrm{W/m^2K}$ for temperatures above the liquidus temperature; below liquidus temperature, IHTC decreases to $310\ \mathrm{W/m^2K}$ at the eutectic temperature; then it drops to $70\ \mathrm{W/m^2K}$ at $673\ \mathrm{K}(400^{\circ}\mathrm{C})$ and remains at this value for the lower temperatures. Due to the formation of surface sink on the inclined and top surfaces a slightly different IHTC curve was used for the inclined and top surfaces. The difference was only at temperatures below the liquidus where the new IHTC decreases sharply to

the value of $70\ W/m^2K$ at the eutectic temperature and remains at this value for the lower temperatures. For the Superwool® 607HT ceramics boards the property dataset in reference [30] was used in simulations. The IHTC between the casting and ceramic boards was assumed to be a constant value of $1000\ W/m^2K$. The calculated latent heat of solidification for A356 aluminum was $400\ kJ/kg$. Then, by applying the exact experimental conditions the casting is simulated using the MAGMASOFT software package. The agreement between the measured and simulated temperature at the location of thermocouple is shown in Figure 2.9.

2.3 Experiment 2 and 3: Manganese Steel Alloy Castings

2.3.1 Experimental Setup and Measurement Results

Experiment 2: Small Plate with Step-blocks

For the Experiment 2, Mn-Steel alloy with the composition in Table 2.2 is considered for experimental investigation. Details of casting dimensions and the location of thermocouples in the sand mold are presented in Figure 2.10.(a)-(d). The casting geometry in Figure 2.10. consists of different parts such as: a gating, a riser, a step block, a thin middle plate and a block at the far end of the casting. In this experiment, once the casting starts to solidify, the riser feed the entire shrink in the system until the flow resistance at the middle section becomes high enough that stops the flow reaching to the far end block. At this point, the block becomes isolated from feeder and a shrinkage porosity nucleates in the block and grow until the end of solidification. Finally, the feeding flow resistance at the middle plate becomes high enough that neither riser nor block could feed the middle part which causes to form a centerline shrink at the middle section. To prevent mold-metal reactions, the sand molds are made of Olivine sand instead of Silica sand.

To measure the cooling of the castings during solidification, four B-type and four

K-type thermocouples are placed at different locations in the casting and mold. K-type thermocouples are inserted through the top of the cope at distance of 0.25, 0.50, 0.75 and 1.0 inch away from the mold-metal interface. All B-type thermocouples are encased in a quartz tube and inserted from the top into the sand mold to measure the melt temperature during filling and solidification. Figure 2.11. shows the photos of the experimental setup and measurement setups where Mn-Steel alloy heat with $T_{pour} = 1678\ \mathrm{K}(1405^{\circ}\mathrm{C})$ and the composition in Table 2.2 is poured into the mold cavity. The filling time and the room temperature were 22 s and $300\ \mathrm{K}(27^{\circ}\mathrm{C})$, respectively. Figure 2.12 shows the measured temperature and cooling rates at different locations in the castings. In both trials, shortly after filling, thermocouple B1 (TC_B1), failed due to damage during filling. Also, it can be observed that the TC_B2, which is located at the middle thin plate section, cools faster than TC_B3 and TC_B4 in the step-blocks. By using the described procedure in references [32] and [33], the measured solidus and liquidus temperatures for Mn-Steel alloy are defined as $T_{sol} = 1523\ \mathrm{K}(1250^{\circ}\mathrm{C})$ and $T_{liq} = 1669\ \mathrm{K}(1396^{\circ}\mathrm{C})$, respectively. Figure 2.13 shows the variation of mold temperature vs. time for casting 1 and 2. It seems TC_K4 in casting 1 failed after some time.

Both Mn-Steel castings are inspected for porosity with dye-penetration and X-ray radiography techniques. Figure 2.14 shows radiography results for the Experiment 2. From this observation, in both castings a shrinkage hole can be observed in the block; and a trace of riser pipe is visible at the connection of rise to step blocks. These observations are confirmed by the dye-penetration test results in Figure 2.15. By take a closer look at the cut sections in Figure 2.15(a)-(b) and the dye-penetrant results in Figure 2.15(c)-(d), in both casting, there are small amount of centerline shrink at the thin middle section; which occurred late during solidification. In Casting 2, it seems some air entrapment happened during filling; that's why the riser pipe and porosity in the block look different compared to the ones in Casting 1.

Experiment 3: Large Plate without Step-blocks

In the experiment 3, two Mn-Steel castings with larger sizes compare to the experiment 2 are considered for experimental trials. The sand mold, the casting geometry and the thermocouple locations are demonstrated in Figure 2.16(a)-(d). The alloy composition for the experiment 3, is provided in the Table 2.2. The pouring temperature was $T_{pour} = 1688\ \text{K}\,(1415^{\circ}\text{C})$ and filling time was 30 s. Unfortunately, due to the size of the casting, most of the B-type thermocouples failed during filling. So, we could not measure temperatures during filling and solidification. Like Experiment 2, the casting consists of different parts such as: a gating system, a riser, a thin middle section and a block at the far end of the casting. It is expected that, once the casting starts solidifying, the riser compensates the entire shrink in the system until the flow resistance at the middle section becomes high enough that stops the flow from reaching the block. Then, a porosity nucleates in the block and feeds the remaining shrink in the system. After solidification, both castings were cut and inspected for porosity defects using dye-penetration and X-ray radiography techniques. The test results for Experiment 3 are provided in Figure 2.17 and Figure 2.18. The results show that, in both castings, there is a large shrinkage pipe in the riser as well as a centerline shrink at the middle section and an open hole in the block.

2.3.2 Thermal Simulation

By comparing the measurement results in Experiment 2 and 3, it is noticed that the measurements in Experiment 2 are more accurate than those in Experiment 3. Thus, Experiment 2 results are considered for thermo-physical property development of Mn-Steel alloy. To begin with, the steel module of IDS and JMatPro™ software are used for defining an initial data-base for temperature dependent properties. Then, the calculated properties are adjusted to the measured data from the experimental studies. Like the

aluminum wedge casting, the IHTC curve is determined using an iterative trial-and-error procedure. The final IHTC curve as a function of temperature is a constant value of 1100 W/m^2K for temperatures above $1623K\,(1350^\circ C)$; below $1623K\,(1350^\circ C)$, IHTC decreases to 200 W/m^2K at liquidus temperature; then it drops to 150 W/m^2K at around $1073K\,(800^\circ C)$ and remains at this value for the lower temperatures. The final properties for Mn-Steel alloy are shown in Figure 2.19. As it can be observed in Figure 2.19(a) and (b), once temperature decreases, the solid-fraction and density increases monotonically; while, the thermal conductivity [Figure 2.19(c)] first remains constant for temperature above the liquidus and for temperatures below solidus the thermal conductivity decreases as temperature drops. In the density curve, it is assumed that the alloy does not contract for temperature below solidus. Figure 2.20 also shows the variation of Olivin's thermal conductivity and heat capacity with temperature. The density of Olivin is assumed to be a constant at 1830 kg/m^3. The calculated Mn-Steel latent heat of fusion is defined as 203 kJ/kg which gives a reasonable agreement between simulation and measurement results. By using the developed properties for Mn-Steel alloy and implement the experimental conditions in MAGMAsoft, the casting was simulated. Figure 2.21 and Figure 2.22 show the comparison between measured and simulation temperatures and cooling rates by thermocouples. It can be observed that for all B-type and K-type TCs simulation and measurement results agree well with each other.

Table 2.1. A356 aluminum alloy composition, given in weight percent of aluminum (Wt Pct Al)

Element	Amount (Wt Pct)
Cu	0.001
Fe	0.090
Mg	0.380
Mn	0.006
Ni	0.004
Si	7.050
Sr	0.001
Ti	0.110
Zn	0.002
Al	balance

Table 2.2. Mn-Steel composition, given in

weight percent of Fe (Wt Pct Fe)

Element	Experiment 2 Amount (Wt Pct)	Experiment 3 Amount (Wt Pct)
C	1.1	1.13
Mn	13.2	12.99
Si	0.65	0.68
P	0.042	0.050
S	0.005	0.004
Cr	0.33	0.46
Ni	0.11	0.10
Mo	0.84	0.36
Al	0.030	0.052
Cu	0.11	0.10
Ti	0.00	0.20
Fe	balance	balance

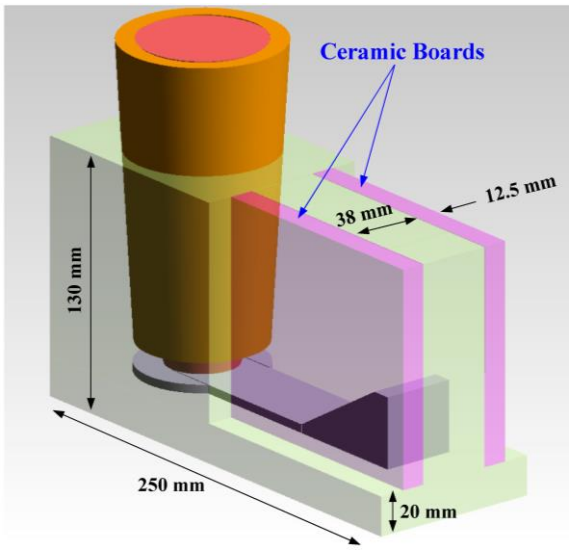

(a)

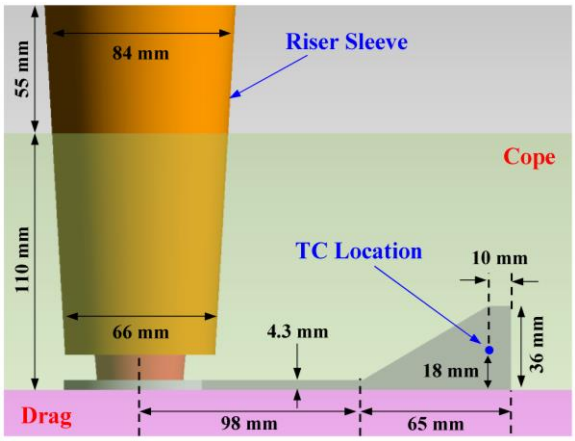

(b)

Figure 2.1. Casting schematic (a) 3D view, (b) side view

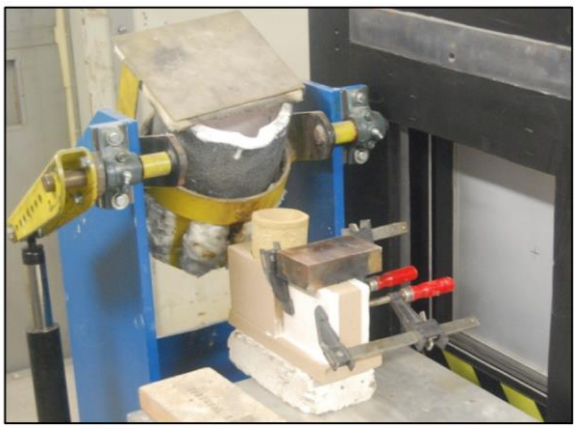

(a)

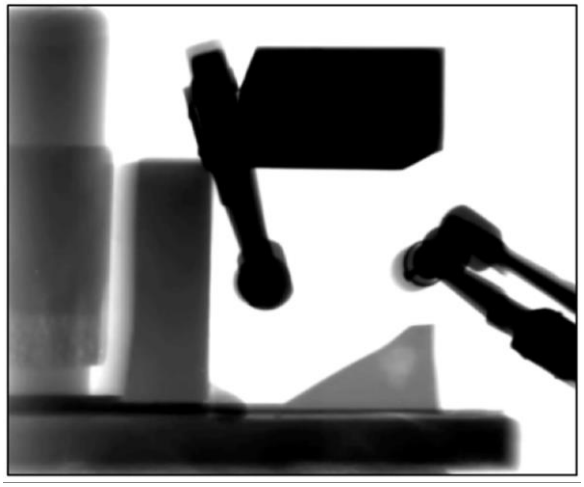

(b)

Figure 2.2. Real-time X-ray radiography setup (a) mold and imaging facilities, (b) a sample radiograph image

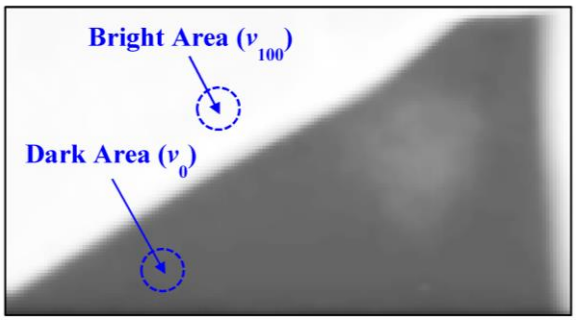

(a)

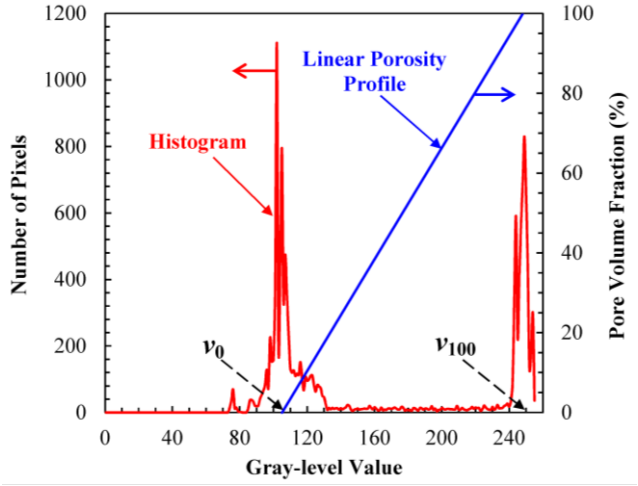

(b)

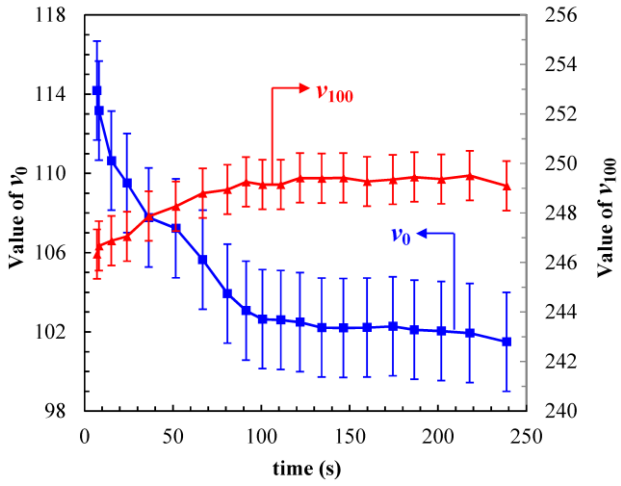

(c)

Figure 2.3. (a) Bright and dark areas on a sample radiograph image, (b) Linear porosity profile and a sample histogram, (c) variation of v_0 and v_{100} values on the real-time radiograph with time

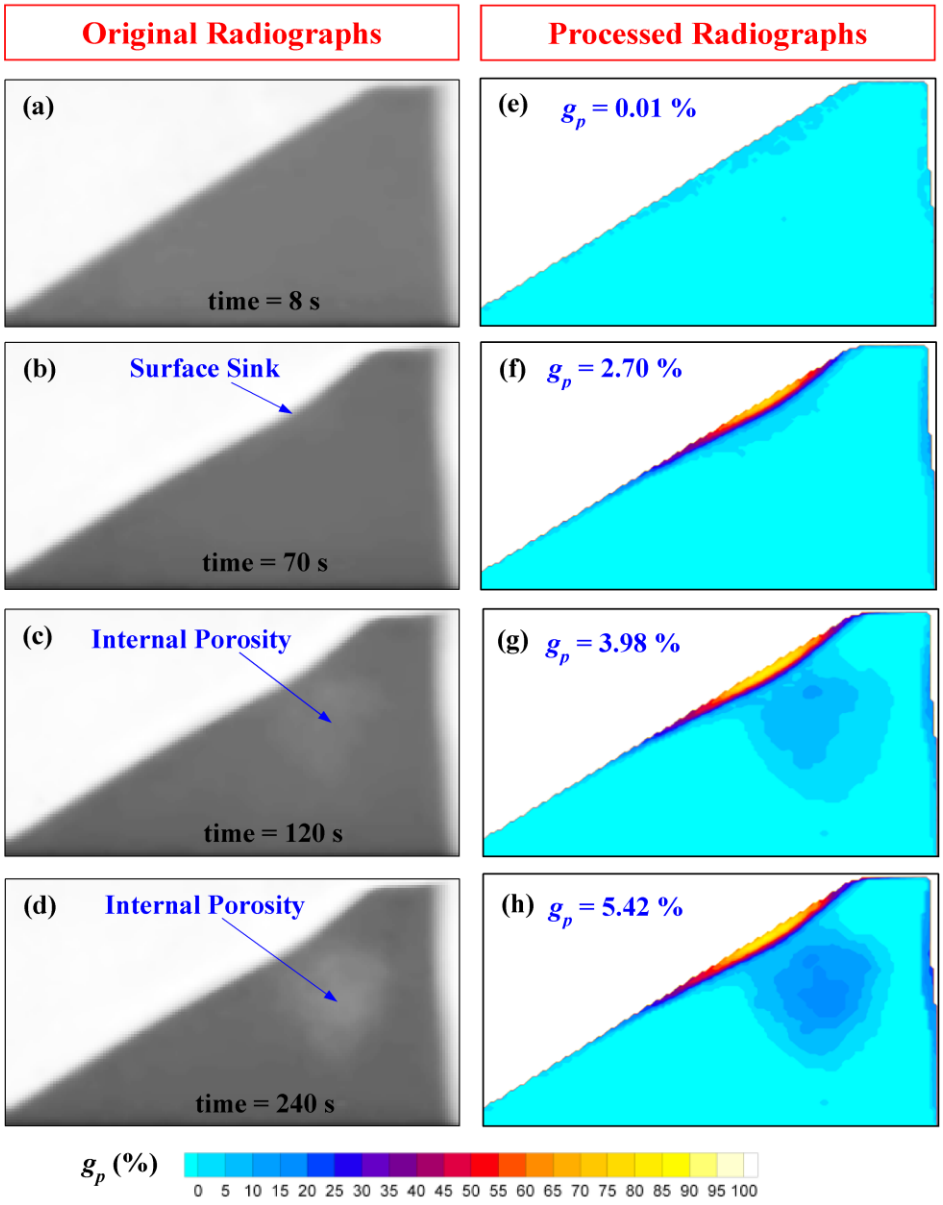

Figure 2.4. Real-time X-ray radiographs of A356 aluminum alloy wedge casting (a)-(d) original radiographs (e)-(h) processed radiographs.

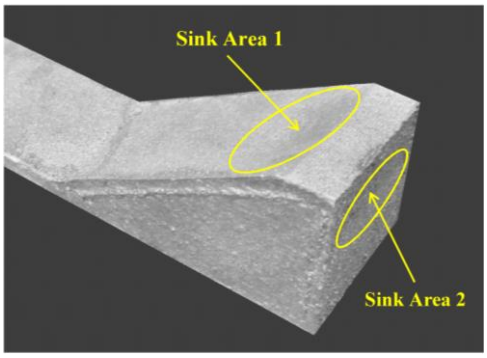

(a)

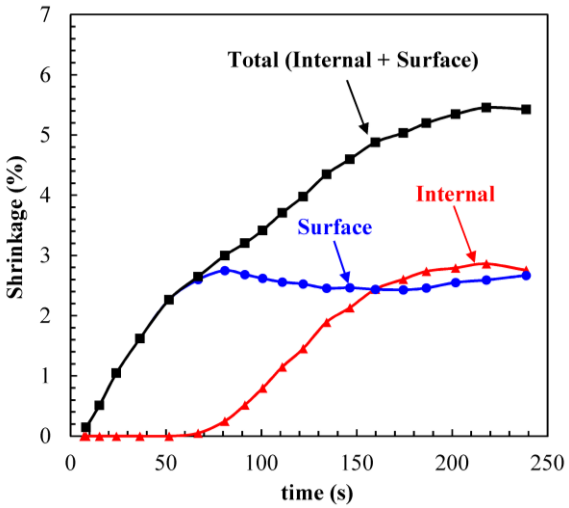

(b)

Figure 2.5. (a) Sink areas on the wedge surfaces (b) variation of the internal, surface and total shrinkage with time

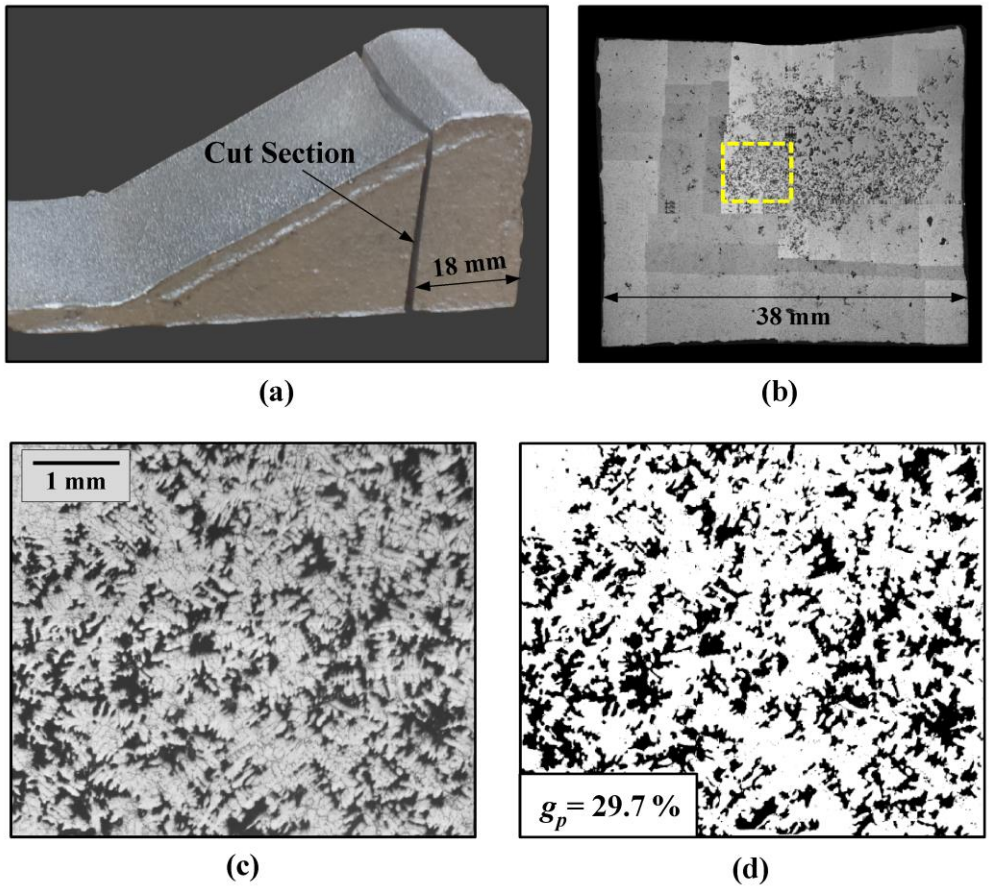

Figure 2.6. (a) Cut section location, (b) composite microscope image of polished surface, (c) the close-up view of the shrinkage porosity at the center of cut section (d) binary image of the close-up image

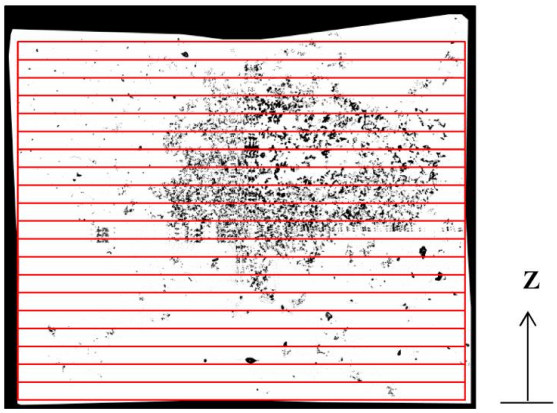

(a)

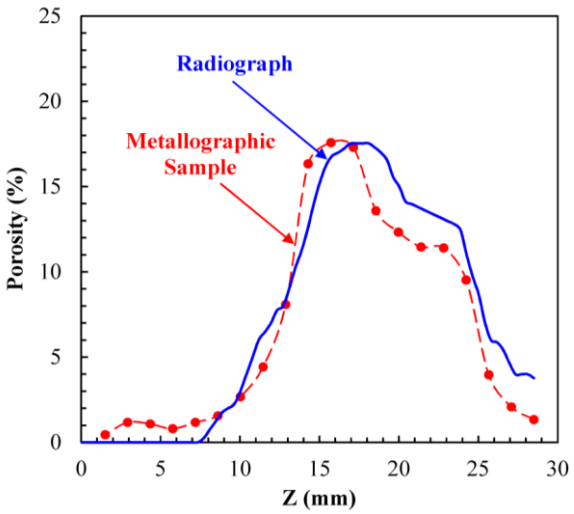

(b)

Figure 2.7. (a) measurement boxes on the metallographic image, (b) Comparison of porosity distribution along the cut section between processed radiograph image and metallographic

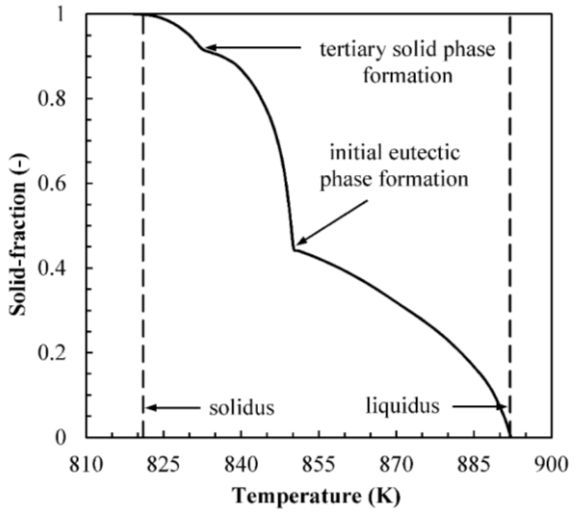

(a)

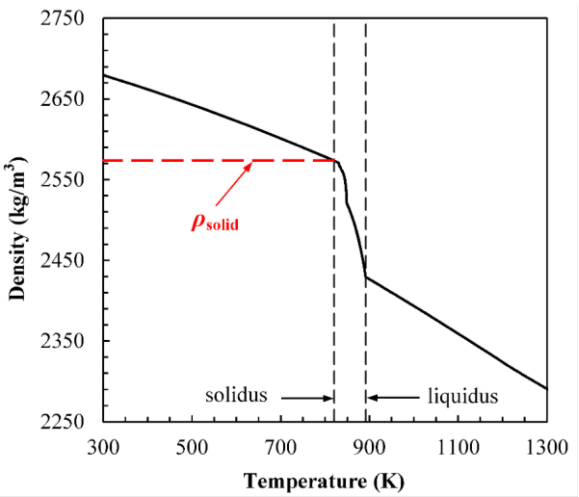

(b)

Figure 2.8. A356 aluminum alloy temperature-dependent properties (a) solid-fraction, (b) density; properties are generated in JMatPro™ software [31] using the alloy chemistry.

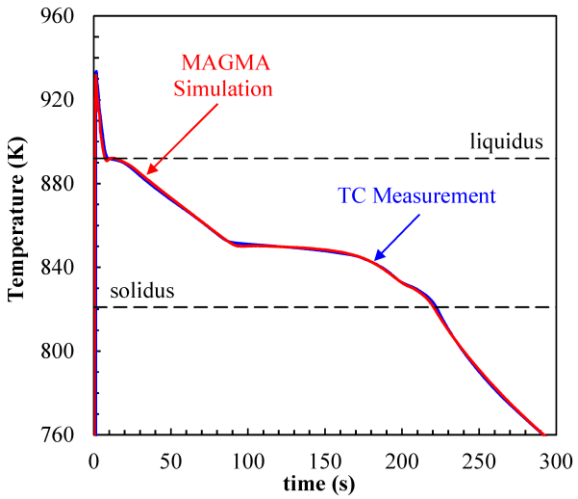

Figure 2.9. Measured and simulated temperature results at the location of thermocouple

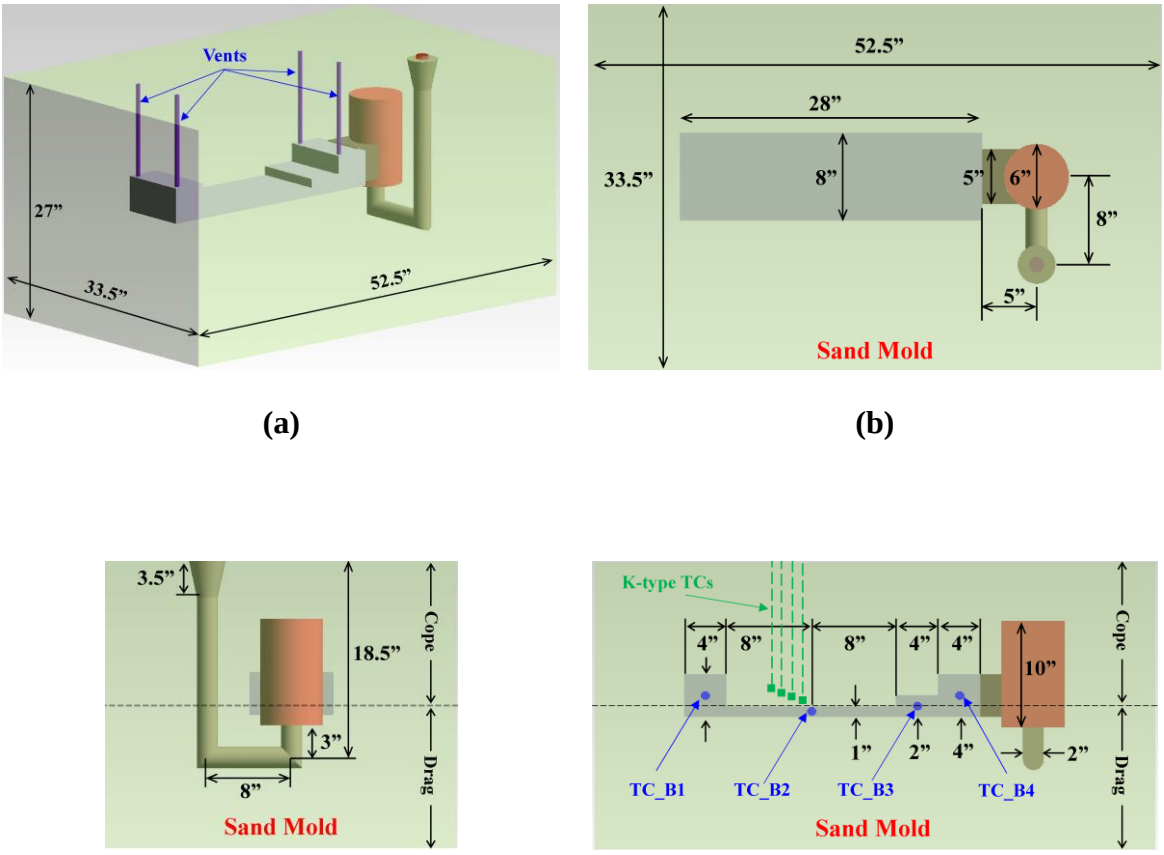

Figure 2.10. Casting geometry for the experiment 1 (a) 3D view, (b) top view, (c) side view, (d) front view

(a)

(b)

(c)

(d)

Figure 2.11. Photographs of experimental and measurement setup: (a)-(c) sand molds, and (d) data logger and wiring setups

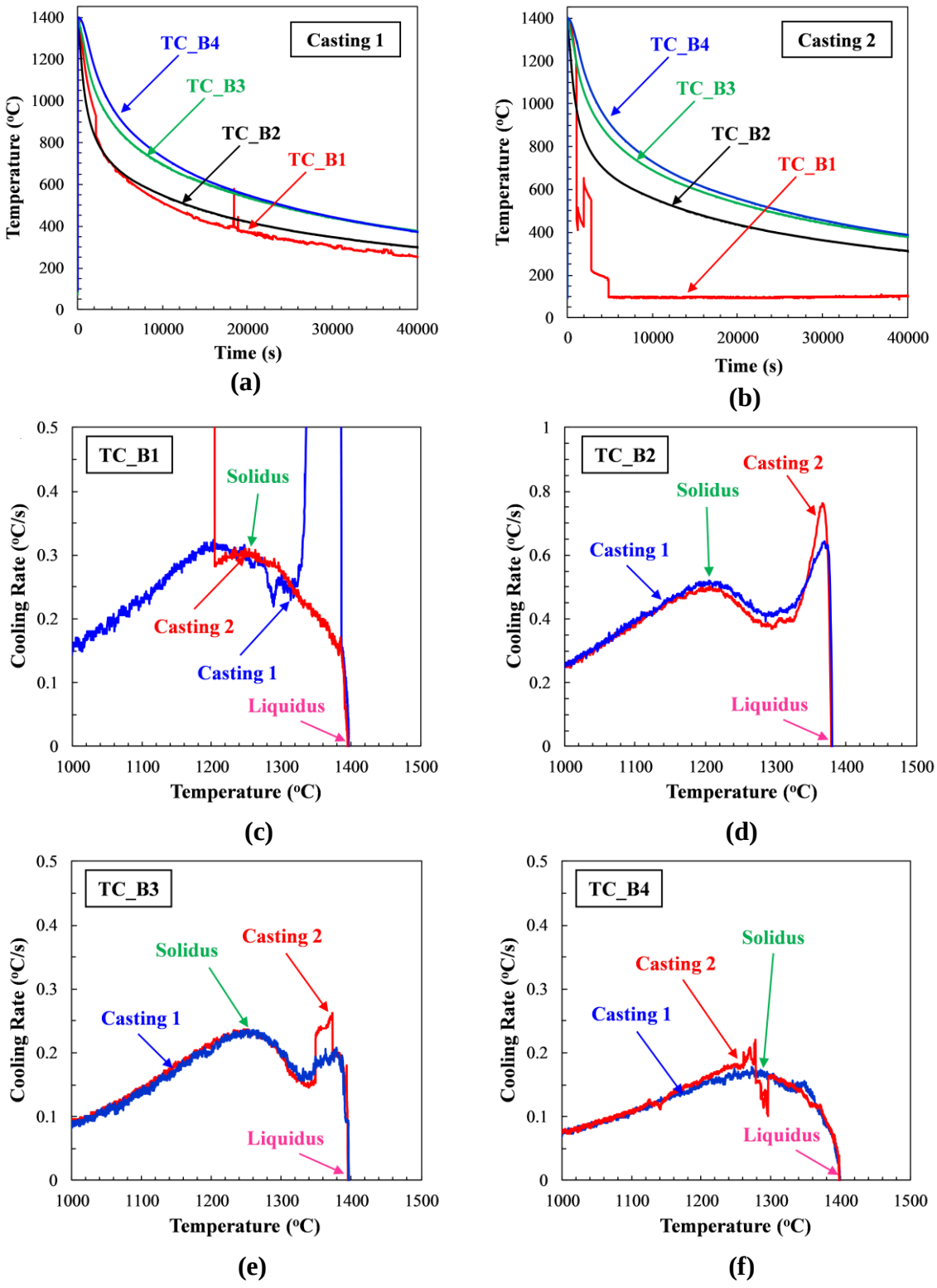

Figure 2.12. B-type thermocouple measurements at different locations in casting:(a)-(b) temperature vs. time, (c)-(f) cooling rate vs. temperature

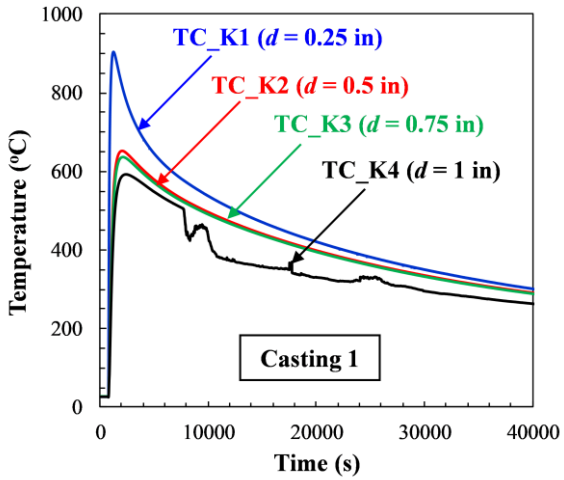

(a)

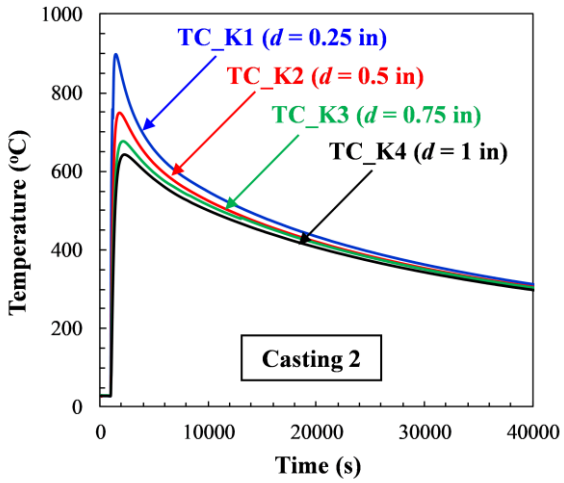

(b)

Figure 2.13. K-type thermocouple measurements at different locations in the sand mold: (a) Casting 1, (b) Casting 2

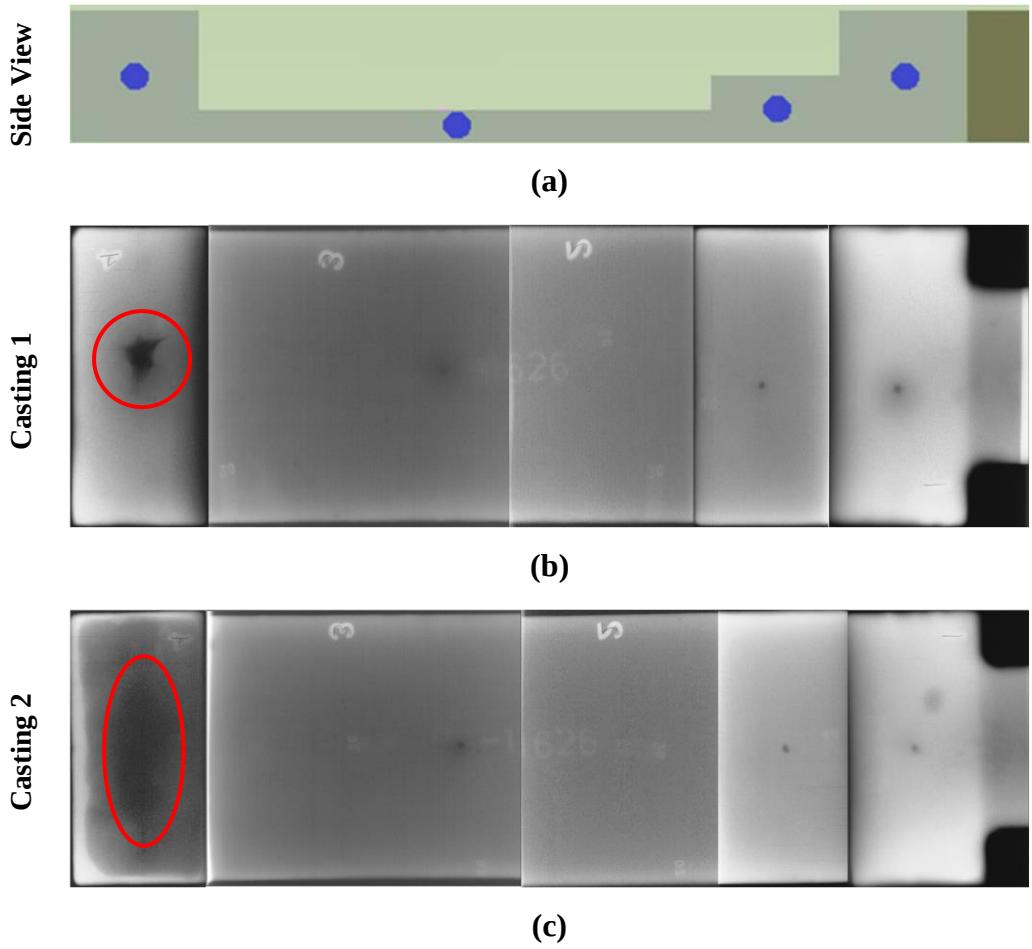

Figure 2.14. Experiment 2: (a) schematic showing the location of thermocouples in casting, (b) Radiographic image of casting 1, (c) radiographic image of casting 2

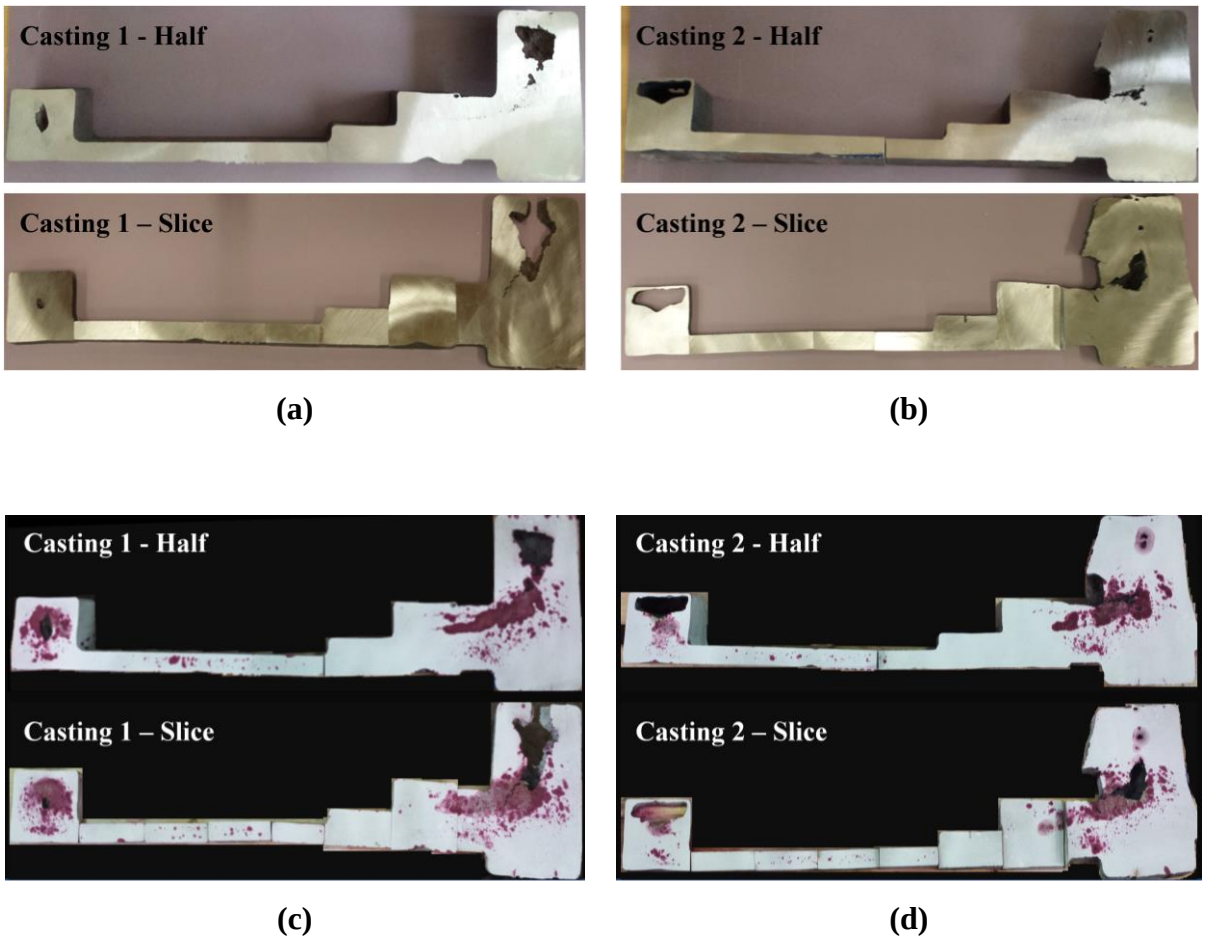

Figure 2.15. Experiment 2: (a)-(b) Porosity distribution on the cut section of Casting 1 and 2, (c)-(d) Dye-penetration test results for Casting 1 and 2

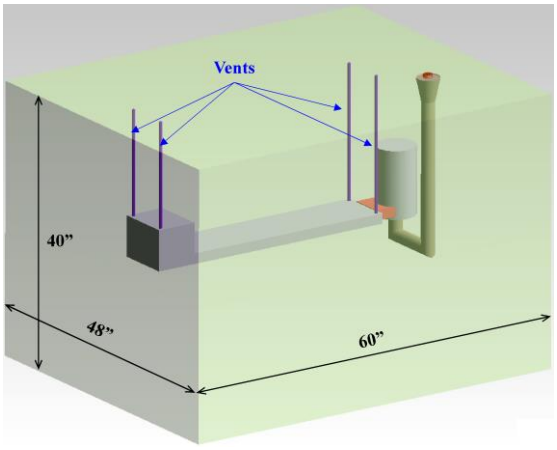

(a)

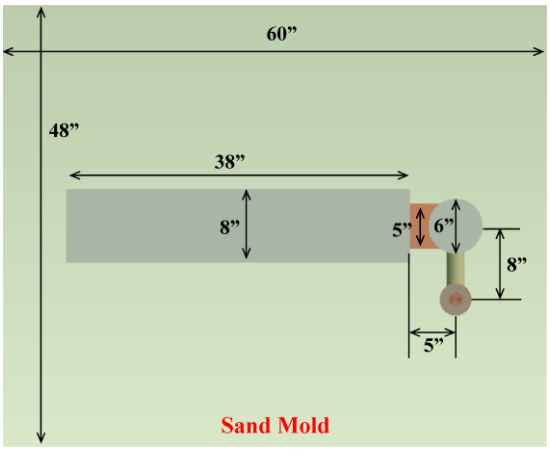

(b)

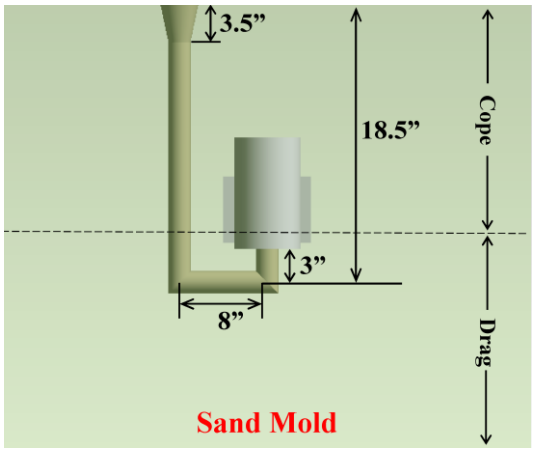

(c)

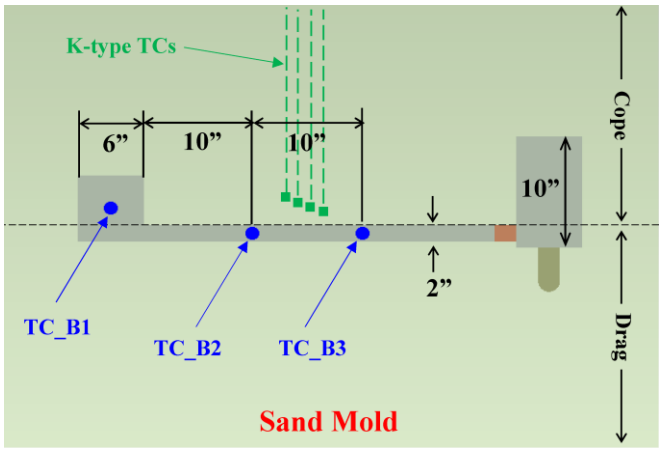

(d)

Figure 2.16. Casting geometry for the experiment 2 (a) 3D view, (b) top view, (c) side view, (d) front view

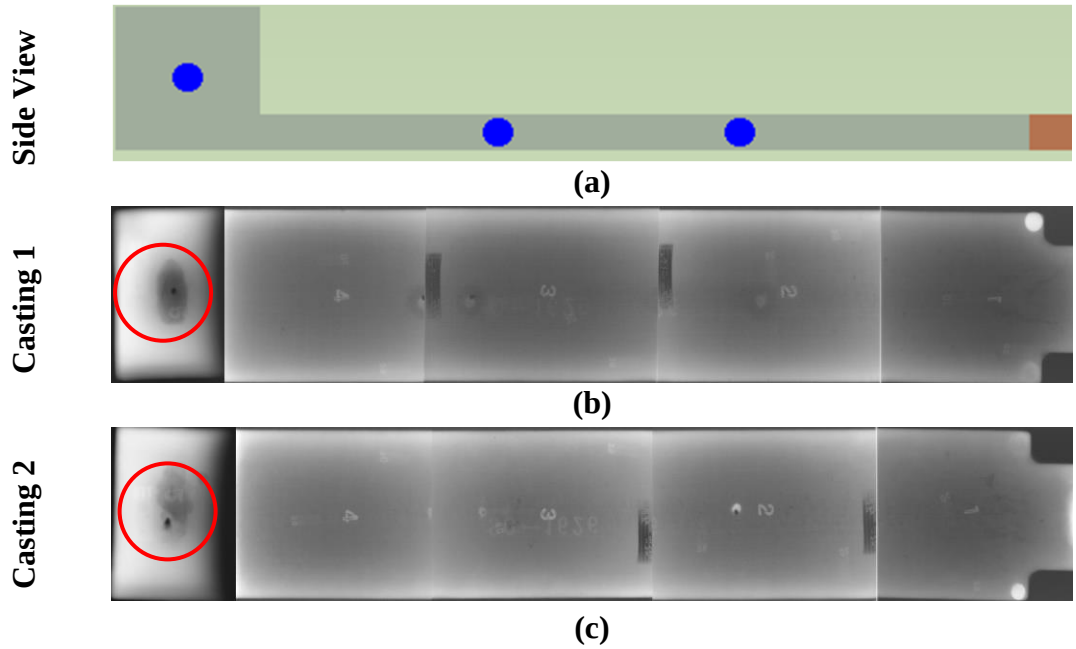

Figure 2.17. Experiment 3: (a) schematic showing the location of thermocouples in casting, (b) Radiographic image of casting 1, (c) radiographic image of casting 2

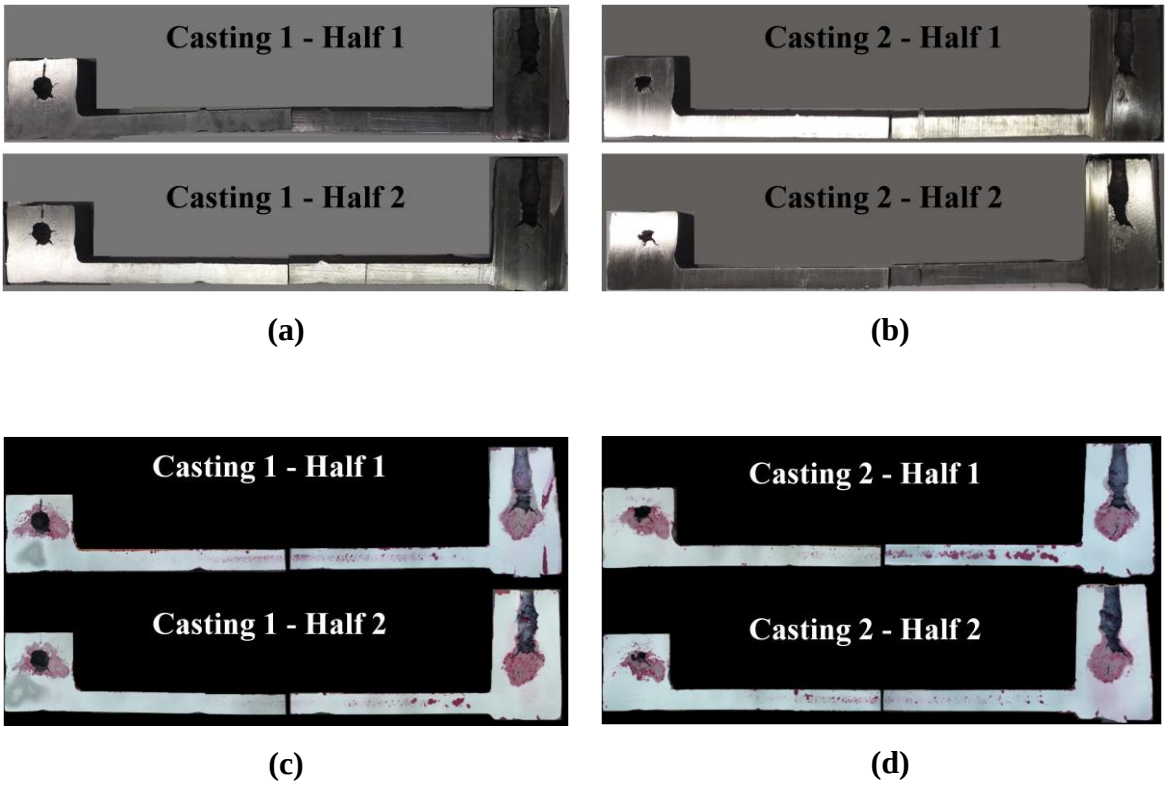

Figure 2.18. Experiment 3: (a)-(b) Porosity distribution on the cut section of Casting 1 and 2, (c)-(d) Dye-penetration test results for Casting 1 and 2

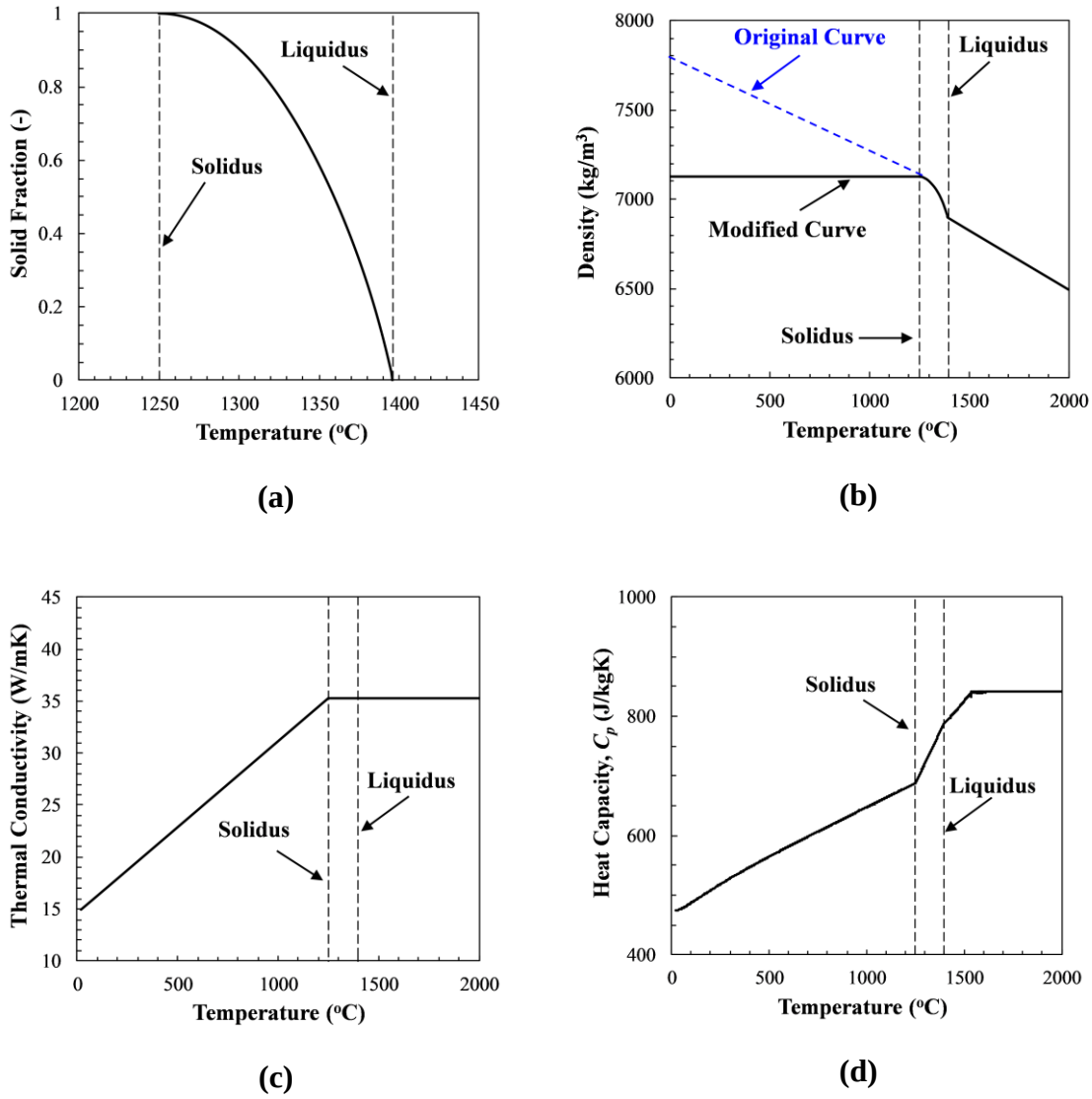

Figure 2.19. Manganese steel (Mn-Steel) alloy temperature-dependent properties (a) solid-fraction, (b) density, (c) thermal conductivity, and (d) heat capacity.

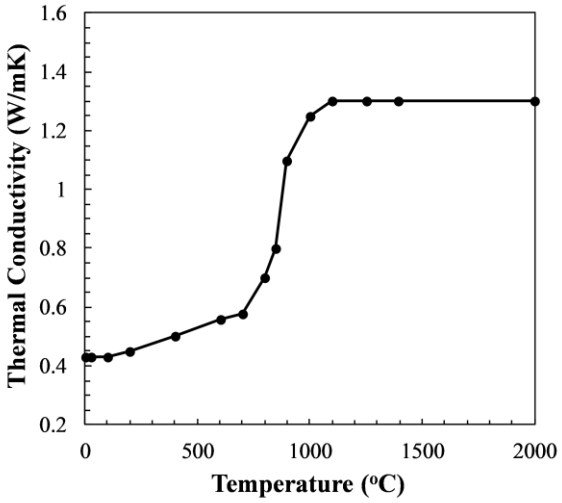

(a)

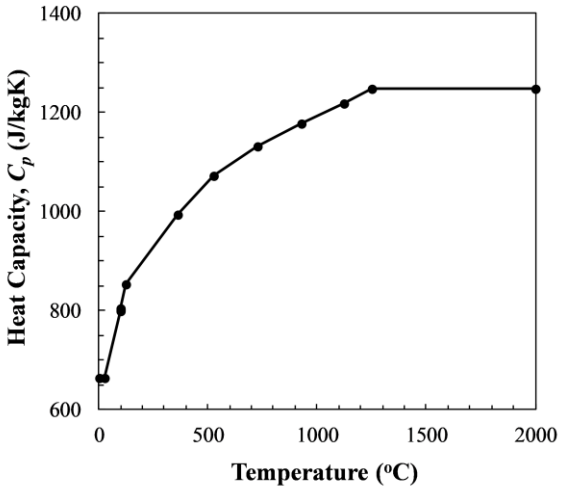

(b)

Figure 2.20. Olivin sand mold temperature-dependent properties: (a) thermal conductivity, and (b) heat capacity.

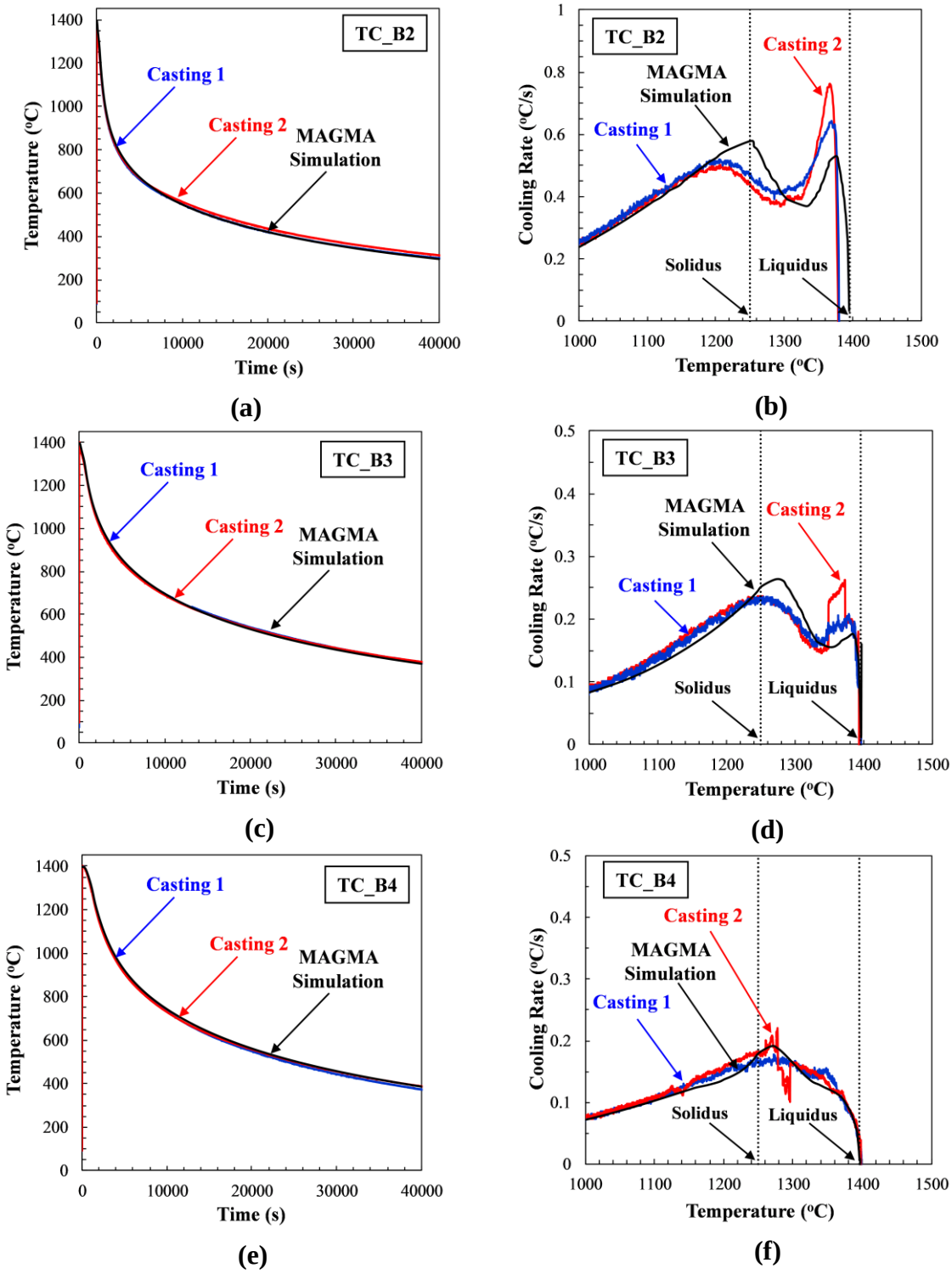

Figure 2.21. Comparison of B-type TC measurements and simulation results: (a) temp. vs. time at the TC_B2 location, (b) cooling rate vs. temperature at the TC_B2 location, (c) temp. vs. time at the TC_B3 location, (d) cooling rate vs. temp. at the TC_B3 location, (d) temperature vs. time at the TC_B4 location, (e) cooling rate vs. temperature at the TC_B4

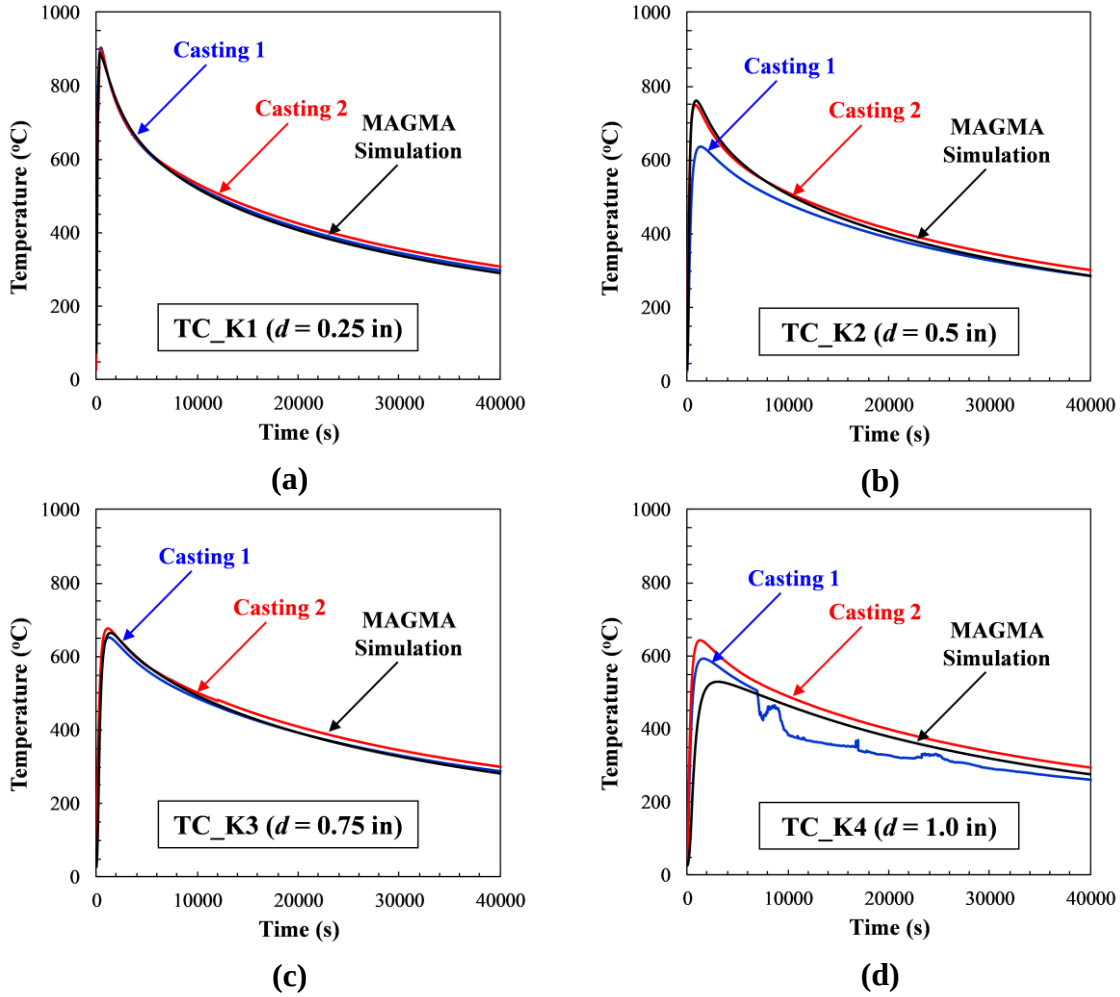

Figure 2.22. Comparison of K-type TC measurements and simulation results: (a) temp. vs. time at the TC_K1 location, (b) temp. vs. time at the TC_K2 location, (c) temperature vs. time at the TC_K3 location, and (d) temperature vs. time at the TC_K4 location

CHAPTER 3. FORMATION OF SURFACE SINK AND INTERNAL POROSITY

3.1 Pore Nucleation Model

To improve the correlation of the MAGMASOFT porosity results to experimental observations, a new porosity model is needed. Based on the real-time radiographic observations presented in Chapter 2, the evolution of shrinkage porosity in aluminum wedge casting has two main stages: 1- surface sink, 2-internal porosity formation. The main reason is that in the first stage, when the casting becomes isolated from in-gate, surfaces are not coherent, so the dendritic solid network can easily move to compensate the solidification shrinkage [Schematic in Figure 3.1(a)]. Thus, the casting surfaces keep sinking until the surfaces become coherent, i.e. $g_s \geq g_{s,sur}$. In the second stage, due to a compact solid network [Schematic in Figure 3.1(b)], the surfaces become rigid and the shrinkage porosity nucleates internally and spreads over the area close to casting's thermal center, which solidifies last in solidification. Therefore, a two-stage model is developed that predicts the porosity formation in the mushy zone. In the pore nucleation, pores require sufficient energy to overcome the capillary pressure due to the surface tension to nucleate and grow during solidification. Therefore, this phenomenon could be explained by the Young-Laplace's pore nucleation criterion as following:

$$P_p - P_{\ell,T} \geq P_\sigma \qquad (3.1)$$

where, $P_{\ell,T}$ is the total liquid pressure which is calculated as $P_{\ell,T} = P_\ell + \rho_\ell g(z_{\max} - z)$; P_ℓ is the dynamic liquid pressure which is assumed to be uniform and equal to $P_\ell = P_{atm}$ and $P_\ell = 0$, for surface sink and internal porosity stages, respectively. P_P is the pore pressure which for surface sinks $P_P = P_{atm}$ and for internal porosity $P_P = 0$; and P_σ is the capillary pressure due to surface tension in the mushy zone.

According to the experimental observations presented in Figure 3.2(a), shrinkage porosity defects tend to nucleate and grow in the casting's thermal center, where

solidifies last during solidification. This means pores nucleate easier in liquid regions than solid ones. By looking at the corresponding solid-fraction field in the Figure 3.2(b), it can be observed that the location and shape of the pore forming region have a close relationship with solid-fraction field. To model this phenomenon, it is assumed that the capillary pressure (P_σ) is a function of the solid-network curvature ($\kappa_s \propto 1/r_p$) which is a function of solid-fraction (g_s)[Figure 3.2(c)]. So, in the current model, before nucleation the capillary pressure is assumed to be a linear function of solid-fraction as $P_\sigma = P_{\sigma,0} \times g_s$; where $P_{\sigma,0}$ is a constant coefficient. After nucleation, P_σ is assumed to be $P_\sigma = 0$ to satisfy the nucleation condition. By foregoing assumptions and using Young-Laplace equation for pore nucleation, a new parameter, Π, is introduced as following:

$$\Pi = P_{\ell,T} - \left(P_p - P_\sigma \right) \qquad (3.2)$$

According to Π definition, once $\Pi \le 0$ for an area, pores nucleate and grow until the end of solidification. In cases that $\Pi > 0$ everywhere in a casting or $\Pi \le 0$ at multiple cells in the domain, pores nucleate in regions with low Π values within the range of $\left|(\Pi - \Pi_{\min})/(\Pi_{\max} - \Pi_{\min})\right| < \varepsilon$; where, $\Pi_{\max} = P_{atm} + \rho_\ell g(z_{\max} - z) + P_{\sigma,0}$ and $\Pi_{\min}$ is the minimum Π value among the searching area; and ε is a small number which usually defined from a parametric study.

3.2 Pore Growth Model

The present model uses an input temperature dependent density curve to calculate the total shrink and the pore growth rate ($d\bar{g}_p/dt$) during solidification. If there is no influx and outflux to the system, the mass conservation can be expressed by the mass balance equation as following:

$$\frac{d}{dt}\int_{V_{Cast}} \bar{\rho} dV = 0 \qquad (3.3)$$

where, V_{Cast} is the initial casting volume, $\bar{\rho}$ is the alloy mixture density. There are two

strategies to calculate $\bar{\rho}$ during solidification: 1- two-phase mixture of solid and liquid ($\bar{\rho}^{SL}$), 2- three-phase mixture of solid, liquid and porosity ($\bar{\rho}$). The two-phase mixture density, $\bar{\rho}^{SL}$, is defined as $\bar{\rho}^{SL} = \rho_s g_s^{SL} + \rho_\ell g_\ell^{SL}$ where $g_s^{SL} + g_\ell^{SL} = 1$; while, the three-phase mixture density, $\bar{\rho}$, is calculated by $\bar{\rho} = \rho_s g_s + \rho_\ell g_\ell + \rho_p g_p$ where $g_\ell + g_s + g_p = 1$. Combining these two strategies and assuming that $g_s^{SL} = g_s$ and $\rho_p << \rho_s, \rho_\ell$, the following equation is obtained for $\bar{\rho}$:

$$\bar{\rho} = \bar{\rho}^{SL} - \rho_\ell g_p \tag{3.4}$$

In Equation (5), $\bar{\rho}$ is expressed as a function of $\bar{\rho}^{SL}$, reference liquid density (ρ_ℓ) and the pore-fraction (g_p). By combining equation (3.3) and (3.4) and assuming that $\bar{g}_p = \left(\int_{V_{Cast}} g_p dV\right) \Big/ V_{Cast}$, the average pore growth rate ($d\bar{g}_p / dt$) is given by:

$$\frac{d\bar{g}_p}{dt} = \frac{1}{\rho_\ell V_{Cast}} \int_{V_{Cast}} \left(\frac{\partial \bar{\rho}^{SL}}{\partial t} \right) dV \tag{3.5}$$

By calculating $d\bar{g}_p / dt$ from equation (3.5), the shrink volume (ΔV_{Shrink}) at each time step (Δt) is given as following

$$\Delta V_{Shrink} = \left[\left(d\bar{g}_p / dt \right) \times \Delta t \right] \times V_{Cast} \tag{3.6}$$

So, at each time step, the total casting's shrink volume is defined as $V_{Shrink} = \sum_0^t \Delta V_{Shrink}$. By having V_{Shrink} at each time, the total casting's shrinkage (β) is given by $\beta = V_{Shrink} / V_{Cast}$. Figure 3.3 presents the variation of total casting's shrinkage percentages by time for both measurement and simulation cases. Despite all the uncertainties, a good agreement between the measured and simulated results is observed.

3.3 Simulation Details

As mentioned before, the porosity formation model has two main stages: 1) surface sink and 2) internal porosity. At each stage, the model uses Π values to nucleate and grow porosity in the casting. If $\Pi > 0$ everywhere in the domain, pores nucleate in areas with low Π values within a range of $\left|(\Pi - \Pi_{\min})/(\Pi_{\max} - \Pi_{\min})\right| < \varepsilon_{nuc}$; where, $\Pi_{\max} = P_{atm} + \rho_{\ell} g(z_{\max} - z) + P_{\sigma,0}$ and $\Pi_{\min}$ is the minimum Π value among the searching area; and ε_{nuc} is a small number. In the surface sink regime, only surface cells with $g_s < g_{s,sur}$ are considered for pore nucleation and growth; while, in the internal porosity stage, all surface and internal cells are considered for pore nucleation within the casting. It should be noted that, in the surface sink stage, pores stop growing once they reach to coherent limit (i.e. $g_s \geq g_{s,sur}$). After defining the total volume of active cells as ΔV_{Active}, the shrink volume (ΔV_{Shrink}) is distributed evenly across all active cells as $\Delta g_p = \Delta V_{Shrink} / \Delta V_{Active}$. Then, the pore-fraction field is updated according to calculated Δg_p. If during shrink volume distribution, all porosity regions become empty of liquid (i.e. $g_s + g_p = 1$) or if they become inactive due to coherency limit, the neighboring cells with Π values within a low range of $\left|(\Pi - \Pi_{\min})/(\Pi_{\max} - \Pi_{\min})\right| < \varepsilon_{layer}$ are known as active cells. Typical examples of active cells distribution for surface sink and internal porosity stage are shown in Figure 3.4 for the wedge casting.

Furthermore, the model assumes that the mass-feeding (solid movement) can only occur when the local solid-fraction is below a coherency criterion (i.e. $g_s < g_{s,coh}$). By this assumption, if a cell in the computational domain has the solid-fractions above the coherency limit (i.e. $g_s \geq g_{s,coh}$), it cannot be emptied completely. Thus, the maximum pore-fraction, $g_p^{\max}$, for each cell is determined as following:

$$\begin{cases} g_p^{\max} = 1 & g_s < g_{s,coh} \\ g_p^{\max} = 1 - g_s & g_s \geq g_{s,coh} \end{cases} \qquad (3.7)$$

3.4 Results and Discussion

Figure 3.5 shows a comparison of measured and predicted porosity distributions at four different times. The processed radiographic images and the computed solid-fraction distributions are also provided in this figure. At the time, the surface stops sinking (around 70 s), the minimum solid fraction on the surface of the wedge is about 40% [see Figure 3.5(j)]. Hence, the surface sink limit, $g_{s,sur}$, is chosen as 40%. Moreover, from the metallographic study [Figure 3.6 (a)], the maximum pore fraction at the center of cut section is about 30%. So, by adjusting the critical coherency limit to $g_{s,coh} = 40\%$, the maximum pore-fraction at the wedge's center agrees well with the experimental results. Numerous simulations were performed where ε_{nuc}, ε_{layer}, $g_{s,sur}$, $g_{s,\mathrm{coh}}$ and $P_{\sigma,0}$ were varied until the measured and predicted porosity distributions agreed best. The optimum combination of these adjustable parameters was found to be $\varepsilon_{nuc} = 0.009$, $\varepsilon_{layer} = 0.05$, $g_{s,sur} = 40\%$, $g_{s,\mathrm{coh}} = 40\%$ and $P_{\sigma,0} = P_{atm}$. With this combination of parameters both surface sink and internal porosity near the thermal center of wedge casting are predicted accurately. By comparing the recorded radiographic video and simulation results in Figure 3.5, it can be observed that when the wedge becomes isolated from the riser, the surfaces start to sink until about 70 second. During the surface sink stage, the solid-fraction at the sinking location increases from about 10% to about 40%, when the surface has reached to the surface sink coherency limit in this alloy (i.e. $g_s = g_{s,sur}$). Internal porosity only forms near the time that the surface sink stops. There seems to be a sharp transition between the sound layer of metal behind the surface sink and the internal porosity. This happens because, the surface sink is creating a compacted mush layer with a solid-fraction that is higher than what the thermal predictions would suggest. Internal porosity spreads over the region that has the lowest solid-fraction, with the maximum pore-fraction being eventually in the thermal center, where the wedge solidifies last. Internal porosity keeps increasing until the wedge is fully solidified. In

general, the proposed model can reasonably predict the location and the amount of both surface sink and internal porosity. Figure 3.6 shows the comparison of porosity distribution predicted by the model and observed on the metallographic image. From the porosity distribution in Figure 3.6(a) it can be observed that the maximum local porosity percentage of 29.7% happens at the center of cut section where its location and porosity percentage is very well predicted by the model, as can be seen in Figure 3.6(b). Finally, parametric studies were performed to better understand how the final porosity distribution in wedge casting is affected by the variation of model parameters. The results of the parametric studies are presented in Figure 3.7, which includes four contours of the porosity distribution for different values of ε_{nuc}, ε_{layer}, $g_{s,sur}$, $g_{s,\mathrm{coh}}$ and $P_{\sigma,0}$. All simulations use the optimum values for the parameters unless otherwise stated on the figures: $\varepsilon_{nuc}=0.009$, $\varepsilon_{layer}=0.05$, $g_{s,sur}=40\%$, $g_{s,\mathrm{coh}}=40\%$ and $P_{\sigma,0}=P_{atm}$. In Figure 3.7(a)-(d), the effects of ε_{layer} and ε_{nuc} parameters on the results are shown. It can be observed choosing smaller values for ε_{layer} and ε_{nuc} causes a concentrated porosity distribution at the central part of the wedge which results to high through-thickness porosity percentage in those locations; while, the larger values of ε_{layer} and ε_{nuc} make the final distribution more spared over the central areas. It should be noted that variation of ε_{nuc} has effect on the final surface sink distribution while ε_{layer} effect is negligibly small. Moreover, results in Figure 3.7(e) and (f) reveals that a smaller surface sink and mass feeding criteria of $g_{s,sur}=g_{s,coh}=30\%$ will cause the transition from surface to internal porosity happens early in solidification which causes the final surface sink becomes smaller than the optimum case while the internal porosity amount is overrated. This trend is opposite for a larger surface sink and mass feeding criteria of $g_{s,sur}=g_{s,coh}=50\%$. Finally, the effect of capillary pressure coefficient, $P_{\sigma,0}$, is investigated in Figure 3.7(g) and (h). The results show that for smaller value of $P_{\sigma,0}$ the surface sink is smaller and more spread on the surface compare to the larger value of $P_{\sigma,0}$. However, this effect on the final internal porosity distribution is opposite and larger value of $P_{\sigma,0}$ makes the

internal porosity more spread over the internal part of the wedge casting.

Formation of shrinkage porosity in A356 aluminum wedge casting is observed using a real-time video radiographic technique. By developing an image processing procedure, the recorded video is processed to obtain the porosity distribution in the casting. Results of image processing and thermal simulation show that the evolution of shrinkage porosity in A356 aluminum castings has two main stages: 1) surface sink formation and 2) internal porosity evolution. The surface sink occurs when the casting becomes isolated from the feeder and continues until the casting's surfaces become coherent. Then, the internal porosity forms adjacent to the inclined surface and spreads over the area with lowest solid-fractions. Based on the experimental observations, a two-stage model is developed to predict shrinkage porosity in castings. Comparison between the simulation and experimental results shows that the proposed method can reasonably predict the location and distribution of shrinkage porosity in castings.

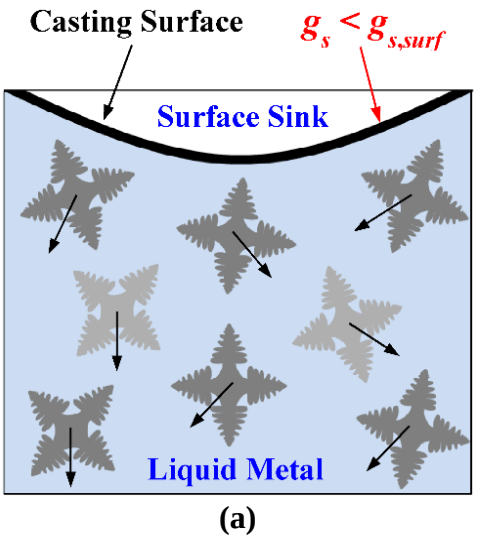

Figure 3.1. Schematic of surface sink and internal porosity formation: (a) for $g_s < g_{s,sur}$ surface can easily move and surface sink happens, (b) once $g_s \geq g_{s,sur}$ surface stops moving and internal porosity forms at the central part of the casting

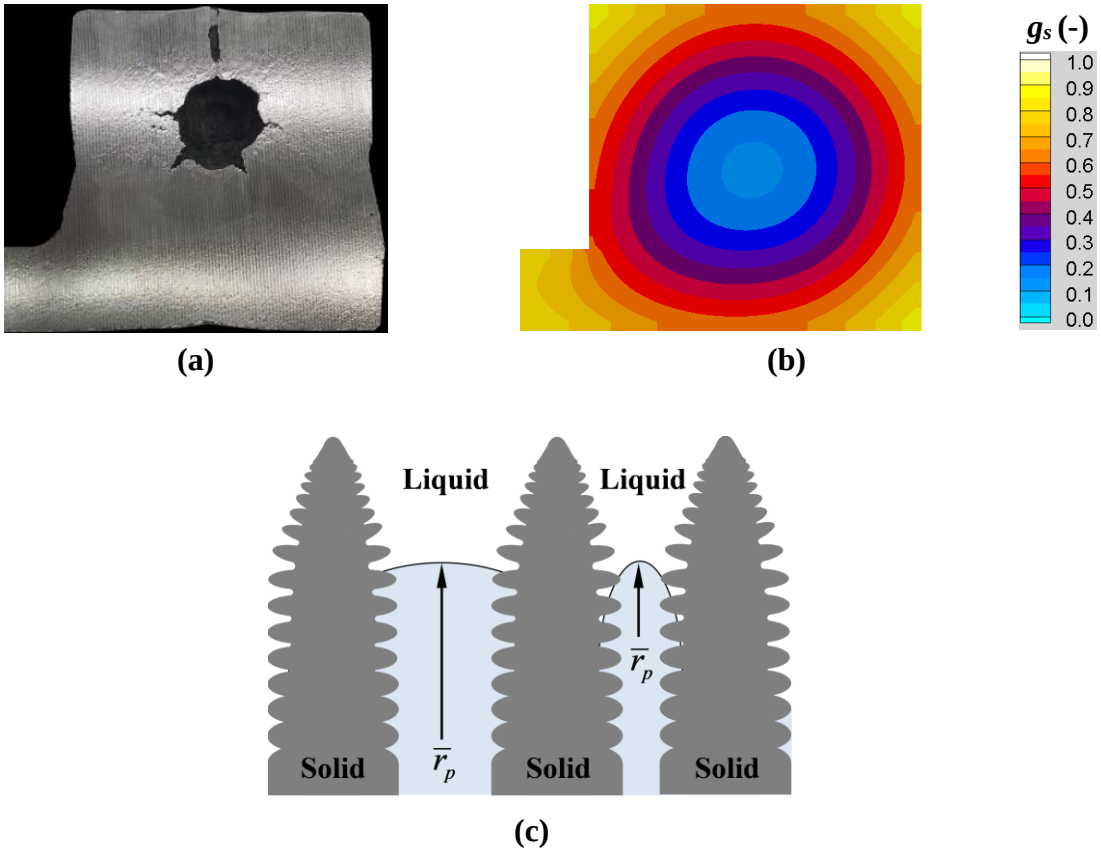

Figure 3.2. (a) photo of typical shrinkage porosity in a block, (b) a sample solid-fraction distribution in a block, (c) schematic showing the solid network curvature

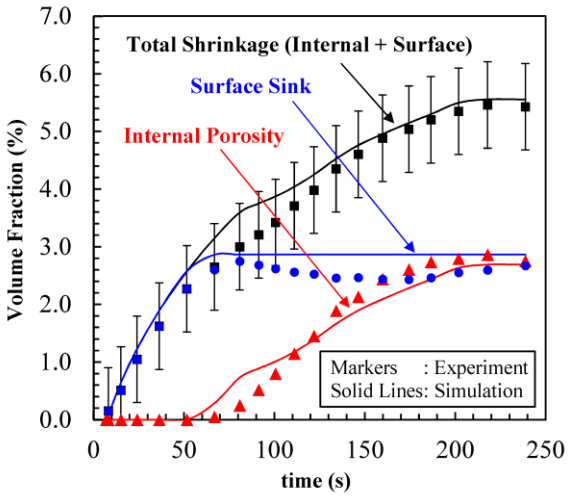

Figure 3.3. Comparison of total shrinkage between radiograph measurement and thermal simulation results for surface sinks, internal and total shrinkage porosity

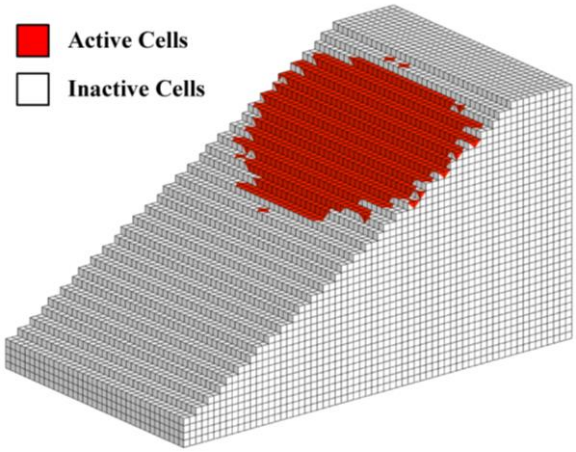

(a)

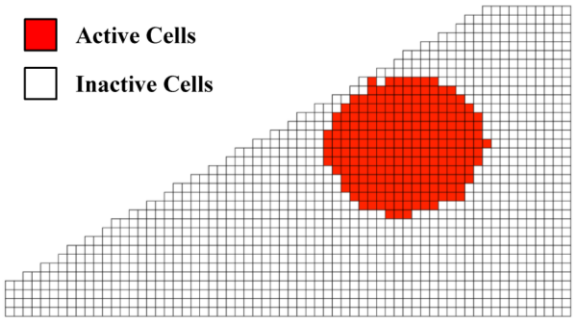

(b)

Figure 3.4. Typical active cell distributions: (a) surface sink, (b) internal porosity

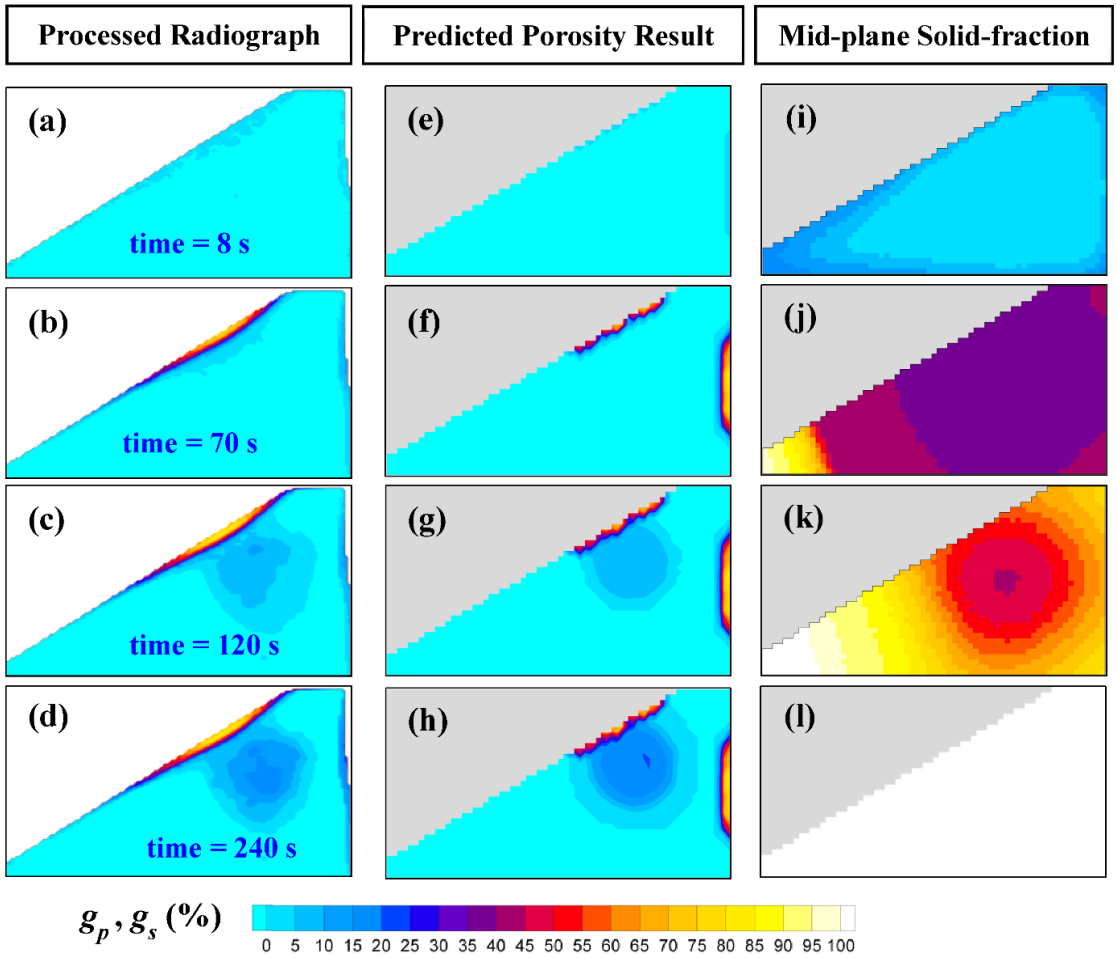

Figure 3.5. Comparison of measured and predicted results at 8s (first row), 70 s (second row), 120 s (third row), and 240 s (forth row): (a)-(d) processed radiographic images showing the measured porosity distribution, (e)-(h) predicted through-thickness average porosity distribution, (i)-(l) predicted mid-plane solid fraction distributions; the model uses , $\varepsilon_{nuc} = 0.009$, $\varepsilon_{layer} = 0.05$, $g_{s,sur} = 40\%$, $g_{s,coh} = 40\%$ and $P_{\sigma,0} = P_{atm}$.

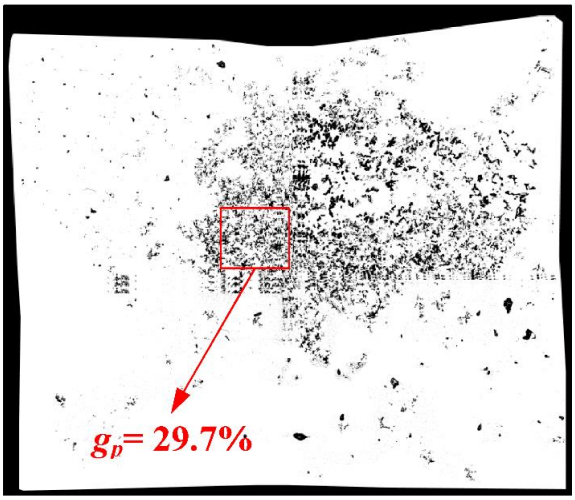

(a)

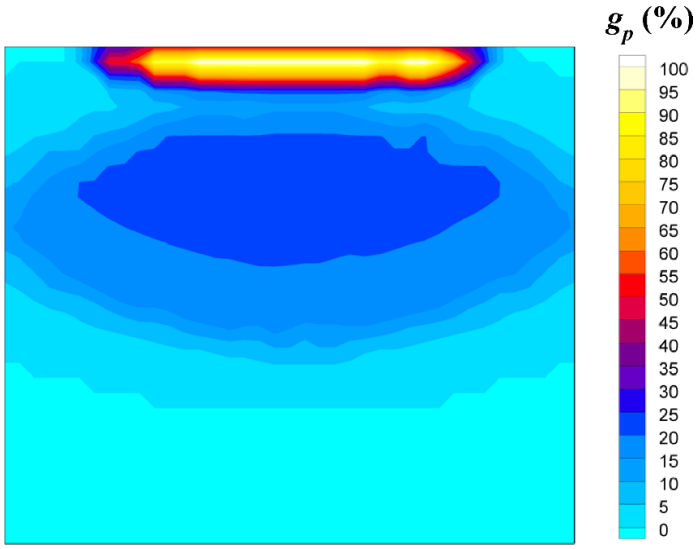

(b)

Figure 3.6. Porosity distribution on the cut surface (a) binary microscope image (b) simulation result; simulation uses $\varepsilon_{nuc} = 0.009$, $\varepsilon_{layer} = 0.05$, $g_{s,sur} = 40\%$, $g_{s,coh} = 40\%$ and $P_{\sigma,0} = P_{atm}$.

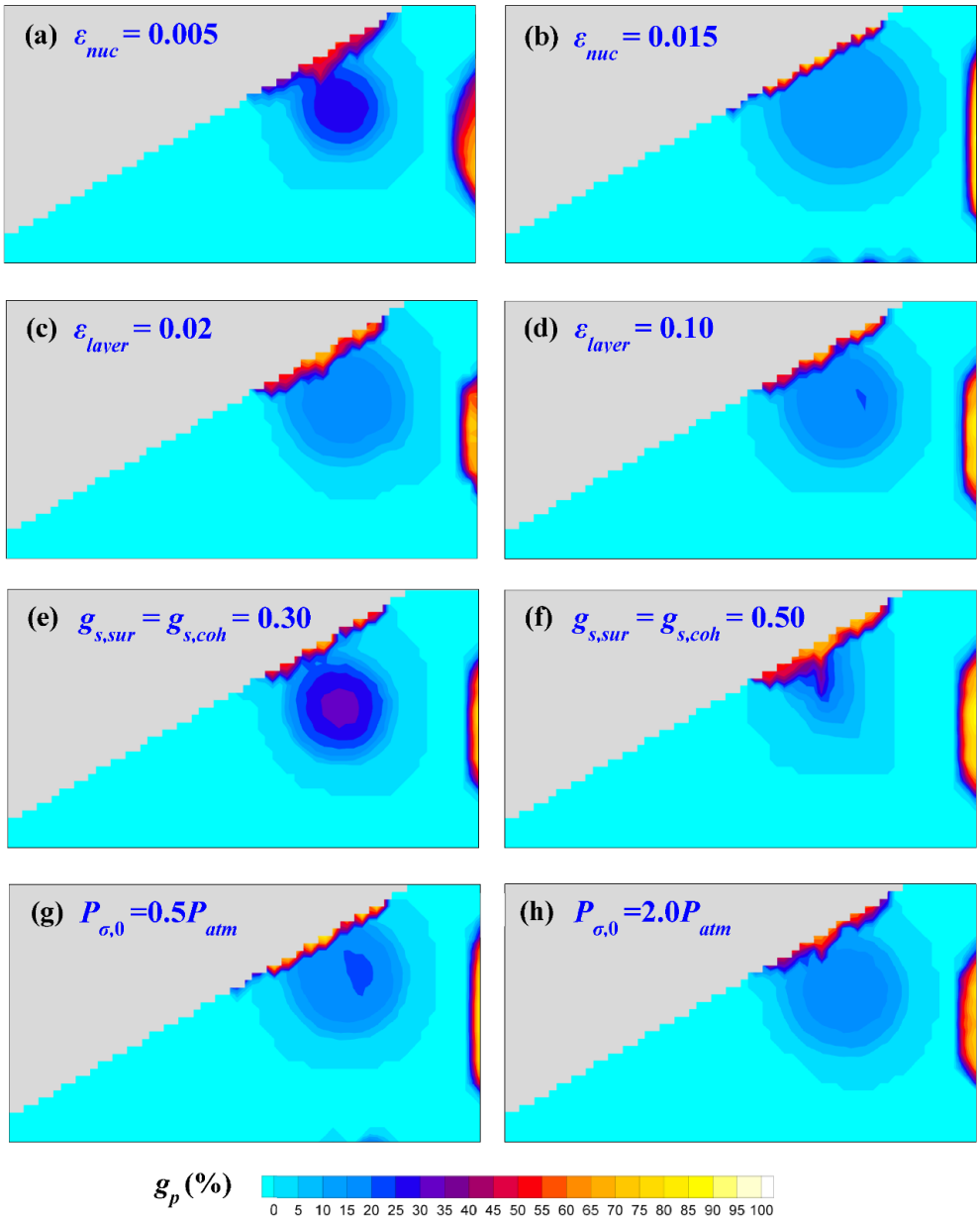

Figure 3.7. Case studies for different model parameters (a) $\varepsilon_{nuc} = 0.005$, (b) $\varepsilon_{nuc} = 0.015$, (c) $\varepsilon_{layer} = 0.02$, (d) $\varepsilon_{layer} = 0.10$, (e) $g_{s,sur} = g_{s,coh} = 30\%$, (f) $g_{s,sur} = g_{s,coh} = 50\%$, (g) $P_{\sigma,0} = 0.5P_{atm}$ and (h) $P_{\sigma,0} = 2P_{atm}$; all simulations use the following parameters unless otherwise stated on the plot $\varepsilon_{nuc} = 0.009$, $\varepsilon_{layer} = 0.05$, $g_{s,sur} = 40\%$, $g_{s,coh} = 40\%$ and $P_{\sigma,0} = P_{atm}$.

CHAPTER 4. ADVANCED FEEDING MODEL

4.1 Introduction

As the model developed in previous chapter did not consider the effects of feeding velocity and liquid pressure variations, a comprehensive model that accounts for those effects is needed. So, the model, hereafter called an "advanced feeding model", is developed which takes material properties and transient temperature field as input and predicts feeding velocity, liquid pressure and shrinkage porosity distributions in castings. According to schematics in Figure 4.1, the model assumes that a control volume in the casting domain may composed of three phases: solid (s), liquid (ℓ) and porosity (p) such that the volume fractions satisfy $g_\ell + g_s + g_p = 1$. Then, the multi-phase continuity and momentum equations are solved to obtain the feeding velocity, liquid pressure and pore-fraction distributions in casting.

In development of the advanced feeding model, some simplifications and assumptions are made which some of them are listed as following:

- The solid and porosity phases are stationary
- Flow movement is only due to the shrinkage in the system and the buoyancy-driven flow during solidification is neglected
- For temperatures below solidus, the material density is assumed to be a constant value; while, for higher temperatures it may vary with temperature

By foregoing assumptions, mathematical equations and numerical procedure are described in the following sections.

4.2 Continuity and Momentum Equations

During solidification, it is assumed that a representative control volume in the mushy zone is composed of solid, liquid and porosity phases which form a porous environment called the "mushy zone". The flow in the mushy zone follows the concepts

of flow in porous media. Therefore, the mixture continuity equation for the flow in the mushy zone is given by:

$$\frac{\partial \overline{\rho}}{\partial t} + \nabla \cdot \left(\rho_\ell \boldsymbol{u}_\ell \right) = 0 \tag{4.1}$$

where $\overline{\rho}$ is the alloy mixture density, ρ_ℓ is the reference liquid density and $\boldsymbol{u}_\ell$ is the superficial liquid velocity vector which is defined as $\boldsymbol{u}_\ell = g_\ell \boldsymbol{v}_\ell$; where $\boldsymbol{v}_\ell$ is the liquid velocity vector. For the momentum equation in the mushy zone, it is assumed that the flow is only shrinkage-driven, and the Darcy's law is applied as following:

$$\nabla P_{\ell,T} = -\frac{\mu_\ell \boldsymbol{u}_\ell}{K} + \rho_\ell \boldsymbol{g} \tag{4.2}$$

where, $P_{\ell,T}$ is the total liquid pressure, μ_ℓ is the dynamic viscosity of liquid, K is the mushy zone permeability and $\boldsymbol{g}$ is the gravity vector. To simplify Eq. (4.2), ($P_{\ell,T}$) is considered to be a sum of dynamic liquid pressure (P_ℓ) and hydrostatic pressure (P_h) which is defined as: $P_{\ell,T} = P_\ell + P_h$. By apply a gradient operator to this equation, the result becomes:

$$\nabla P_{\ell,T} = \nabla P_\ell + \nabla P_h \tag{4.3}$$

where, the hydrostatic pressure gradient (∇P_h) is given by $\nabla P_h = \rho_\ell \boldsymbol{g}$. By combine Eq. (4.2) and (4.3), the gravity term Eq. (4.2) is eliminated and the simplified momentum equation for P_ℓ becomes:

$$\nabla P_\ell = -\frac{\mu_\ell \boldsymbol{u}_\ell}{K} \tag{4.4}$$

The mushy zone permeability, K, in Eq. (4.4) is given by famous Kozeny–Carman's equation as following:

$$K = K_0 \frac{(1-g_s)^3}{g_s^2} \tag{4.5}$$

where K_0 is a permeability coefficient which is assumed to be an alloy-dependent parameter. To avoid large numbers or dividing by zero problems in the permeability calculations, the maximum and minimum K values are bounded to $K_{\min}$ and $K_{\max}$, respectily. To solve Eq. (4.4), a reference liquid pressure is needed. As the capillary pressure at the pore-liquid interfaces is negligibly small, P_ℓ at the porosity region is forced to $P_\ell\big|_{Porosity} = P_p$; where, P_p is the pore pressure; which, for internal porosity $P_p = 0$, for mold-metal interface porosity is $P_p = P_{mold}$, and for the atmosphere-metal interface porosity $P_p = P_{atm}$ [see schematic in Figure 4.1(d)].

By assuming that ρ_ℓ is constant during solidification and combining Eqs. (4.1) and (4.4), a Poisson-type PDE for the dynamic liquid pressure is derived as:

$$\nabla \cdot \left(-\frac{K}{\mu_\ell} \nabla P_\ell \right) = -\frac{1}{\rho_\ell} \frac{\partial \overline{\rho}}{\partial t} \tag{4.6}$$

From mathematical point of view, Eq. (4.6) is an Elliptic PDE which requires two boundary conditions to have a valid solution. The first boundary condition comes from the Darcy's law equation, i.e. $P_\ell\big|_{Porosity} = P_p$, and the other one is provided by the zero-mass flux condition at the casting walls, i.e. $(\boldsymbol{u}_\ell \cdot \boldsymbol{n})_{Surface} = (\nabla P_\ell \cdot \boldsymbol{n})_{Surface} = 0$. With these two boundary conditions, P_ℓ distribution in casting can be defined from the solution of Eq. (4.6). Once P_ℓ is defined everywhere in the domain, the Darcy's law [Eq. (4.4)] is solved for $\boldsymbol{u}_\ell$ to obtain the velocity distribution in the casting as following:

$$\boldsymbol{u}_\ell = -\frac{K}{\mu_\ell} \nabla P_\ell \tag{4.7}$$

Finally, by integrating the (4.3), the total pressure, $P_{\ell,T}$, can be determined as:

$$P_{\ell,T} = P_\ell + P_h \tag{4.8}$$

where, P_h is the hydrostatic pressure given by $P_h = \rho_\ell g(z_{\max} - z)$, where $(z_{\max} - z)$ is the hydrostatic head from a reference height of $z_{\max}$.

4.3 Pore Nucleation Model

As homogenous pore nucleation during solidification is almost impossible in industrial castings [34], in the current study, a heterogeneous mechanism is considered for pore nucleation. Thus, existing nucleation sites in the mushy zone only grow once the needed energy to overcome the capillary pressure is provided. In absence of any dissolved gas in the system, the nucleation energy is provided by large pressure drop due to flow resistance in the mushy zone. The inequality form of Young-Laplace equation is used for the pore nucleation criterion during solidification:

$$P_p - P_{\ell,T} \geq P_\sigma \tag{4.9}$$

where, $P_{\ell,T}$ is the total liquid pressure which is defined as $P_{\ell,T} = P_\ell + \rho_\ell g(z_{\max} - z)$; P_P is the pore pressure, and P_σ is the capillary pressure due to surface tension in the mushy zone. According to the experimental observations presented in Figure 3.2(a) and (b), shrinkage porosity defects tend to nucleate first in areas with low solid-fractions during solidification. In the other words, pores nucleate easier in liquid regions than solid ones. Moreover, it has been observed that the location and shape of the pore forming region have a close relationship with solid-fraction field. Therefore, to model this phenomenon, it is assumed that the capillary pressure (P_σ) in the mushy zone is a function of the solid-network curvature ($\kappa_s \propto 1/r_p$) which is related to the solid-fraction (g_s). So, in the current study, P_σ is modeled as a linear function of solid-fraction (g_s) as following:

$$P_\sigma = P_{\sigma,0} \times g_s \tag{4.10}$$

where $P_{\sigma,0}$ is a constant coefficient. Furthermore, it has been assumed that after nucleation, due to a small surface curvature at the pore-liquid interfaces, P_σ become negligibly small that can be considered as $P_\sigma = 0$. By foregoing assumptions and using Young-Laplace equation for pore nucleation, a new parameter, Π, is introduced as following:

$$\Pi = P_{\ell,T} - \left(P_p - P_\sigma \right) \qquad (4.11)$$

According to Π definition, once $\Pi \le 0$ pores nucleate in respective area and grow until the end of solidification. In the cases that $\Pi > 0$ everywhere in casting or $\Pi \le 0$ at multiple cells in the domain, pores nucleate in regions with low Π values within the range of $\left|(\Pi - \Pi_{\min})/(\Pi_{\max} - \Pi_{\min})\right| < \varepsilon$; where, $\Pi_{\max}$ is defined as $\Pi_{\max} = P_{atm} + \rho_\ell g \, z_{\max} + P_{\sigma,0}$ and $\Pi_{\min}$ is the minimum Π value among the searching area; and ε is a small number which usually defined from parametric study.

4.4 Pore Growth Model

For any given active porosity region in the domain, the pore growth rate ($d\bar{g}_p / dt$) is defined by applying the mass conservation at the porosity region. Figure 4.1(c) shows a closeup view of a porosity region with volume of V_p and pore-liquid interface area of A_p. The normal flux at the pore-liquid interface is defined as $(\boldsymbol{u}_\ell \cdot \boldsymbol{n})$. The mass conservation law at the porosity region can be expressed as:

$$\int_{V_p} \left(\frac{\partial \bar{\rho}}{\partial t} \right) dV + \int_{A_p} (\rho_\ell \boldsymbol{u}_\ell) \cdot \boldsymbol{n} \, dA = 0 \qquad (4.12)$$

Like the model used for A356 aluminum wedge casting in the section 3.2, the three-phase mixture density ($\bar{\rho}$) can be shown as a function of two-phase mixture density ($\bar{\rho}^{SL}$) and pore-fraction (g_p) as following:

$$\bar{\rho} = \bar{\rho}^{SL} - \rho_\ell g_p \qquad (4.13)$$

By incorporating Eqs. (4.13) in (4.12) and assuming that $\bar{g}_p = \left(\int_{V_p} g_p dV \right) \Big/ V_p$, the average pore growth rate for a given porosity region is defined as:

$$\frac{d\bar{g}_p}{dt} = \frac{1}{\rho_\ell V_p}\int_{V_P}\left(\frac{\partial\bar{\rho}^{SL}}{\partial t}\right)dV + \frac{1}{V_p}\int_{A_p}\boldsymbol{u}_\ell\cdot\boldsymbol{n}\,dA \tag{4.14}$$

In equation (4.14), the first term on the right-hand side is related to shrinkage within the porosity region and the second term is related to sum of all fluxes at the pore-liquid interfaces. The balance of these two terms will define the rate and the magnitude of pore growth for a given porosity region. Once $d\bar{g}_p/dt$ is defined, the corresponding feeding volume (ΔV_{Shrink}) at each time-step is calculated as:

$$\Delta V_{Shrink} = \left[\left(d\bar{g}_p/dt\right)\times\Delta t\right]\times V_p \tag{4.15}$$

Finally, the calculated ΔV_{Shrink} is distributed equally across the active porosity region and the pore-fraction field will be updated accordingly.

4.5 Numerical Implementation

4.5.1 Finite Volume Approach

Eq. (4.6) is valid everywhere in the domain which in 3D can be expressed as following:

$$\frac{\partial}{\partial x}\left(\frac{K}{\mu_\ell}\frac{\partial P_\ell}{\partial x}\right)+\frac{\partial}{\partial y}\left(\frac{K}{\mu_\ell}\frac{\partial P_\ell}{\partial y}\right)+\frac{\partial}{\partial z}\left(\frac{K}{\mu_\ell}\frac{\partial P_\ell}{\partial z}\right)=\frac{1}{\rho_\ell}\frac{\partial\bar{\rho}}{\partial t} \tag{4.16}$$

To solve this equation numerically, a standard finite volume approach with a staggered grid shown in Figure 4.2 is used. Details about finite-volume method and related information can be found in book by Patankar [35]. Eq. (4.16) is discretized to the system of linear equations as following:

$$a_B P_{\ell,B} + a_S P_{\ell,S} + a_W P_{\ell,W} - a_P P_{\ell,P} + a_E P_{\ell,E} + a_N P_{\ell,N} + a_T P_{\ell,T} = S_P \tag{4.17}$$

where, the coefficients in the above equation are:

(4.18)

$$a_E = \frac{K_e A_e}{\mu_l \Delta x} \;;\; a_W = \frac{K_w A_w}{\mu_\ell \Delta x} \;;\; a_N = \frac{K_n A_n}{\mu_\ell \Delta y} \;;\; a_S = \frac{K_s A_s}{\mu_\ell \Delta y} \;;\; a_T = \frac{K_t A_t}{\mu_\ell \Delta z} \quad ; \quad a_B = \frac{K_b A_b}{\mu_\ell \Delta z}$$

$$a_P = a_E + a_W + a_N + a_S + a_T + a_B \quad ; \qquad S_P = \left[\frac{1}{\rho_\ell} \frac{(\bar{\rho}_P^n - \bar{\rho}_P^{n-1})}{\Delta t} \right] \Delta V$$

$$A_w = A_e = \Delta y \times \Delta z \;\; ; \;\; A_s = A_n = \Delta x \times \Delta z \;\; ; \;\; A_t = A_b = \Delta x \times \Delta y \quad ; \quad \Delta V = \Delta x \times \Delta y \times \Delta z$$

$$K_e = \frac{2}{(1/K_P) + (1/K_E)} \;\; ; \;\; K_w = \frac{2}{(1/K_P) + (1/K_W)} \;\; ; \;\; K_n = \frac{2}{(1/K_P) + (1/K_N)}$$

$$K_s = \frac{2}{(1/K_P) + (1/K_S)} \;\; ; \;\; K_t = \frac{2}{(1/K_P) + (1/K_T)} \;\; ; \;\; K_b = \frac{2}{(1/K_P) + (1/K_B)}$$

To solve the system of equations presented in Eq. (4.17), a computational fluid dynamics (CFD) code is developed to obtain the liquid pressure (P_ℓ) distribution in the entire casting. Once P_ℓ distribution is defined everywhere in the casting domain, the velocity components in 3D are defined from the Darcy's law as following:

$$u_\ell = -\frac{K}{\mu_\ell}\left(\frac{\partial P_\ell}{\partial x}\right) \quad ; \quad v_\ell = -\frac{K}{\mu_\ell}\left(\frac{\partial P_\ell}{\partial y}\right) \quad ; \quad w_\ell = -\frac{K}{\mu_\ell}\left(\frac{\partial P_\ell}{\partial z}\right) \tag{4.19}$$

For a staggered grid and the example volume cell shown in Figure 4.2, the velocity components at the cell center P are given by:

(4.20)

$$u_{\ell,e} = -\frac{K_e}{\mu_\ell}\left[\frac{P_{\ell,E} - P_{\ell,P}}{\Delta x}\right] \quad ; \quad u_{\ell,w} = -\frac{K_w}{\mu_\ell}\left[\frac{P_{\ell,P} - P_{\ell,W}}{\Delta x}\right] \quad \rightarrow \quad u_{\ell,P} = \frac{u_{\ell,w} + u_{\ell,e}}{2}$$

$$v_{\ell,n} = -\frac{K_n}{\mu_\ell}\left[\frac{P_{\ell,N} - P_{\ell,P}}{\Delta y}\right] \quad ; \quad v_{\ell,s} = -\frac{K_s}{\mu_\ell}\left[\frac{P_{\ell,P} - P_{\ell,S}}{\Delta y}\right] \quad \rightarrow \quad v_{\ell,P} = \frac{v_{\ell,n} + v_{\ell,s}}{2}$$

$$w_{\ell,t} = -\frac{K_t}{\mu_\ell}\left[\frac{P_{\ell,T} - P_{\ell,P}}{\Delta z}\right] \quad ; \quad w_{\ell,b} = -\frac{K_b}{\mu_\ell}\left[\frac{P_{\ell,P} - P_{\ell,B}}{\Delta z}\right] \quad \rightarrow \quad w_{\ell,P} = \frac{w_{\ell,t} + w_{\ell,b}}{2}$$

4.5.2 Porosity Calculations

After calculating the dynamic liquid pressure (P_ℓ) and the superficial liquid velocity ($\boldsymbol{u}_\ell$) distributions, the average pore growth ($\Delta\bar{g}_p$) for any given porosity region can be determined by the numerical integration of equation (4.14) as following:

$$\Delta\bar{g}_p = \frac{1}{\rho_\ell V_p}\sum_{i=1}^{N_P}\left(\Delta\bar{\rho}_i^{SL}\times\Delta V_i\right)+\frac{\Delta t}{V_p}\sum_{i=1}^{N_{P-L}}\left(\boldsymbol{u}_{\ell,i}\cdot\boldsymbol{n}_i\Delta A_i\right) \tag{4.21}$$

where, V_P is the volume of pore region, N_P is the number of porosity cells inside a porosity region, ΔV_i volume of each cell, Δt is the time-step, and N_{P-L} is the number of porosity cells at the porosity-liquid interface. It should be noted that $\boldsymbol{u}_{\ell,i}$ and $\boldsymbol{n}_i$ are vectors and they should be considered in all directions. Since $\Delta\bar{g}_p$ is defined from (4.21), the corresponding average feeding volume is determined as:

$$\Delta V_{Shrink} = \Delta\bar{g}_p \times V_p \tag{4.22}$$

Finally, ΔV_{Shrink} is distributed uniformly across all active cells as $\Delta g_p = \Delta V_{Shrink} / \Delta V_{Active}$. Then the porosity values are updated as:

$$g_p^{new} = g_p^{old} + \Delta\bar{g}_p \tag{4.23}$$

Within each porosity region, all porosities are known as active porosity except: porosities with $g_s + g_p \geq 1$ or surface porosities with $g_s \geq g_{s,sur}$. If all active cells in a porosity region become empty of liquid (i.e. $g_s + g_p = 1$) or if they become inactive due to coherency limit, the neighboring cells with Π values within a low range of $\left|(\Pi-\Pi_{\min})/(\Pi_{\max}-\Pi_{\min})\right| < \varepsilon_{layer}$ are known as active cells. As it was discussed in the previous chapter, the solid movement only occurs when the local solid-fraction is below a coherency criterion (i.e. $g_s < g_{s,coh}$). By this assumption, if a cell in the computational domain has the solid-fractions above the coherency limit (i.e. $g_s \geq g_{s,coh}$) it cannot be emptied completely. Thus, the maximum pore-fraction, $g_p^{\max}$, for each cell is determined

as following:

$$\begin{cases} g_p^{\max} = 1 & g_s < g_{s,coh} \\ g_p^{\max} = 1 - g_s & g_s \geq g_{s,coh} \end{cases} \qquad (4.24)$$

4.5.3 Zone Detection Algorithm

To identify each porosity region in the domain, a search algorithm is developed that detects the isolated porosity regions in casting. The method uses the "connected-component labeling algorithm" which is mostly used in image-processing and graph theory fields to label the subset of connected regions or pixels in an image [36]. In this method, first the input porosity field is converted to a binary field using the following thresholding function:

$$Binary\ Value = \begin{cases} 0 & g_p = 0 \\ 1 & g_p > 0 \end{cases} \qquad (4.25)$$

Figure 4.3 shows a sample porosity region and corresponding binary field using Eq. (4.25). In the binary image [Figure 4.3(b)], background cells have $Binary\ Value = 0$ and foreground ones have a value of $Binary\ Value = 1$; that the connected regions in the foreground are desired. The details about the algorithm can be found in Ref. [36].

4.5.4 Summary of All Procedures

In the current advanced feeding model, there are several steps that should be performed during a time-step. The steps can be listed as following:

Principles:

1. Input T, g_s and ρ fields
2. Search for regions with $\Pi \le 0$ for nucleating new porosities
3. Porosity regions are identified using Zone Labeling Algorithm
4. Within each porosity region, all porosities are known as **active porosity** except:
   a) Porosities with $g_s + g_p \ge 1$
   b) Surface porosities with $g_s \ge g_{s,sur}$
5. Liquid pressure at all active porosities is forced to $P_\ell = P_P$
6. The Pressure Poisson equation is solved to obtain P_ℓ and $\boldsymbol{u}_\ell$ fields
7. The pore growth rate (dg_p / dt) and ΔV_{Shrink} are calculated for each porosity region
8. At each porosity region, ΔV_{Shrink} is distributed uniformly on all active cells and g_p field is updated

Special Cases:

1. If there is no active cell in a porosity region, among the neighbor cells, the ones with $\Pi^* \le \varepsilon$ are selected as active porosity cells
2. If there is no active cell in the entire domain, among all non-empty cells, the ones within $\Pi^* \le \varepsilon$ will be known as active porosities
3. If a cell becomes empty of liquid (i.e. $g_s + g_p \ge 1$), its permeability is set to $K = 0$
4. During shrink volume distribution, if the entire porosity region becomes empty and some shrink volume left in the system, among the neighbor cells, the ones with $\Pi^* \le \varepsilon$ will participate in the shrink volume distribution

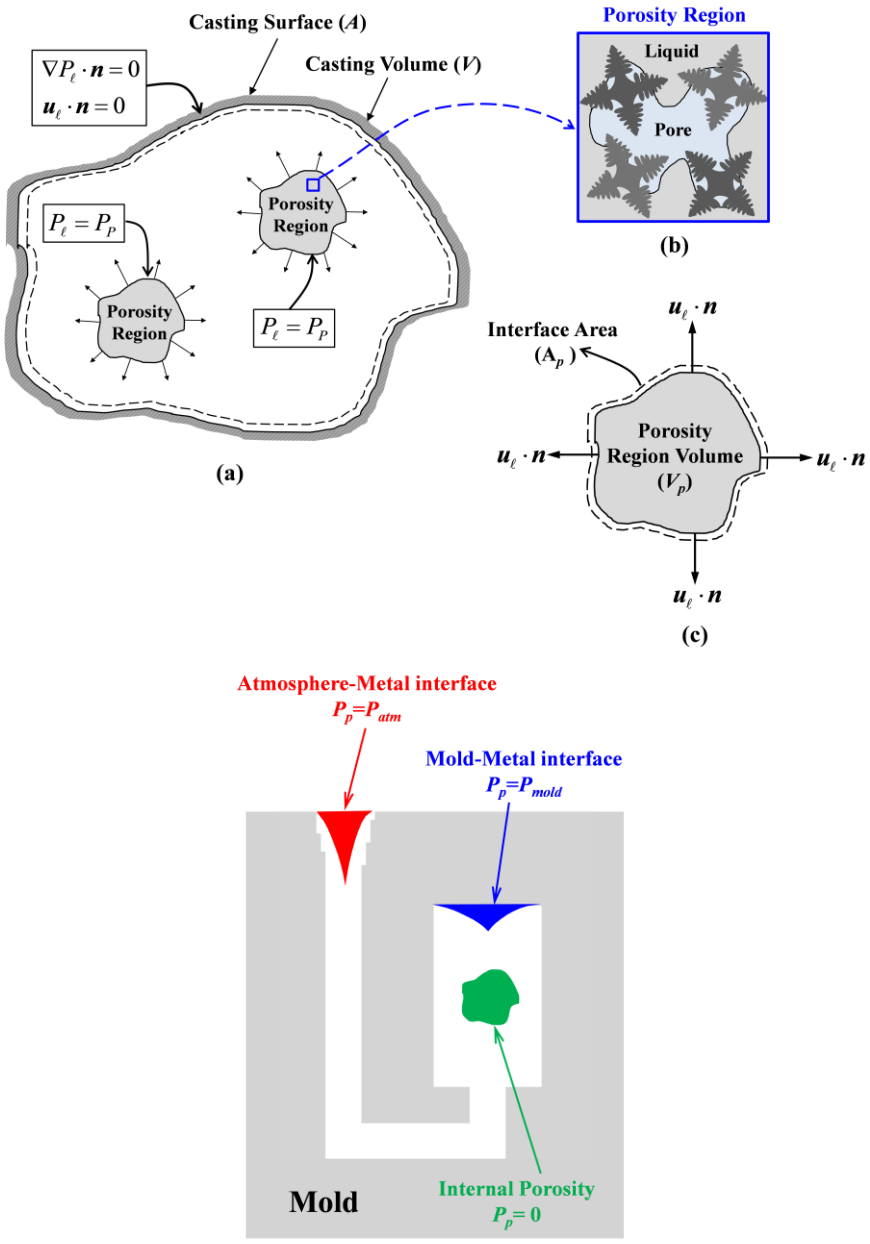

Figure 4.1. (a) Schematic of casting domain including porosity region, (b) a representative volume of a porosity region, (c) close-up view of a porosity region with the mass fluxes at the pore-liquid interface, (d) schematic of pore pressure value at different locations in casting

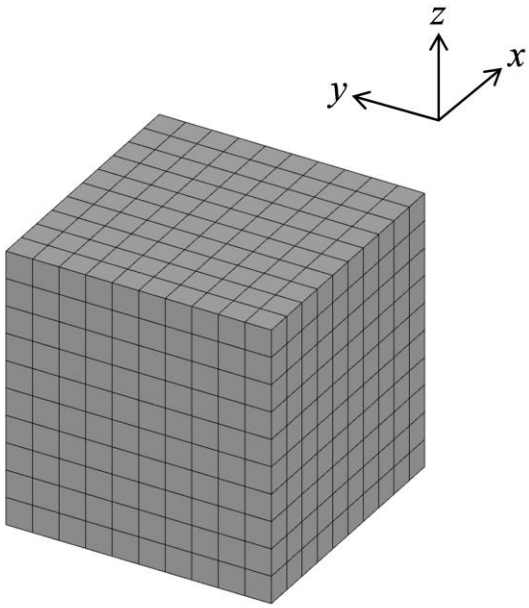

(a)

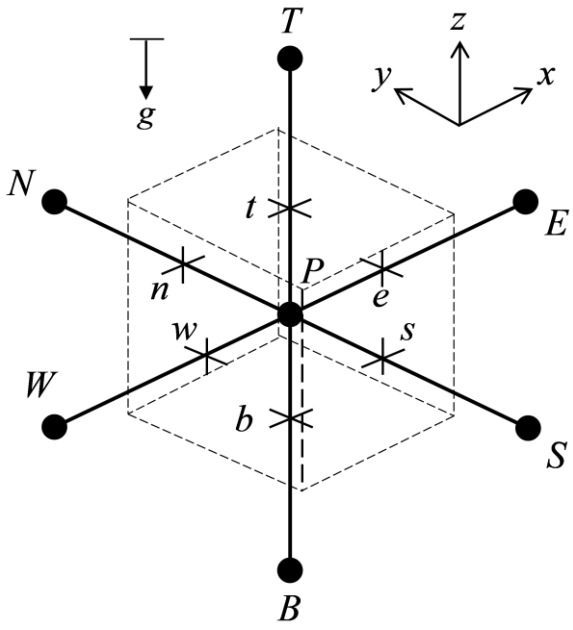

(b)

Figure 4.2. (a) a sample staggered grid, (b) a volume cell with its neighbor cell labels

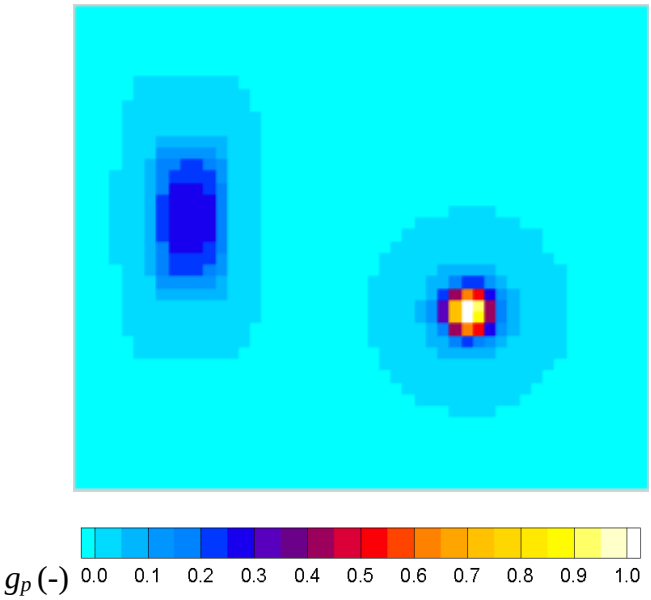

(a)

(b)

Figure 4.3. (a) a sample porosity field used as input to the zone labeling algorithm, (b) generated binary field from a porosity field

CHAPTER 5. APPLICATION OF ADVANCED FEEDING MODEL

In this chapter, the advanced feeding model is applied to several different cases to illustrate the capability of the model in prediction of shrinkage porosity in castings. First, the model is applied to three benchmark examples with simple geometries such as: a block with a single feeding zone, a riser, and a block with two feeding zones. The geometries of all three cases are depicted in Figure 5.1. To simplify the calculations, hypothetical temperature fields are given for the castings' solidification. List of model parameters and material properties used for all three cases are provided in Table 5.1; unless otherwise stated in the text. Once the model is tested for the benchmark examples, it is applied to more complex castings such as: an aluminum wedge, a WCB plate and two industrial Mn-Steel castings. Finally, the prediction results are compared with the available experimental data.

5.1 Benchmark Examples with Simple Geometries

In the first case of benchmark examples, a block with a single feeding zone and the geometry presented in Figure 5.1(a) is considered for porosity formation. The standard WCB steel with material properties in MAGMAsoft is considered for this study. The given transient temperature is calculated by:

$$T = T_{liquid} - (\dot{T} \times t) - G \times \left[(x - x_0)^2 + (y - y_0)^2 + (z - z_0)^2 \right] \qquad (5.1)$$

where a constant temperature gradient of $G = 16000\ ^{o}\mathrm{C/m}$, a constant cooling rate of $\dot{T} = 0.01\ ^{o}\mathrm{C/s}$ are considered for the cooling of the block. The parameter t is time and x_0, y_0 and z_0 are the location of block's center and T_{liquid} is the liquidus temperature. Once the temperature field is defined by equation (5.1), the solid-fraction and the density fields are calculated from respective temperature-dependent curves in MAGMAsoft. The material properties and model parameters are presented in Table 5.1. Simulation results in Figure 5.2 show that at the beginning of the simulation (i.e. $\mathrm{Time} = 1\mathrm{s}$), a porosity region

nucleates at the center of the block where the solid-fraction is the lowest [Figure 5.2(a)]. Due to a small pressure drop within the mushy zone, the existing porosity could feed the entire casting without noticeable pressure drop. So, the total liquid pressure distribution is pretty much hydrostatic everywhere in the block [Figure 5.2(b)]. Results at $\text{Time} = 45\text{s}$ show that, higher solid-fractions around the corners [Figure 5.2(c)] causes the liquid pressure to drop significantly as the flow moves away from the porosity area [Figure 5.2(d)]. Also, it can be observed that the porosity region has grown from $\text{Time} = 1\text{s}$ to $\text{Time} = 45\text{s}$ [Figure 5.2(e)]. Finally, at $\text{Time} = 90\text{s}$, the block is mostly solidified [Figure 5.2(f)] and there is almost no feeding flow in the domain. As the dynamic pressure inside the porosity region is uniform, the total pressure becomes hydrostatic inside the porosity region while in the solid areas the pressure is set to a low value [Figure 5.2(g)]. At the end of solidification, the maximum porosity value is observed at the center of the block [Figure 5.2(h)].

To investigate the effect of model parameters on the final porosity results, a parametric study has been performed which its results are shown in Figure 5.3. In Figure 5.3(a), a small $\varepsilon_{layer} = 0.001$ is used in the simulation which shows that the porosity becomes more concentrated at the middle of the block. In another study a higher value of $\varepsilon_{layer} = 0.1$ is used and it causes the shrinkage porosity distributed in layers and smoothly around the open hole [Figure 5.3(b)]. For the third example, a small value of $\varepsilon_{nuc} = 0.001$ is used which results the internal porosity to nucleate in small area at the center of the block [Figure 5.3(c)] while a larger value of $\varepsilon_{nuc} = 0.1$ results to more spread porosity in the central parts [Figure 5.3(d)]. Also, the effect of critical solid fractions, $g_{s,sur}$ and $g_{s,\text{coh}}$ are investigated. The results show that lower value of $g_{s,sur} = g_{s,\text{coh}} = 0.25$ will result to smaller open hole at the block's center [Figure 5.3(e)] while a larger value of $g_{s,sur} = g_{s,\text{coh}} = 0.75$ allows a larger open hole in the block [Figure 5.3(f)]. The reason is that by using larger value of $g_{s,sur}$ and $g_{s,\text{coh}}$, the pores have more time to grow and form as open hole in casting. In addition, the grid and time-step independency of the model are

performed. Figure 5.4 and Figure 5.5 show that the results are independent of grid size and numerical time-step.

In the second example, a riser with a surface sink and an internal porosity with the geometry presented in Figure 5.1(b) is considered. Like the block, the temperature distribution is given as input with the following equation:

$$T = T_{liquid} - (\dot{T} \times t) - G_1 \times \left[(x - x_0)^4 + (y - y_0)^4 \right] - \left[G_2 \times (z - z_0)^4 \right] \qquad (5.2)$$

where $G_1 = 5 \times 10^7 \ ^{o}\mathrm{C/m}$, $G_2 = 10^5 \ ^{o}\mathrm{C/m}$ and $\dot{T} = 0.007 \ ^{o}\mathrm{C/s}$. Once the transient temperature is defined from equation (5.2), the solid-fraction distributions is calculated from temperature-dependent curves. To observe a large shrinkage pipe in the casting, a larger solid density of ρ_{solid} = 7798 kg/m^3 is considered for the shrinkage calculations. Other model parameters and material properties are listed in Table 5.1 Simulation results in Figure 5.6 show that at the beginning of solidification, a surface sink forms on the top surface and it feeds the entire shrinkage in the casting until around $\mathrm{Time} = 160\,\mathrm{s}$. During this period, the total pressure distribution is almost hydrostatic, and the flow direction is always away from the surface sink [Figure 5.6(b) and (e)]. After around $\mathrm{Time} = 160\,\mathrm{s}$, the surface becomes coherent and the surface stops growing. Subsequently, an internal porosity nucleates adjacent to the surface sink and keeps growing until the end of solidification. During the second stage, due to a lower dynamic liquid pressure at the porosity region, the magnitude of the total pressure is lower compare to the first stage. It is also observed that, as the flow moves toward the sides which have high solid-fractions, the liquid pressure drops significantly due to the flow resistance in those areas [Figure 5.6(h)]. In the final porosity result in Figure 5.6(k), a large shrinkage pipe followed by an internal porosity area are observed in the casting.

In the third example, geometry in Figure 5.1(c) is selected. The input temperature field is chosen in a way that it creates two feeding zones in the casting. Based on the results presented in Figure 5.7, first, two porosity regions nucleate at the locations with

low solid-fraction values in the casting [Figure 5.7(c)]. These two porosity areas feed the entire shrink in the casting and keep growing until the end of solidification. The flows directions are away from the porosity regions toward the sides and the total pressure drops as the feeding flow moves in areas with high solid- fractions [Figure 5.7].

5.2 Industrial Castings with more Complex Geometries

In the second group of case studies, more complex geometries are considered for model validation (Figure 5.8). For the first case, an aluminum wedge with the model parameters in Table 5.2 is selected. Using the material properties developed for A356 aluminum alloy in Chapter 3, the cooling of the wedge is modeled in MAGMAsoft. By having the 3D transient temperature field and the material properties, the advanced feeding model is applied for the prediction of shrinkage porosity in the wedge casting. The results in Figure 5.9 show that at the beginning of the simulation, two surface sinks form on the inclined and back surface of the wedge [Figure 5.9(c)]. These two sinks feed the entire shrink in the wedge and keep growing until around $\text{Time} = 70\,\text{s}$, when the surfaces become coherent [Figure 5.9(d)]. During this time, the total liquid pressure distribution is hydrostatic everywhere in the domain. Once all surfaces become coherent (i.e. $g_s \geq g_{s,sur}$), internal porosity nucleates adjacent to the surface sink where the solid-fraction value is the lowest [Figure 5.9(c)]. Due to a small size of the wedge, the total pressure in the liquid area is mostly hydrostatic and it has minor drops near the corners [Figure 5.9(e)]. Finally, the wedge is fully solidified at around $\text{Time} = 240\,\text{s}$. The maximum pore-fraction occurs at the thermal center of the casting, where solidifies last during solidification. Finally, the simulation results are compared with the experimental measurements provided in Chapter 3. As it can be observed in Figure 5.10, the through-thickness porosity distribution results from the advanced feeding model agree well with the measurement results from image-processing.

For the second case, a WCB plate casting with the geometry in Figure 5.8(b) is

selected. Like the wedge casting, by using proper material properties, the casting is modeled in MAGMAsoft. Then, the transient temperature fields, solid-fraction and density curves with other material properties are imported to the advanced feeding model. The model parameters for WCB casting are listed in Table 5.2. The simulation results at the mid-plane of the casting are shown in Figure 5.11. Based on the results, first a surface sink nucleates at the top surface of the riser where the Π has the lowest value. This sink feeds the entire shrink in the system until about $\text{Time} = 170\,\text{s}$. At this point, due to an increase in the flow resistance, the total pressure drops significantly in the plate section. So, an internal porosity nucleates in the plate and keeps growing until the plate is fully solidified [Figure 5.11]. The shrinkage pipe stops growing once the surface becomes coherent and then internal porosity nucleates in the riser and it keeps growing until the end of solidification [Figure 5.11]. By take a closer look at the through-thickness and through-width averaged porosity results in Figure 5.12, the evolution of porosity in the plate starts at $\text{Time} = 170\,\text{s}$ and finishes at $\text{Time} = 220\,\text{s}$. The centerline shrink is distributed at the central part of the plate which has the lower solid-fractions during solidification. To validate the model simulation results, they are compared to experimental data presented in a paper by Carlson and Beckermann [18]. In this paper, the centerline shrink distribution in the several WCB plates has been investigated in detail. The experimental results in Figure 5.13 show that the centerline shrinks are mostly concentrated in the central part of the plate. This trend is accurately predicted by the advanced feeding model presented in Figure 5.13(c).

In another study, two Mn-Steel alloy castings with the geometries presented Figure 5.8(c) and Figure 5.8(d) are considered for simulations. The details of casting dimensions and material properties can be found in Chapter 2. Like other studies, the casting thermal simulations are performed in MAGMAsoft and they are validated by comparing with the experimental measurements. Then, the transient temperature fields and material properties are imported to the advanced feeding model's code to simulate

the evolution of shrinkage porosity in the castings. The simulation results for the Mn-steel Experiment 2 are demonstrated in Figure 5.14 and Figure 5.15. At $\text{Time} = 10\,\text{s}$ [Figure 5.14(a), Figure 5.15(a)], casting is mostly liquid and porosity forms at the poring cup [Figure 5.14(c), Figure 5.15(c)] and it feeds the entire casting. The total pressure distribution is mostly hydrostatic and the flow direction is away from the pouring cup [Figure 5.14(b), Figure 5.15(b)]. This surface sink keeps growing until around $\text{Time} = 150\,\text{s}$ when the location of surface sink becomes coherent. Then another surface sink nucleates at the top of the riser and feeds the shrinkage in the system. This shrinkage pipe develops until around $\text{Time} = 250\,\text{s}$ when the pressure drop in the middle section becomes high enough that an internal porosity nucleates at the center of isolated block in the right side of the casting. From that time both shrinkage pipe and internal porosity in the block feed the entire casting. At around $\text{Time} = 300\,\text{s}$, the liquid pressure drops significantly at the middle section which causes to nucleate porosity at the thin plate section [Figure 5.15(i)]. Finally, the surface sinks and internal porosity stop growing once the casting solidifies. The porosity distributions on the mid-plane cut section are presented in Figure 5.16. The results show that the advanced feeding model has an acceptable in predicting the porosity distributions in castings [Figure 5.16(a)]. By take a closer look at results for the block [Figure 5.16(b)&(c)], it can be observed that the model could predict the formation of macro-porosity in the block. The simulation results for the Mn-steel Experiment 3 are depicted in Figure 5.17 and Figure 5.18. Similar to the Experiment 2, at the beginning of the solidification, the melt is almost liquid [Figure 5.17(a) and Figure 5.18(a)] and the pressure distribution is hydrostatic everywhere [Figure 5.17(b) and Figure 5.18(b)]. In this stage, all the shrink in the casting appear as surface sink in the gating system [Figure 5.17(c) and Figure 5.18(c)]. Once the sinking area becomes coherent at $\text{Time} = 150\,\text{s}$, it stops growing and a new shrinkage pipe is created at the top of the riser and grow until the end of solidification. The riser can feed the entire shrink in the system until around $\text{Time} = 500\,\text{s}$, when the liquid pressure in the

block drops due to flow resistance in the middle [Figure 5.18(h)]. At this time, a porosity nucleates in the block and feeds the remaining shrink [Figure 5.18(i)]. Finally, the block and the middle section freezes off and the riser keep feeding the remaining shrink in the system. The shrinkage porosity stops growing, once the casting is fully solidified.

To investigate the effects of model parameters on the final porosity distributions, several parametric studies have been performed which the results are presented in Figure 5.20 - Figure 5.23. According to results, increasing ε_{layer} from 0.001 to 0.10 affects the shape of shrinkage pipe in the riser while it has a minor effect on the internal porosity distributions in the casting. The results also show that the effect of ε_{nuc} on porosity distribution is not significant. It is also observe that increasing $g_{s,sur}$ and $g_{s,\mathrm{coh}}$ from $g_{s,sur} = g_{s,\mathrm{coh}} = 0.45$ to $g_{s,sur} = g_{s,\mathrm{coh}} = 0.60$ changes the shape and the location of shrinkage pipe in the riser. Also, it affects the internal porosity distributions in the block and thin plate section. Moreover, it has been noticed that lower values of K_0 and $K_{\min}$ facilitates the occurrence of liquid pressure-drop during solidification which causes the porosities become larger in low values compare to large values of K_0 and $K_{\min}$. Finally, the effect of P_σ on the porosity formation is investigated which results demonstrated that increasing P_σ from $0.5P_{atm}$ to $2.0P_{atm}$ has significant effects on the shape and distribution of shrinkage pipe in the riser. Also, it has changed the internal porosity distributions in the middle plate and block sections in casting.

Table 5.1. Properties and parameters used in benchmark examples

Parameter	Value
K_0 (m^2)	1×10^{-8}
K_{min} (m^2)	5×10^{-15}
K_{max} (m^2)	4×10^{-6}
$g_{s,sur}$ (-)	0.50
$g_{s,coh}$ (-)	0.50
ε_{layer} (-)	1×10^{-2}
ε_{nuc} (-)	1×10^{-2}
P_{atm} (bar)	1.01325
$P_{\sigma,0}$ (bar)	P_{atm}
P_{mold} (bar)	P_{atm}
ρ_{solid} (kg/m^3)	7124
ρ_{liquid} (kg/m^3)	6958
μ_ℓ (Pa.s)	5×10^{-3}

Table 5.2. Properties and parameters used in industrial cases

Parameter	Case 4: Aluminum Wedge Casting	Case 5: WCB Plate Casting	Case 6: Mn-Steel Plate Casting
$K_0\,(\mathrm{m}^2)$	1×10^{-9}	1×10^{-8}	1.7×10^{-9}
$K_{\min}\,(\mathrm{m}^2)$	1×10^{-15}	5×10^{-15}	1×10^{-16}
$K_{\max}\,(\mathrm{m}^2)$	4×10^{-6}	4×10^{-6}	1×10^{-6}
$g_{s,sur}$ (-)	0.38	0.50	0.55
$g_{s,\mathrm{coh}}$ (-)	0.38	0.50	0.55
ε_{layer} (-)	5×10^{-2}	1×10^{-2}	3.5×10^{-2}
ε_{nuc} (-)	9×10^{-3}	1×10^{-2}	1×10^{-3}
P_{atm} (bar)	1.01325	1.01325	1.01325
$P_{\sigma,0}$ (bar)	P_{atm}	P_{atm}	P_{atm}
P_{mold} (bar)	P_{atm}	P_{atm}	$0.9P_{atm}$
$\rho_{solid}\,(\mathrm{kg/m}^3)$	2573	7198	7124
$\rho_{liquid}\,(\mathrm{kg/m}^3)$	2492	6958	6491
μ_ℓ (Pa.s)	1.58×10^{-3}	5×10^{-3}	5.63×10^{-3}

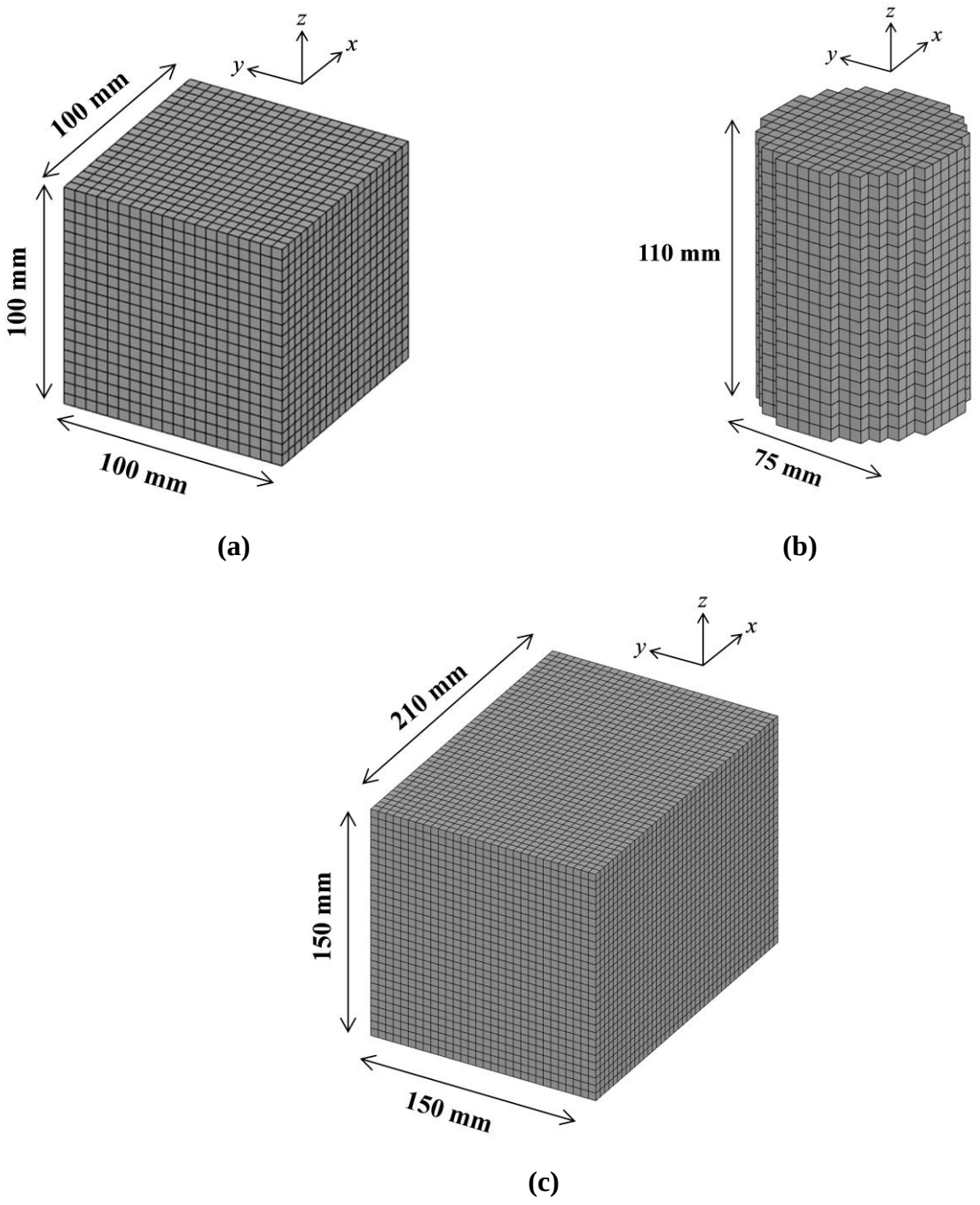

Figure 5.1. Geometry of different case studies: (a) a block with single feeding zone, (b) a riser with surface sink and internal porosity, (c) block with two feeding zones

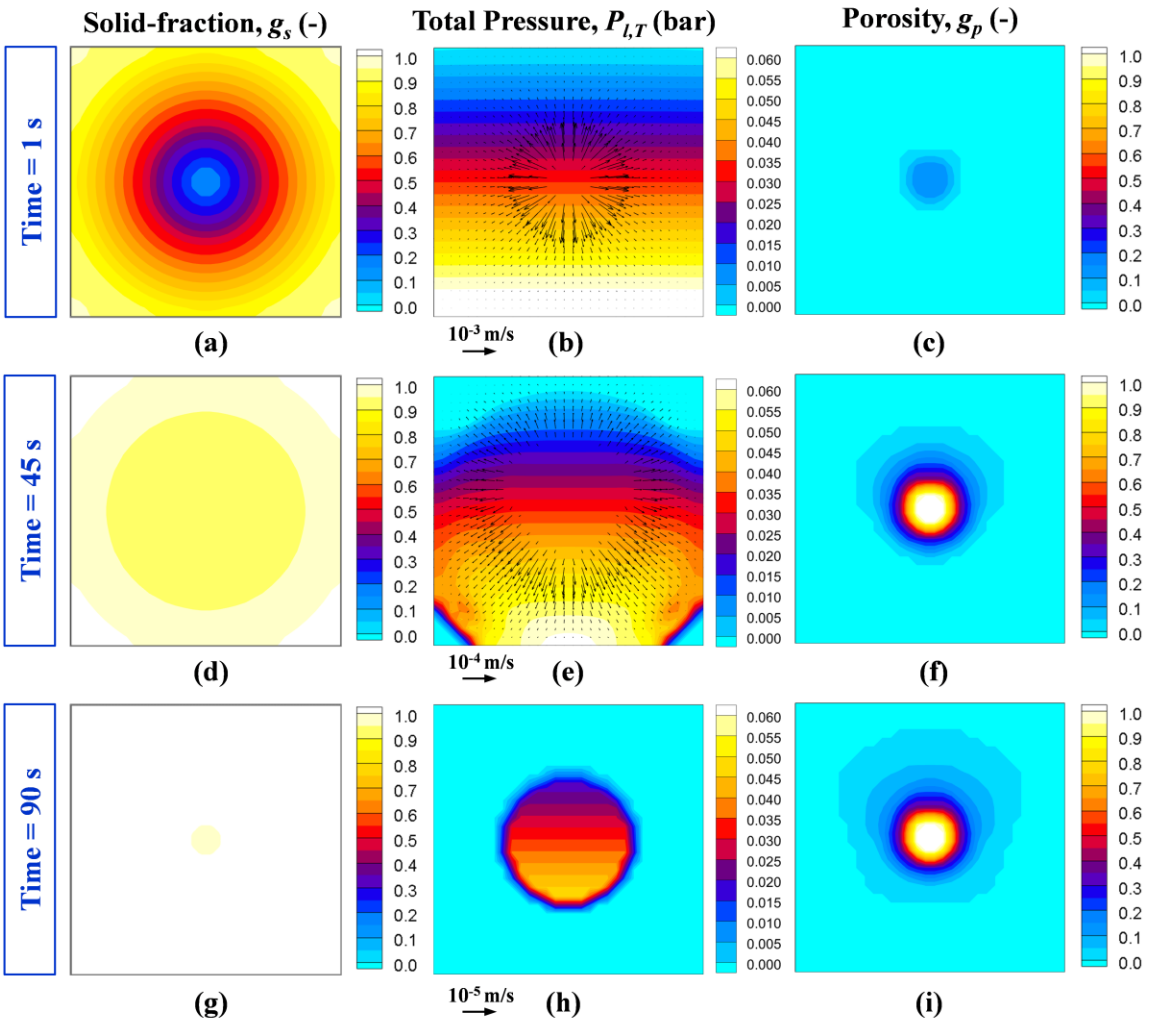

Figure 5.2. Mid-plane results for the 3D Block: solid-fraction (first row), mid-plane pressure distribution and velocity vectors (second column) and mid-plane porosity distribution (third column), (a)-(c) $\text{Time} = 1\text{s}$, (d)-(f) $\text{Time} = 45\text{s}$, and (g)-(h) $\text{Time} = 90\text{s}$

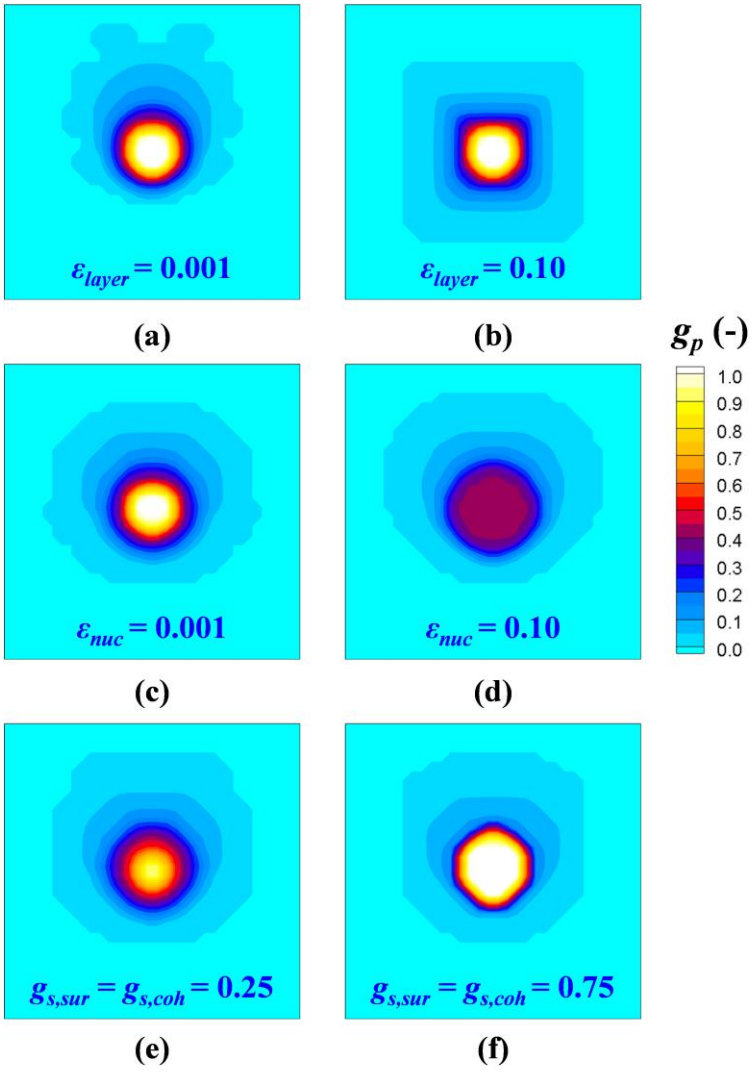

Figure 5.3. Parametric study results for the 3D Block: (a)&(b) effects of ε_{layer}, (c)&(d) effects of ε_{nuc}, (e)&(f) effects of $g_{s,sur}$ and $g_{s,\mathrm{coh}}$

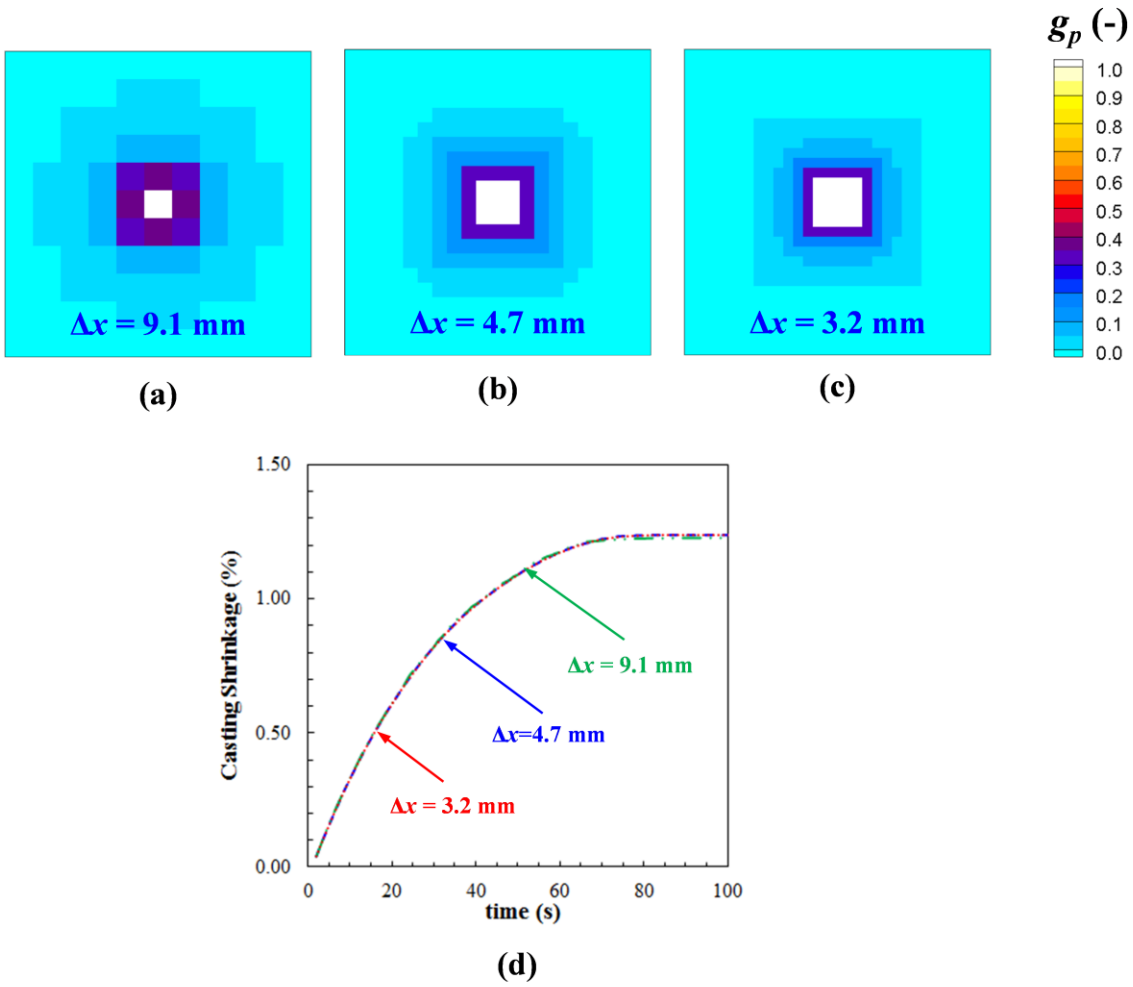

Figure 5.4. Grid study, (a) gird size of $\Delta x = 9.2$ mm, (b) gird size of $\Delta x = 4.7$ mm, (c) gird size of $\Delta x = 3.2$ mm, and (d) comparison of calculated total shrinkage

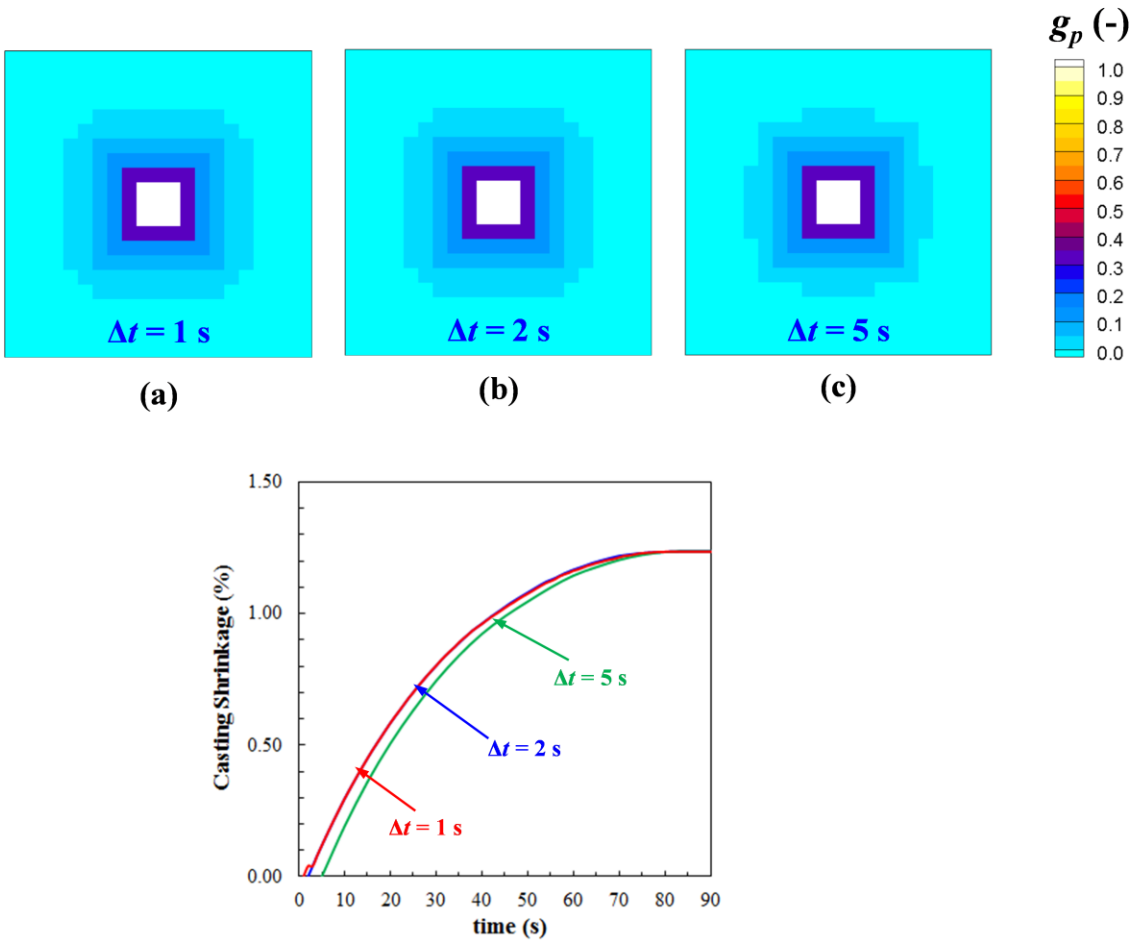

Figure 5.5. Time-step study, (a) $\Delta t = 1$ s, (b) $\Delta t = 2$ s, (c) $\Delta t = 5$ s, and (d) comparison of calculated total shrinkage

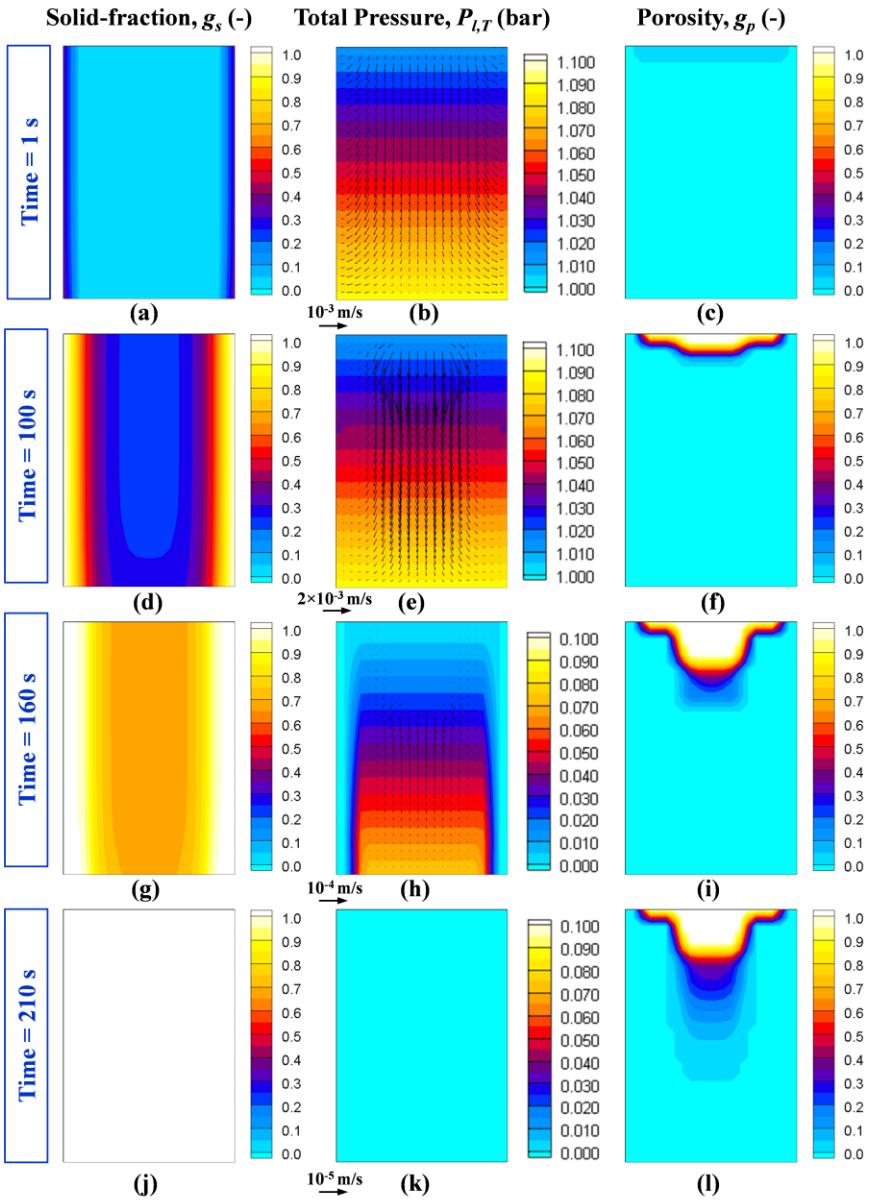

Figure 5.6. Mid-plane results for the riser: solid-fraction (first row), mid-plane pressure distribution and velocity vectors (second column) and mid-plane porosity distribution (third column), (a)-(c) Time = 1s , (d)-(f) Time = 100 s , (g)-(h) Time = 160 s and (j)-(l) Time = 210 s

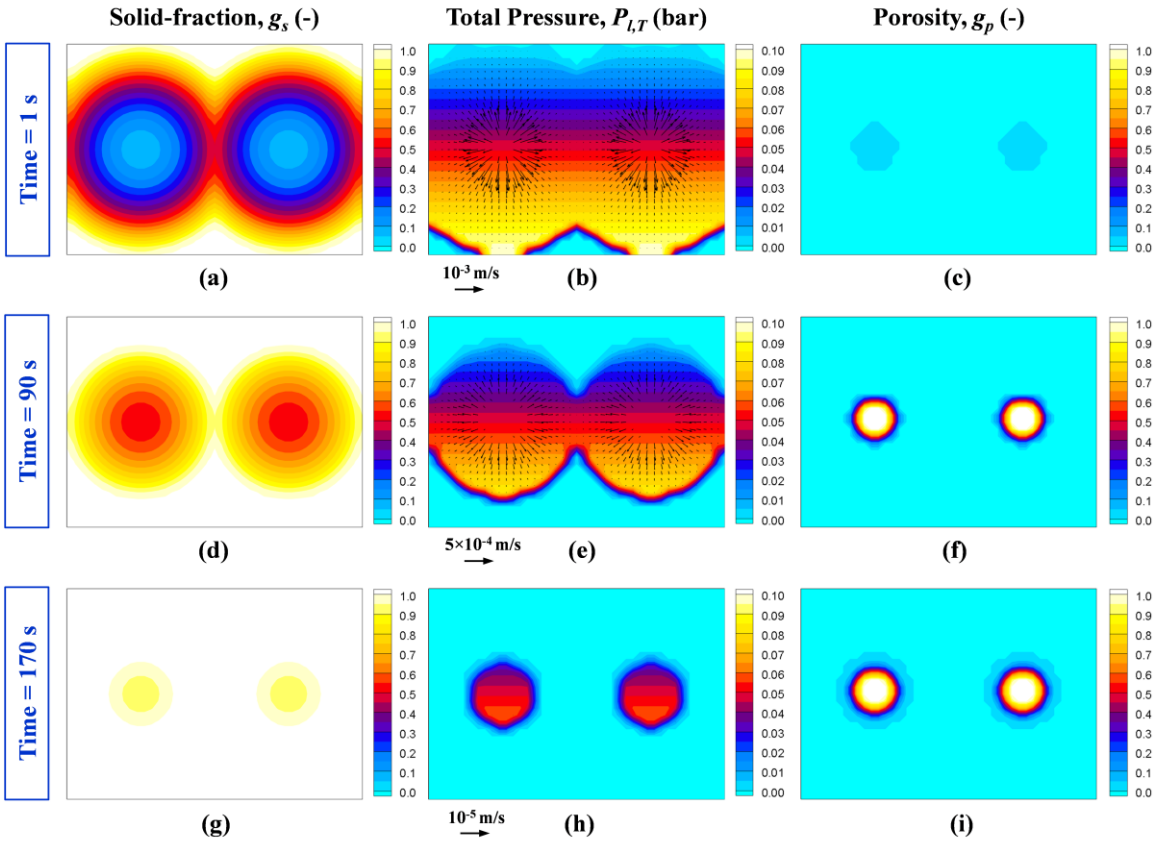

Figure 5.7. Mid-plane results for the block with two feeding zones: solid-fraction (first row), mid-plane pressure distribution and velocity vectors (second column) and mid-plane porosity distribution (third column), (a)-(c) $\text{Time} = 1\text{s}$, (d)-(f) $\text{Time} = 90\text{s}$, (g)-(h) $\text{Time} = 170\text{s}$

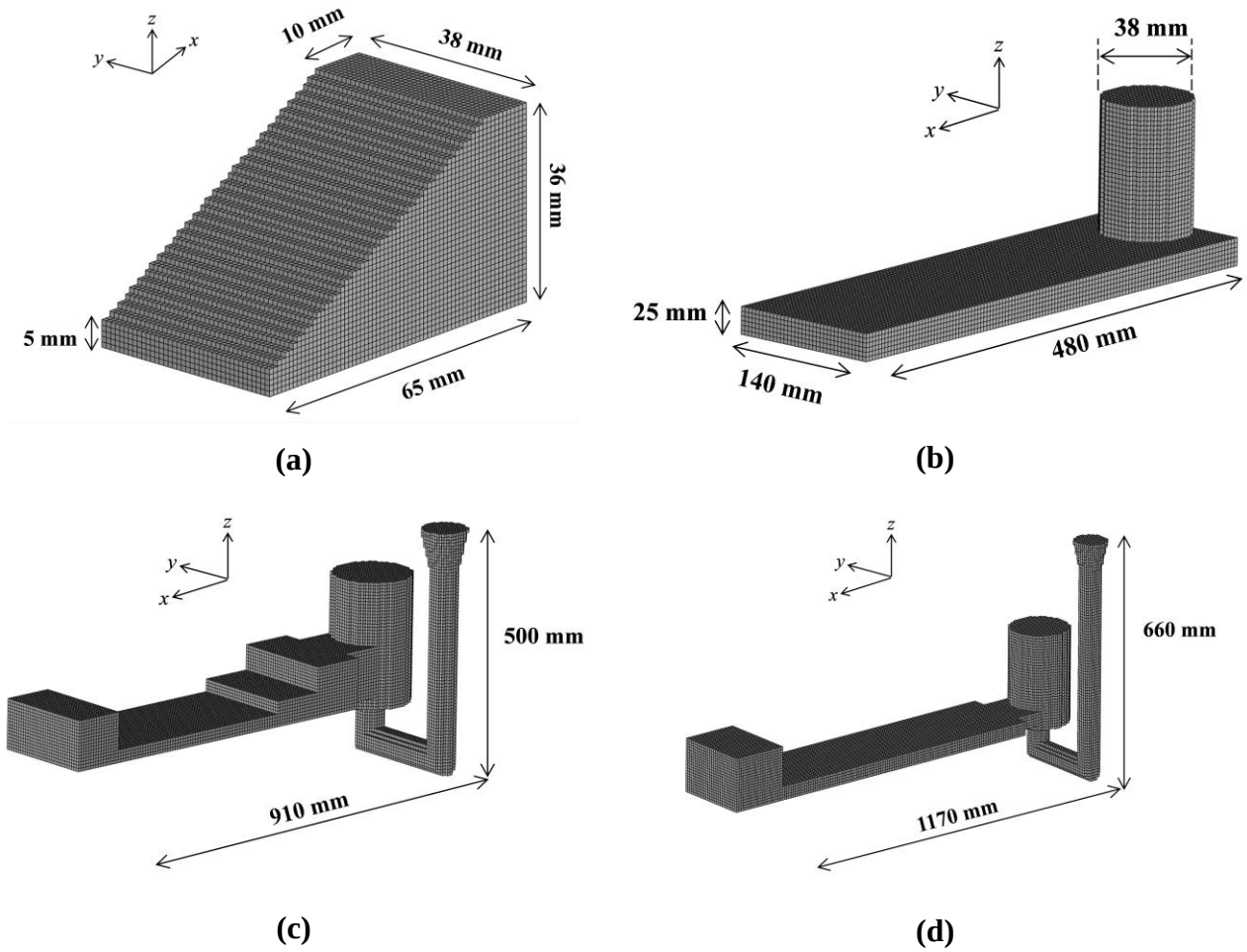

Figure 5.8. Geometry of real castings: (a) Aluminum Wedge, (b) WCB plate, (c) MnSteel Plate Experiment 1, (d) MnSteel Plate Experiment 2

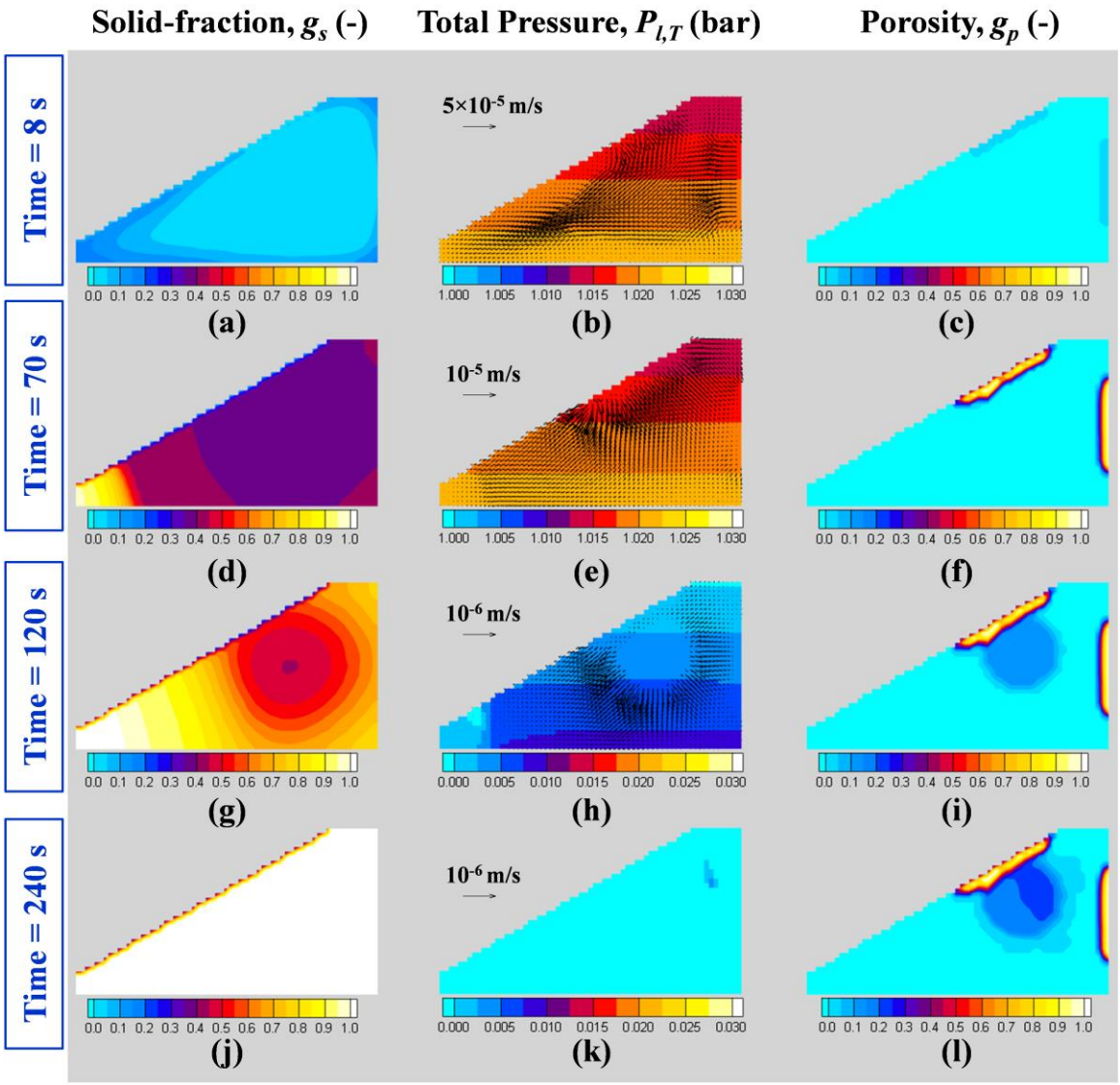

Figure 5.9. Mid-plane results for the A356 aluminum wedge: solid-fraction (first row), mid-plane pressure distribution and velocity vectors (second column) and mid-plane porosity distribution (third column), (a)-(c) $\text{Time} = 1\text{s}$, (d)-(f) $\text{Time} = 70\text{s}$, (g)-(h) $\text{Time} = 120\text{s}$ and (j)-(l) $\text{Time} = 240\text{s}$

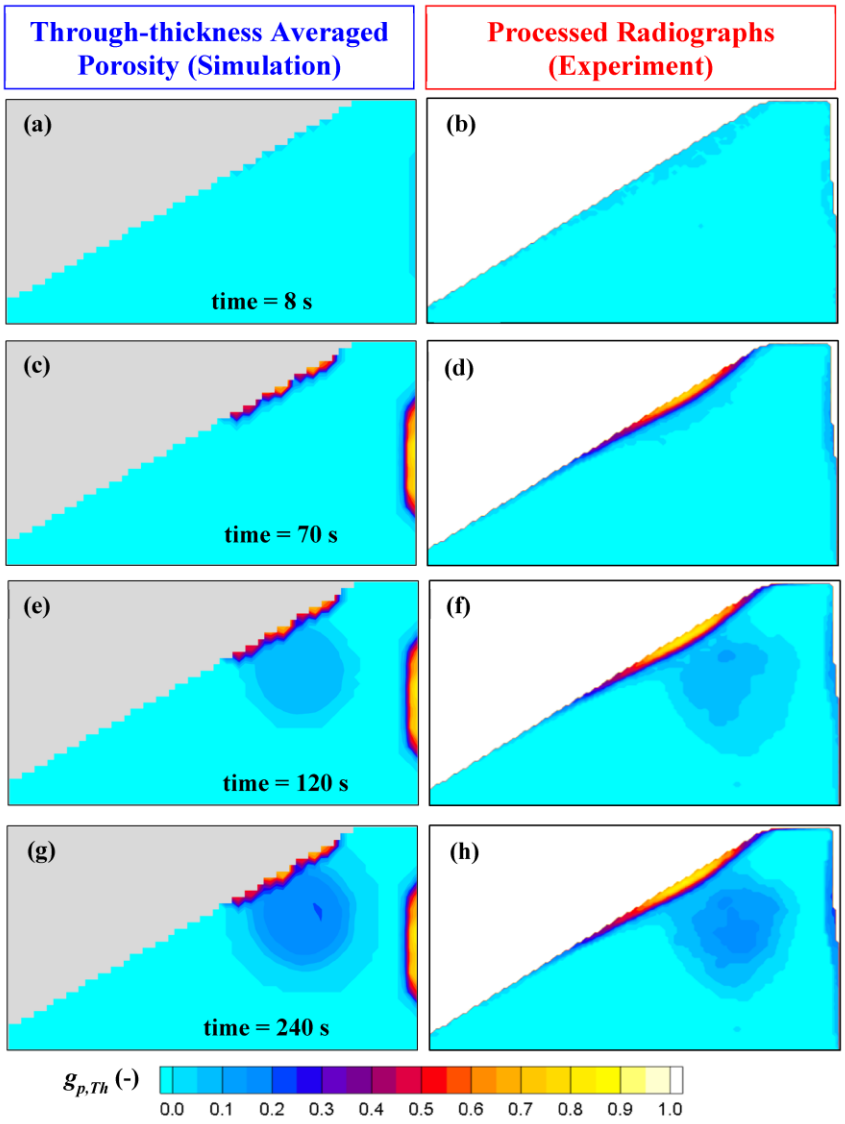

Figure 5.10. Comparison of simulation and experimental results for the wedge casting: simulation results (first column), experimental results (second column), (a)-(c) Time = 8s, (d)-(f) Time = 70s, (g)-(h) Time = 120s and (j)-(l) Time = 240s

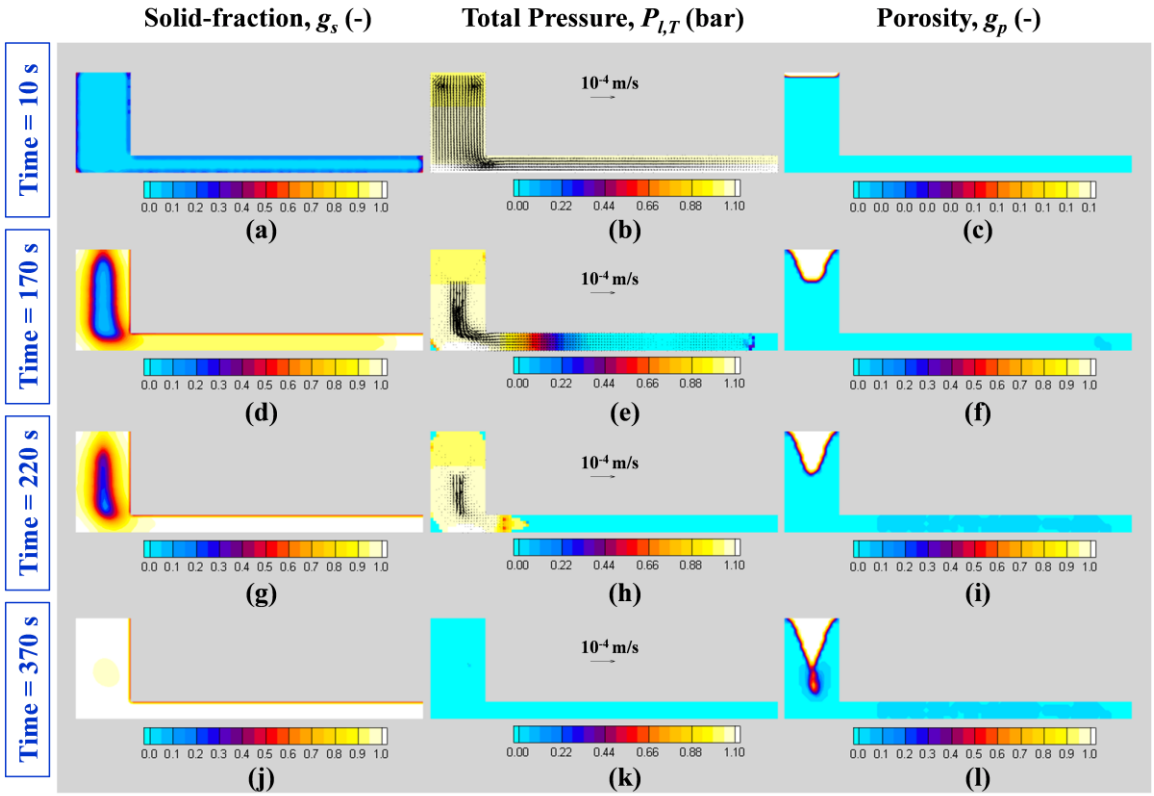

Figure 5.11. Mid-plane results for WCB casting: solid-fraction (first column), mid-plane pressure distribution and velocity vectors (second column) and mid-plane porosity distribution (third column), (a)-(c) $\text{Time} = 10\,\text{s}$, (d)-(f) $\text{Time} = 170\,\text{s}$, (g)-(h) $\text{Time} = 220\,\text{s}$ and (j)-(l) $\text{Time} = 370\,\text{s}$

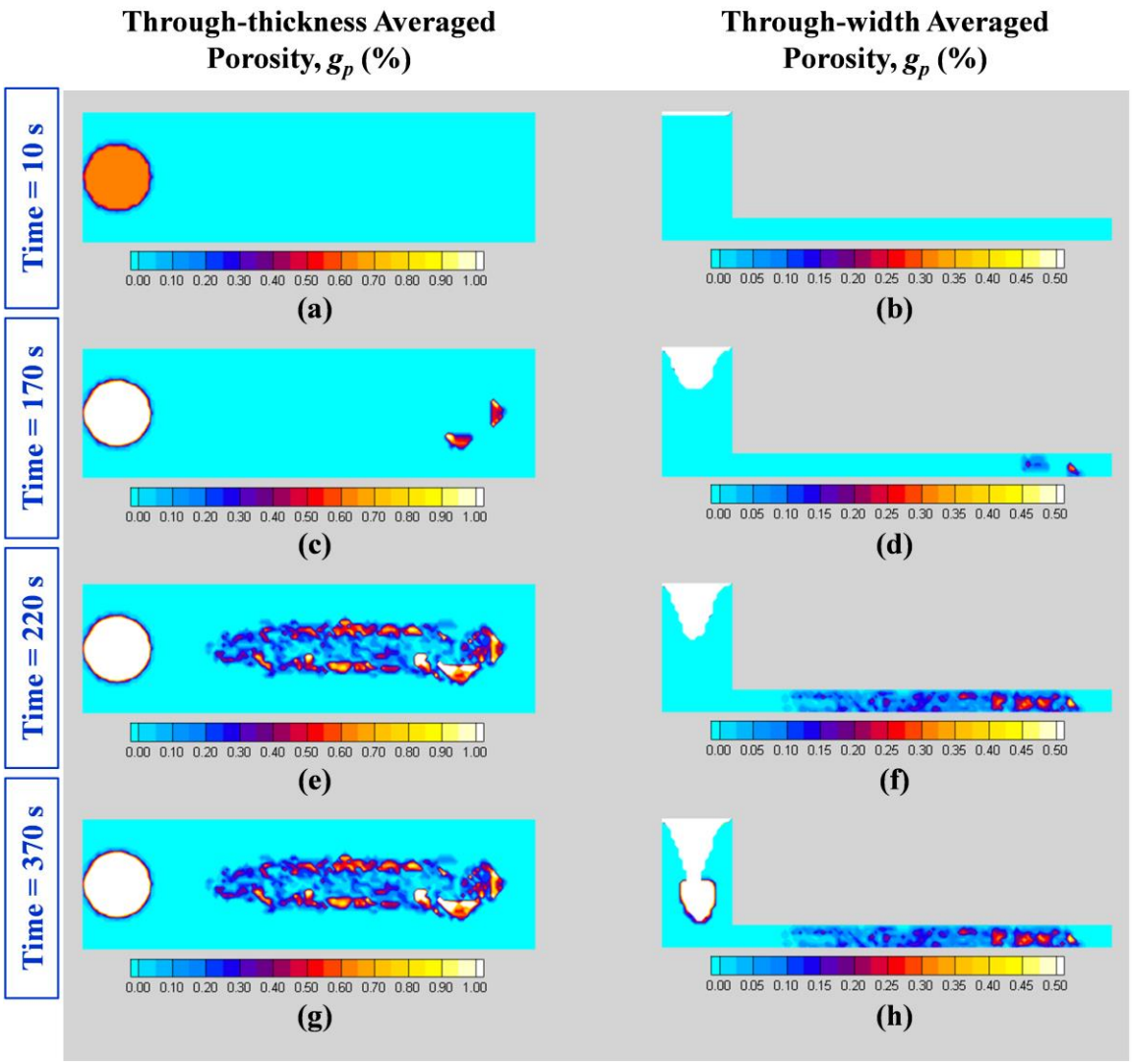

Figure 5.12. Predicted results for WCB casting: through-thickness averaged porosity (first column), through-width averaged porosity (second column), (a)-(b) $\text{Time} = 10\,\text{s}$, (c)-(d) $\text{Time} = 170\,\text{s}$, (e)-(f) $\text{Time} = 220\,\text{s}$ and (g)-(h) $\text{Time} = 370\,\text{s}$

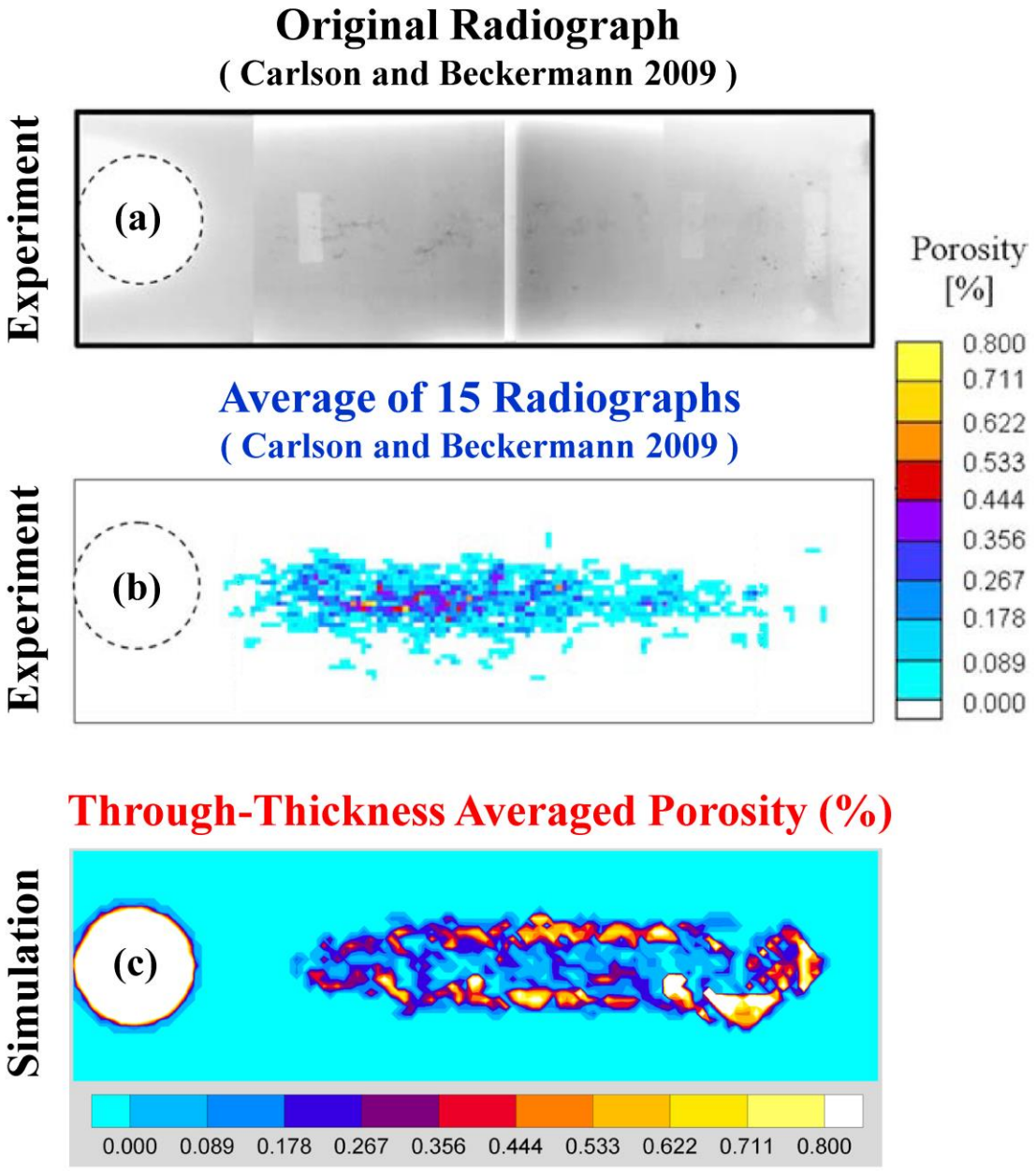

Figure 5.13. (a) the original radiograph of WCB steel casting [18] , (b) average of 15 processed radiographs [18], (c) predicted through-thickness averaged porosity

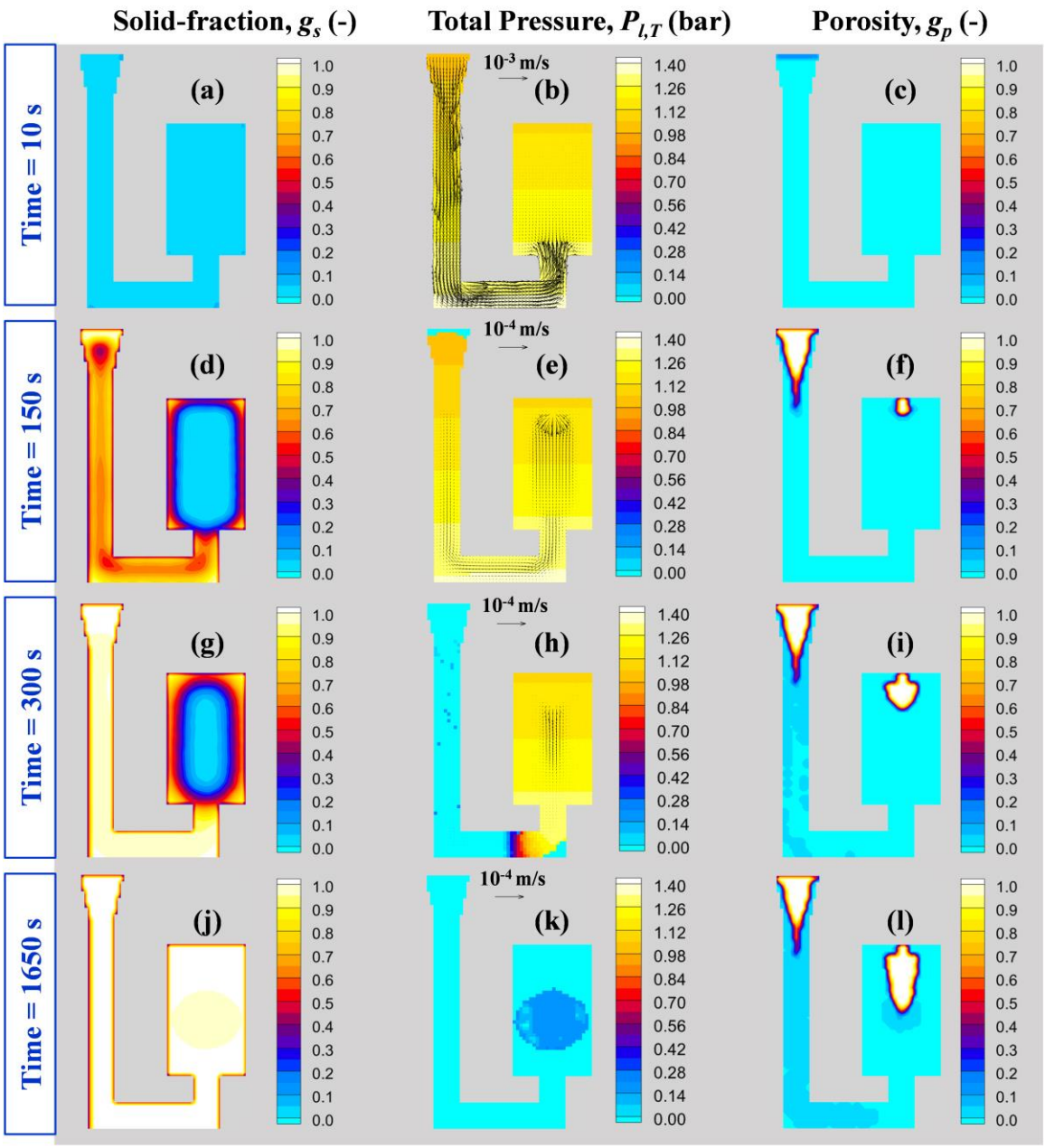

Figure 5.14. Predicted results the Mn-steel casting (Experiment 2): solid-fraction (first column), mid-plane pressure distribution and velocity vectors (second column) and mid-plane porosity distribution (third column), (a)-(c) Time = 10 s , (d)-(f) Time = 150 s , (g)-(h) Time = 300 s and (j)-(l) Time = 1650 s

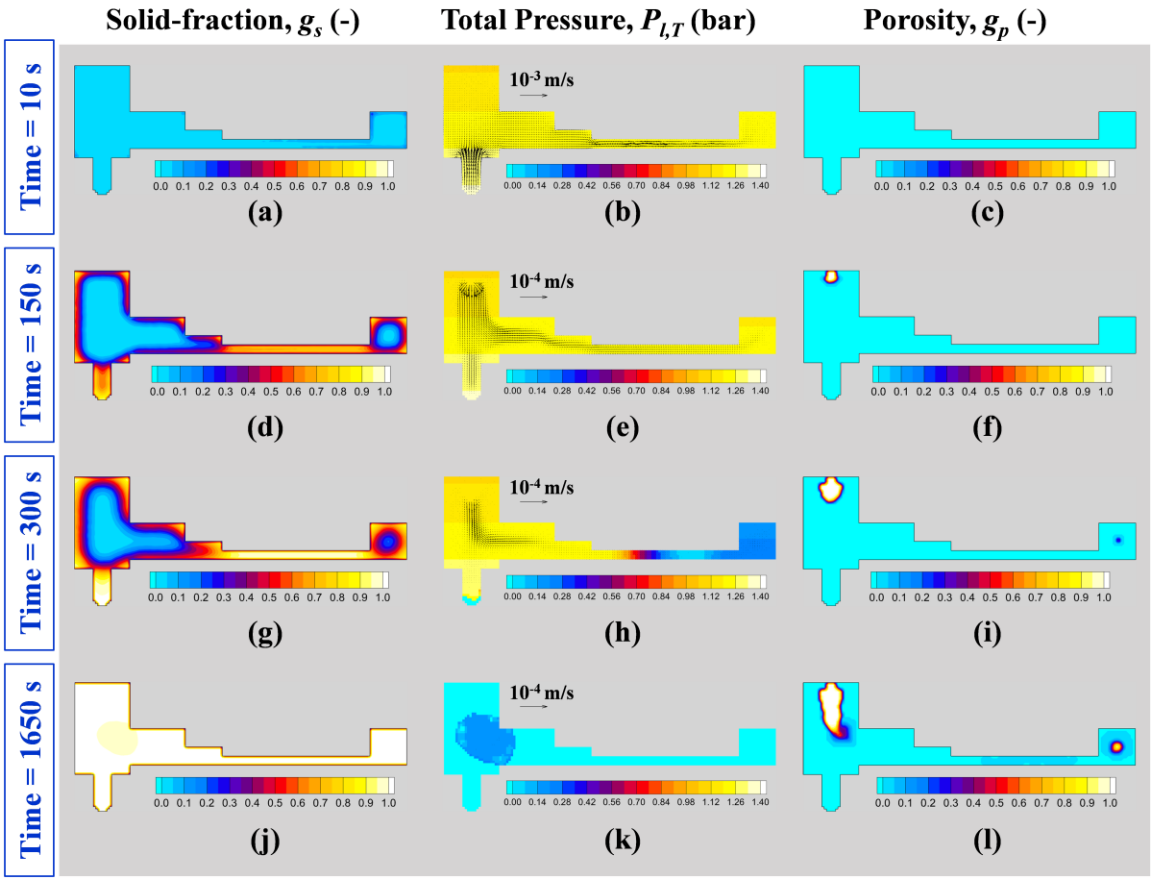

Figure 5.15. Predicted results the Mn-steel casting (Experiment 2): solid-fraction (first column), mid-plane pressure distribution and velocity vectors (second column) and mid-plane porosity distribution (third column), (a)-(c) Time = 10 s, (d)-(f) Time = 150 s, (g)-(h) Time = 300 s and (j)-(l) Time = 1650 s

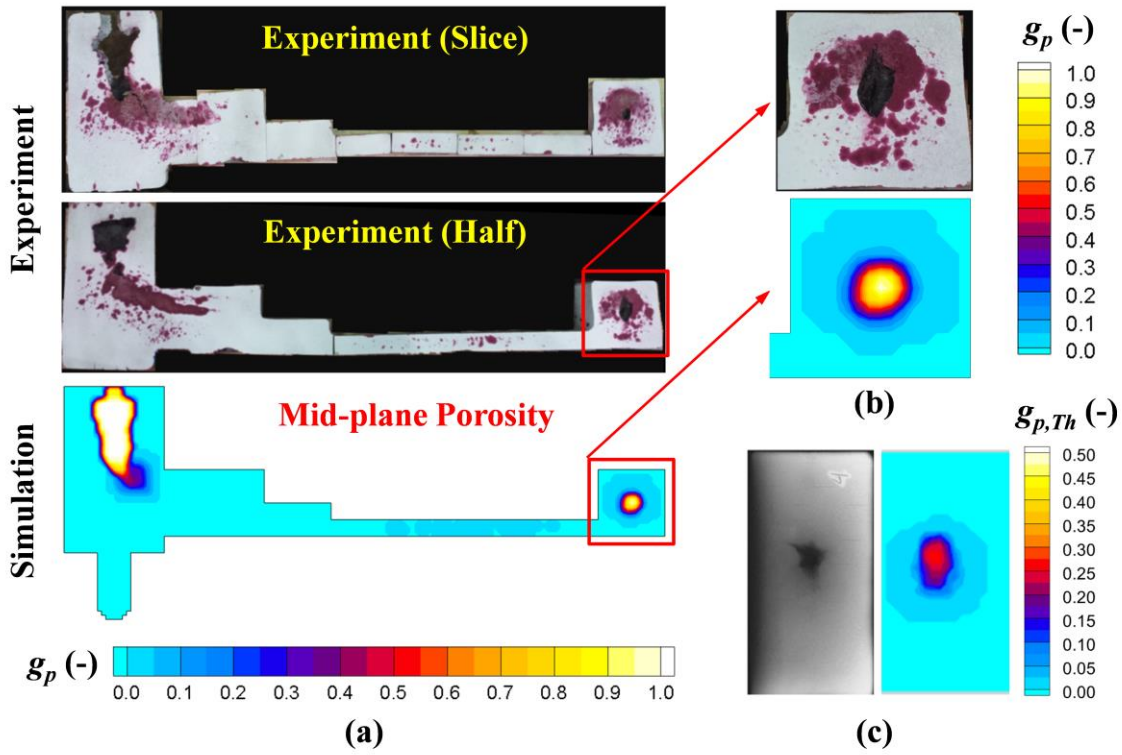

Figure 5.16. Porosity distribution on the mid-plane of Mn-steel casting: (a) Cut-section view of Mn-Steel, (b) Cut-section of the block, (c) X-ray view of the block

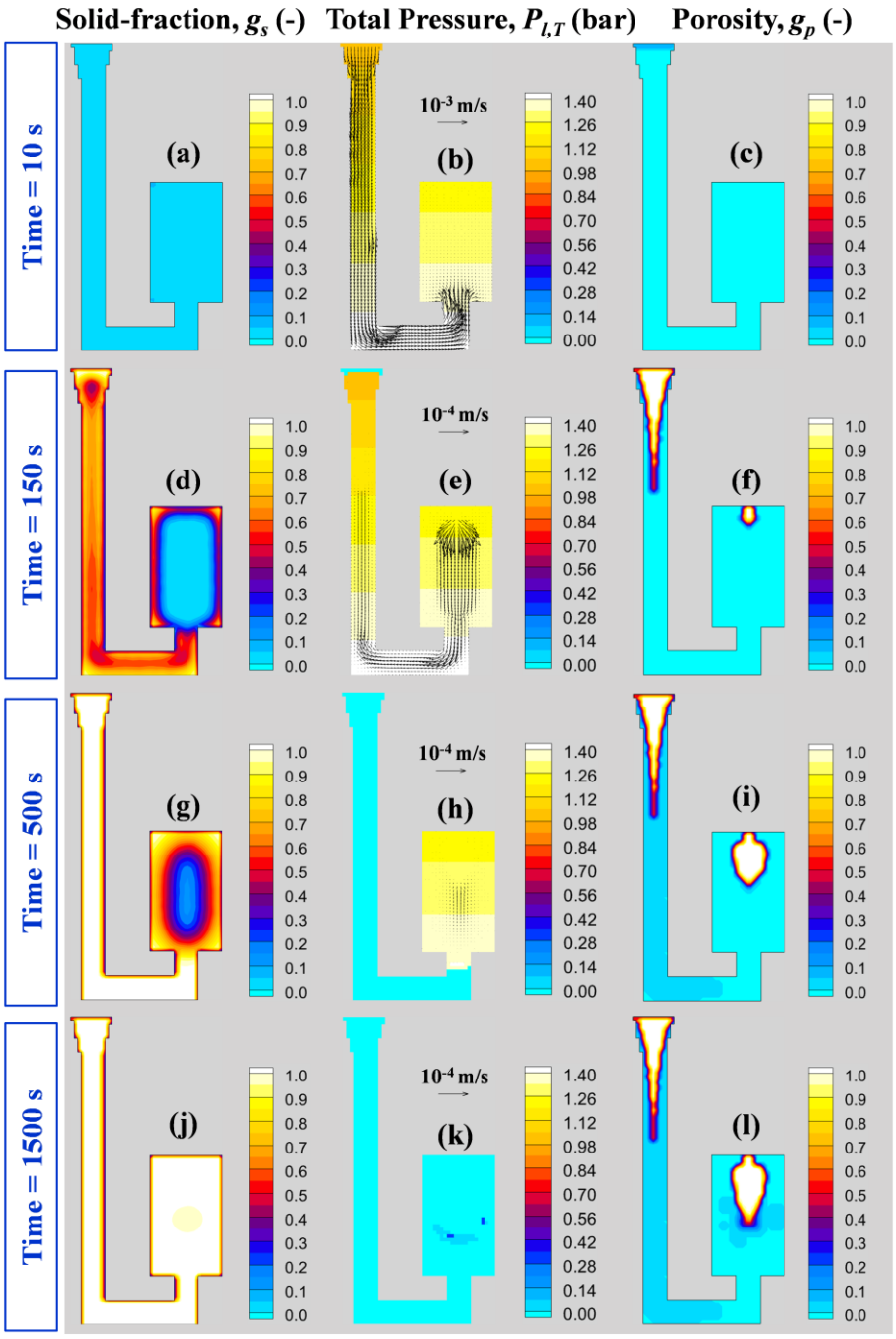

Figure 5.17. Predicted results the Mn-steel casting (Experiment 3): solid-fraction (first column), mid-plane pressure distribution and velocity vectors (second column) and mid-plane porosity distribution (third column), (a)-(c) Time = 10 s , (d)-(f) Time = 150 s , (g)-(h) Time = 500 s and (j)-(l) Time = 1500 s

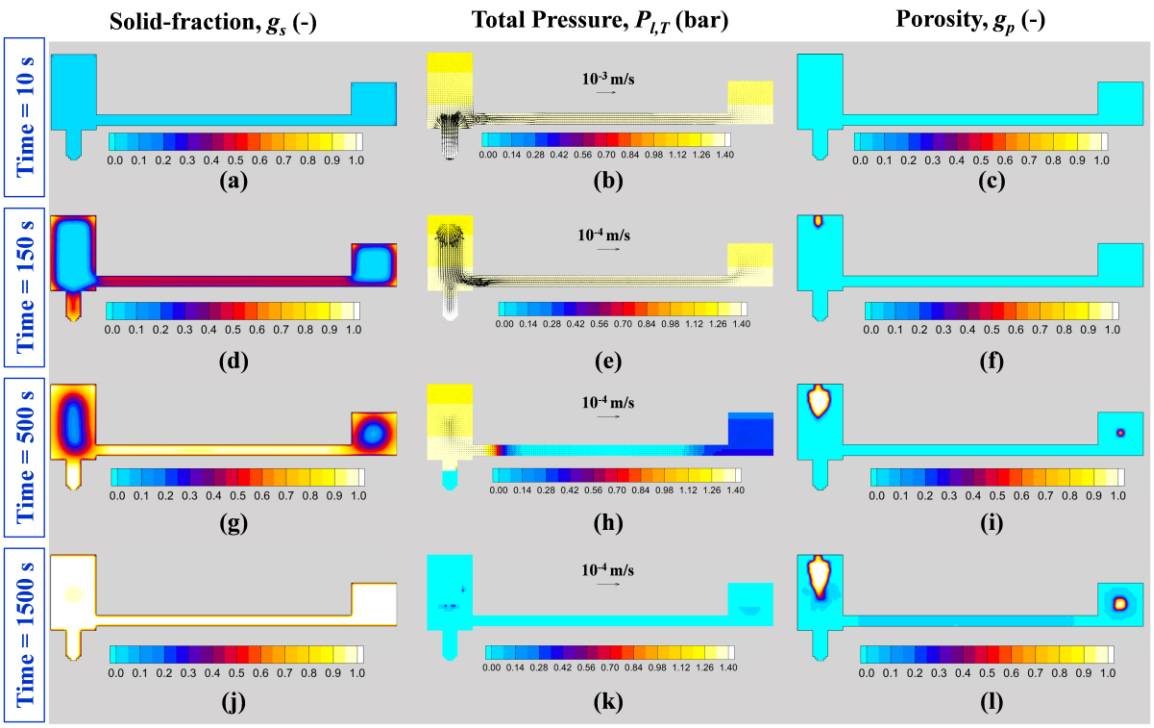

Figure 5.18. Predicted results the Mn-steel casting (Experiment 3): solid-fraction (first column), mid-plane pressure distribution and velocity vectors (second column) and mid-plane porosity distribution (third column), (a)-(c) $\text{Time} = 10\,\text{s}$, (d)-(f) $\text{Time} = 150\,\text{s}$, (g)-(h) $\text{Time} = 500\,\text{s}$ and (j)-(l) $\text{Time} = 1500\,\text{s}$

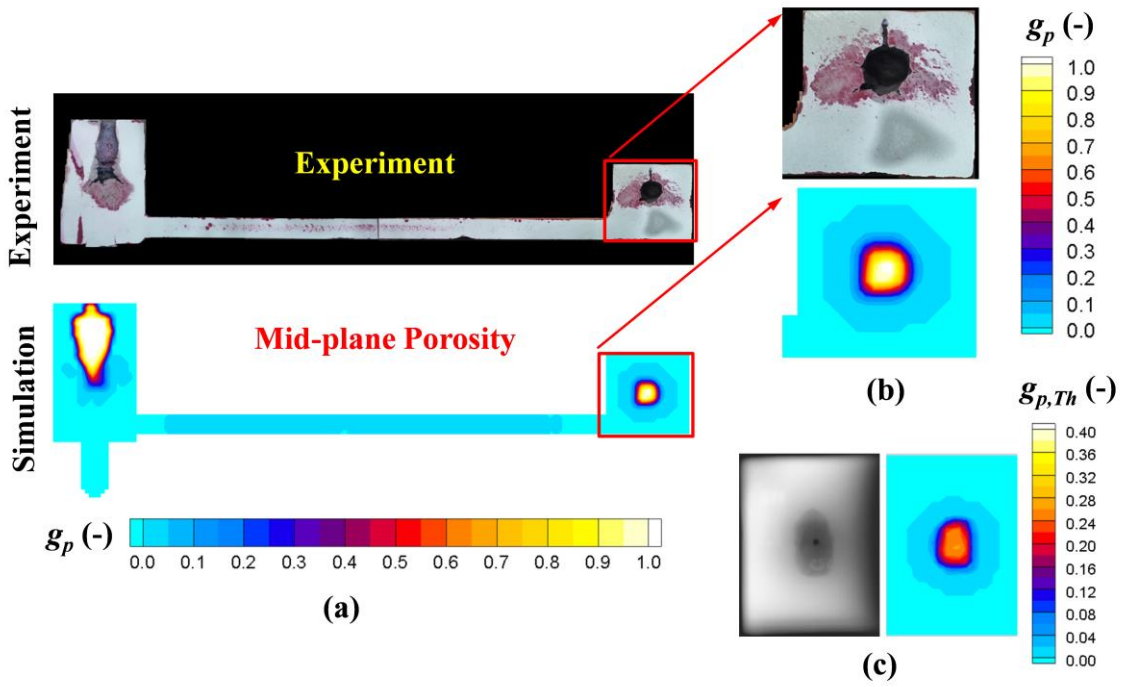

Figure 5.19. Porosity distribution on the mid-plane of Mn-steel casting: (a) Cut-section view of Mn-Steel, (b) Cut-section of the block, (c) X-ray view of the block

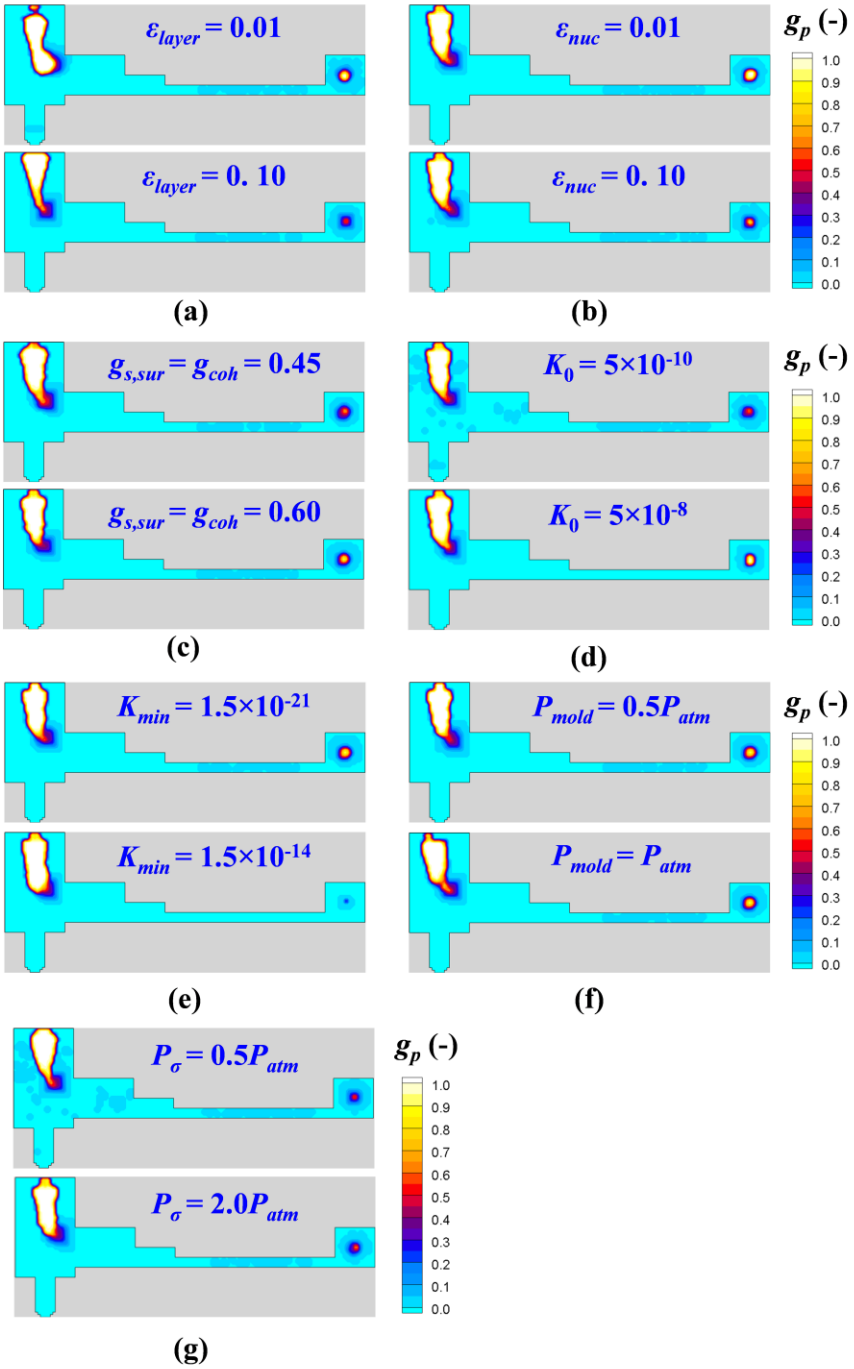

Figure 5.20. Mid-plane results for Experiment 2 parametric study: (a) effect of ε_{layer}, (b) effect of ε_{nuc}, (c) effect of $g_{s,sur}, g_{s,\mathrm{coh}}$, (d) effect of K_0, (e) effect of K_{min}, (f) effect of $P_{\sigma,0}$,

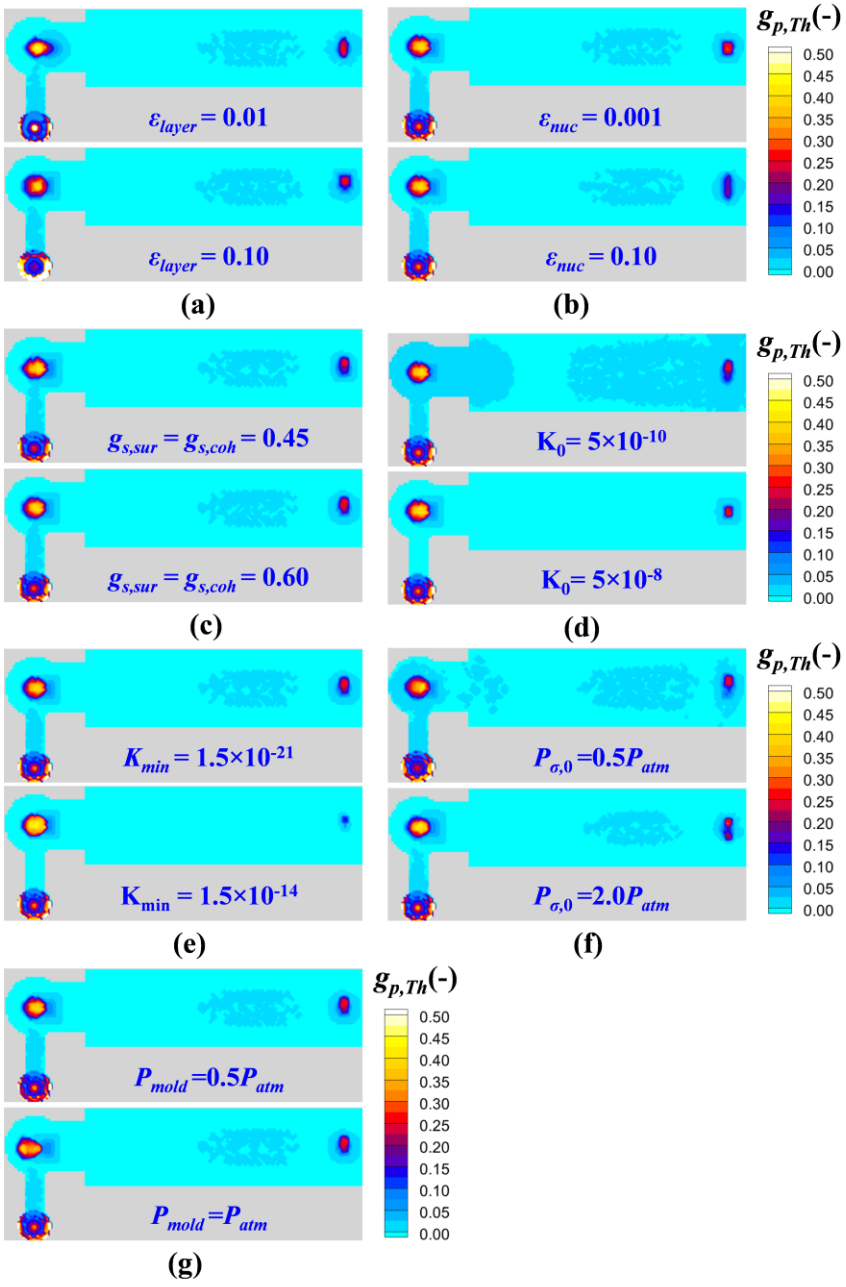

Figure 5.21. X-ray view results for Experiment 2 parametric study: (a) effect of ε_{layer}, (b) effect of ε_{nuc}, (c) effect of $g_{s,sur}, g_{s,\mathrm{coh}}$, (d) effect of K_0, (e) effect of $K_{\min}$, (f) effect of $P_{\sigma,0}$,

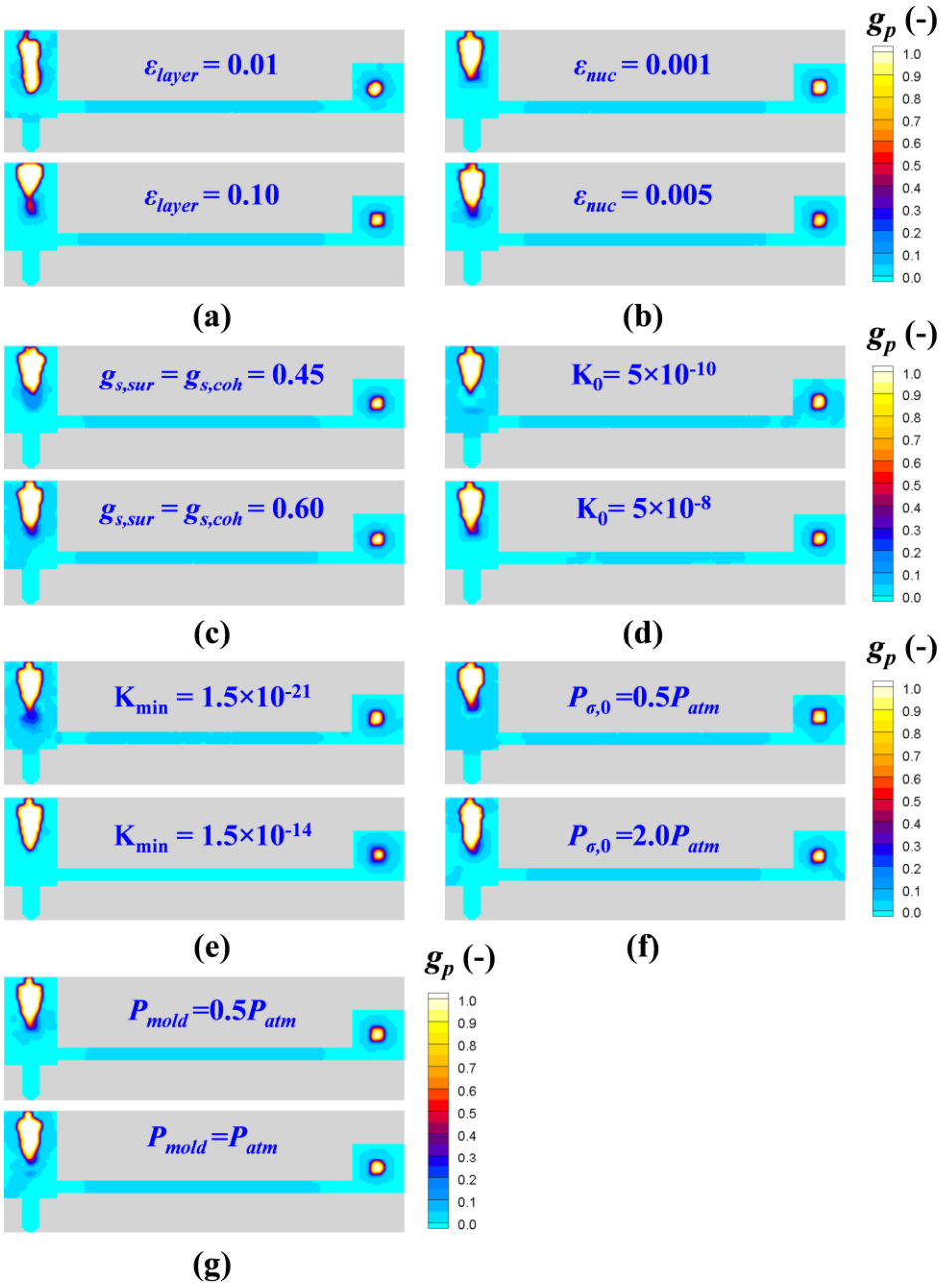

Figure 5.22. Mid-plane results for Experiment 3 parametric study: (a) effect of ε_{layer}, (b) effect of ε_{nuc}, (c) effect of $g_{s,sur}, g_{s,\mathrm{coh}}$, (d) effect of K_0, (e) effect of $K_{\min}$, (f) effect of $P_{\sigma,0}$,

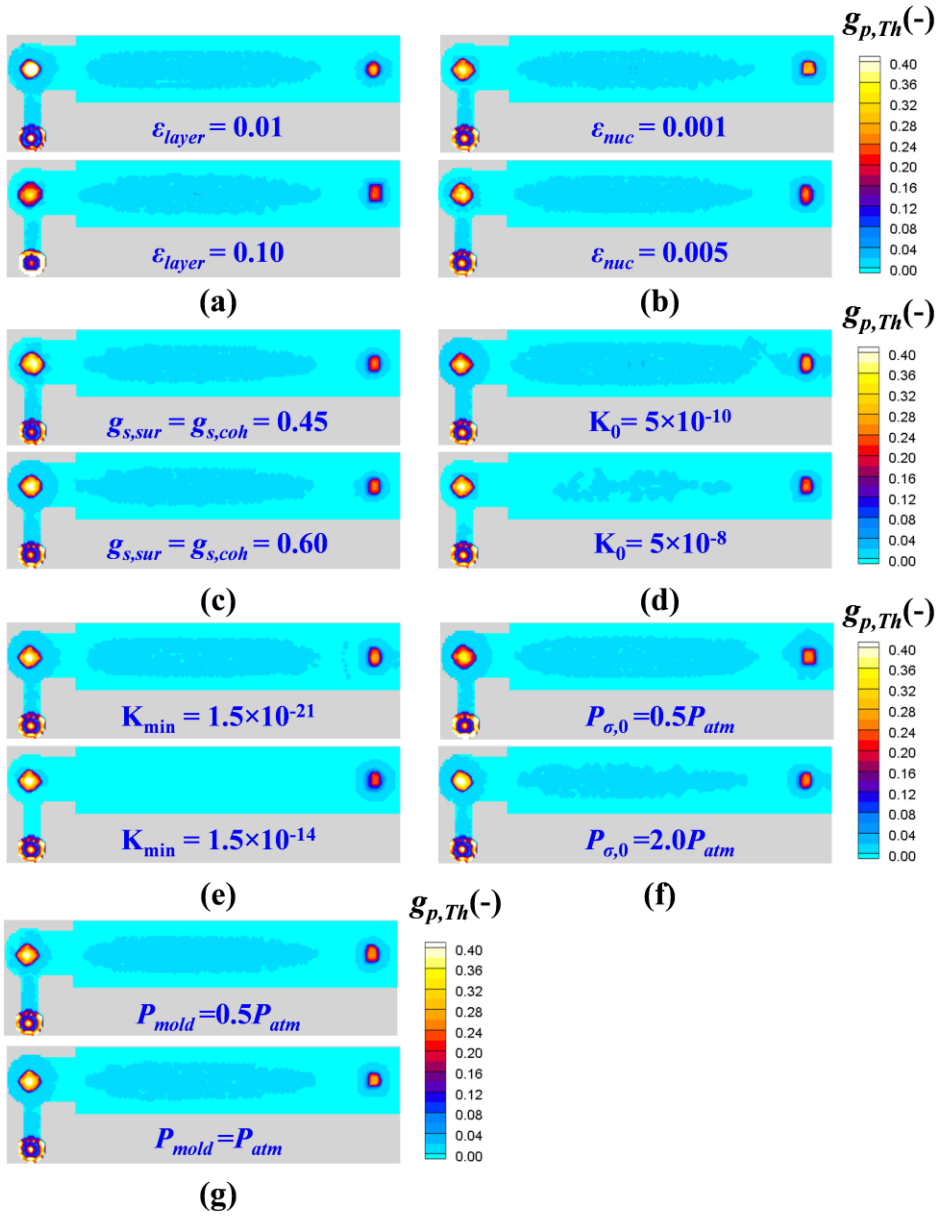

Figure 5.23. X-ray view results for Experiment 2 parametric study: (a) effect of ε_{layer}, (b) effect of ε_{nuc}, (c) effect of $g_{s,sur}, g_{s,\mathrm{coh}}$, (d) effect of K_0, (e) effect of $K_{\min}$, (f) effect of $P_{\sigma,0}$,

CHAPTER 6. CONCLUSIONS AND FUTURE WORK

6.1 Conclusions

Shrinkage-related defects are important quality issues in the metal castings. To avoid and reduce these types of defects, the formation mechanisms of these defects should be understood very well. In this study, physics behind the shrinkage porosity formation during solidification has been studied through numerous experimental tests on A356 aluminum and Mn-steel alloy castings. In the aluminum casting experiment, the evolution of shrinkage porosity in a wedge-shaped casting has been observed in real-time using video radiography. The results indicate that at the early stages of the solidification, when the casting surfaces are not coherent, the shrinkage defects appear in form of surface sinks on the casting exterior. Once, the surfaces become rigid, internal porosity nucleates and develops in areas with low solid-fractions. This trend is confirmed by the results of the Mn-steel experiments. In all mentioned experiments, the cooling of castings was measured by several thermocouples located at different areas in mold walls and castings during solidification. Finally, with the aid of the alloys' thermo-physical properties were developed through the thermal simulations by MAGMAsoft.

By the lessons learned from the experimental studies, an advanced feeding model has been developed for the prediction of shrinkage porosity during solidification of metal alloys. The model combines multi-phase continuity, momentum equations to obtain a Poission-type PDE for the liquid pressure. Then, this equation is solved numerically for obtaining liquid pressure distribution in castings. Once the pressure distribution is defined, the feeding velocity and averaged pore growth rate can be defined from the model equations. A computational FORTRAN code with finite volume approach is developed for solving the governing equations. This model inputs the material properties and transient temperature fields and outputs the porosity distribution in castings. Thus, it can be easily integrated to a regular casting simulation software.

The model has been exercised in detail, in order to explore the effect of model parameters on the predicted porosity for an A356 aluminum, WCB and Manganese steel alloys. The parametric studies reveal how porosity distributions depends on the model parameters such as: the surface coherency limit ($g_{s,sur}$), mass feeding critical solid-fraction ($g_{s,\mathrm{coh}}$), nucleation and distribution parameters ($\varepsilon_{nuc}, \varepsilon_{sur}$), the permeability coefficient (K_0), minimum permeability ($K_{\min}$) and the capillary pressure coefficient ($P_{\sigma,0}$). Finally, it is concluded that the advanced feeding model can accurately predict the location and the amount of shrinkage porosity in casting.

6.2 Future Work

Although the current advanced feeding model has an acceptable accuracy in the prediction of shrinkage porosity in castings, more case studies are needed to make sure the model works very well. So, after the model is implemented in next version of MAGMAsoft software, it should be applied to more industrial cases to see the capabilities of the model in porosity predictions. Also, there are several simplifications in the model that can be improved in the model. Some of the major simplifications are listed as following:

1- It is assumed that the flow movement is only due to the shrinkage in the system and the movement due to the natural convection is neglected. In future model, the effect of natural convection on the pore growth calculations can be considered.

2- In the derivation of pore-growth rate equation, it is assumed that the flow within the pore forming region is negligibly small and the averaged pore growth rate of $d\bar{g}/dt$ is considered for a given porosity region. By this assumption, the dynamic liquid pressure at the porosity region is forced to a specific value and the model equations are only solved outside of the porosity regions. In future, this assumption can be improved by coupling the pore

growth rate to the momentum equation and solving them everywhere in the computational domain including the porosity region.

3- The mushy zone permeability during solidification is assumed to be given by the Kozeny–Carman's equation [equation (4.5)], which needs further investigations.

4- In the model equations, the solid dendrites and porosity movements are neglected, which might not be the case. So, more studies are needed.

5- It is assumed that the melt is free of any dissolved gas and the effect of gas segregation on the pore growth is neglected. In future model, the effect of gas diffusion also can be incorporated in the model.

REFERENCES

1. S.H. Majidi, and C. Beckermann, *Int. J. Cast Met. Res.*, 2017, vol. *30*(5), 301-315.

2. M.T. Rad, P. Kotas, and C. Beckermann, *Metall. Mater. Trans. A*, 2013, vol. *44*, 4266-4281.

3. M.T. Rad, C. Beckermann. In *CFD Modeling and Simulation in Materials Processing 2016*, pp. 85-92. Springer, Cham, 2016.

4. M.J. Couper, A.E. Neeson, and J.R. Griffiths: *Fatigue Fract. Eng. Mater. Struct.*, 1990, vol. 13(3), pp. 213-27.

5. Q.G. Wang, D. Apelian, and D.A. Lados: *J. Light Met.*, 2001, vol. 1 (1), pp. 73–84.

6. R. Hardin, and C. Beckermann: *Metall. Mater. Trans. A*, 2012, vol. 2, pp. 217-224.

7. T.S. Piwonka and M.C. Flemings: *Trans. AIME*, 1966, vol. 236, pp. 1157–65

8. K. Kubo and R.D. Pehlke: *MTB*, 1985, vol. 16, pp. 359-366.

9. A.S. Sabau and S. Viswanathan: *Metall. Mater. Trans. B*, 2002, vol. 33, pp. 243-255.

10. Ch. Pequet, M. Rappaz and M. Gremaud: *Metall. Mater. Trans. A*, 2002, vol. 33, pp. 2095-2106.

11. R.W. Hamilton, D. See, S. Butler, and P.D. Lee: *Mater. Sci. Eng. A*, 2003, vol. 343, pp. 290–300.

12. P.D. Lee and J.D. Hunt: *Modeling of Casting, Welding, and Advanced Solidification Processes VII*, TMS, Warrendale, PA, 1995, pp. 585–92.

13. P.D. Lee and J.D. Hunt: *Scripta Mater.*, 1997, vol. 36, pp. 399-404.

14. R.C. Atwood and P. D. Lee: *Metall. Mater. Trans. B*, 2002, vol. 33, pp. 209-221.

15. P.D. Lee, A. Chirazi, and D. See: *J. Light Met.*, 2001, vol. 1, pp. 15-30.

16. D. M. Stefanescu: *Int. J. Cast Met. Res.*, 2005, vol. 18, pp. 129-143.

17. E. Niyama, T. Uchida, M. Morikawa, and S. Saito: *AFS Int. Cast Met. J.*, 1982, vol. 7, pp. 52–63

18. K.D. Carlson and C. Beckermann: *Metall. Mater. Trans. A*, 2009, vol. 40, pp. 163-175.

19. J. Guo, C. Beckermann, K.D. Carlson, D. Hirvo, K. Bell, T. Moreland, J. Gu, J. Clews, S. Scott, G. Couturier, and D. Backman: *IOP Conference Series: Materials Science and Engineering*, 2015, vol. 84, p. 012003.

20. K.D. Carlson, Z. Lin, and C. Beckermann: *Metall. Mater. Trans. B*, 2007, vol. 38, pp. 541-555.

21. L. Yao, S. Cockcroft, J. Zhu, and C. Reilly: *Metall. Mater. Trans. A*, 2011, vol. 42, pp. 4137-4148.

22. Ch. Pequet, M. Rappaz, and M. Gremaud, *Metall. Mater. Trans. A*, 2002, vol. 33, pp. 2095-2106.

23. K.D. Carlson, Z. Lin, R.A. Hardin, and C. Beckermann, SFSA 56th Technical and Operating Conference, November 2002

24. A. Reis, Y. Houbaert, Z. Xu, R. Van Tol, A.D. Santos, J.F. Duarte, and A.B. Magalhaes, J. Mater. Process. Tech., 2008, vol. 202(1), pp. 428-434.

25. A. Reis, Z. Xu, R.V. Tol, and R. Neto, J. Manuf. Process., 2012, vol. 14(1), pp. 1-7.

26. Y. Awano, and K. Morimoto. *Int. J. Cast Met. Res.*, 2004, vol. 17(2), pp. 107-114.

27. P.D. Lee and J.D. Hunt: *Acta Mater.*, 1997, vol. 45, pp. 4155-4169.

28. R.C. Atwood, S. Sridhar, W. Zhang, and P.D. Lee: *Acta Mater.*, 2000, vol. 48, pp. 405-417.

29. L. Arnberg and R. Mathiesen: *JOM*, 2007, vol. 59, pp. 20–26.

30. Morgan Thermal Ceramics catalog for Superwool® 607® HT.

31. JMatPro, Sente Software Ltd, Surrey Technology Center, Surrey GU2 7YG, United Kingdom.

32. D. Emadi and L.V. Whiting: *AFS Trans.*, 2002, vol. 200, No. 033.

33. K.D. Carlson and C. Beckermann: *Int. J. Cast Met. Res.*, 2012, vol. 25, pp. 75–92.

34. P. Yousefian, and M. Tiryakioğlu: *Metall. Mater. Trans. A*, 2018, vol. 49(2) pp. 563-575.

35. S. Patankar, Numerical heat transfer and fluid flow. *CRC press*, 1980.

36. H. Samet, and M. Tamminen. *IEEE Transactions on Pattern Analysis and Machine Intelligence*, 1988, vol. 10(4), pp. 579-586.